

MONTE CARLO SIMULATIONS OF FERROELECTRIC CRYSTAL
GROWTH AND MOLECULAR ELECTRONIC STRUCTURE OF ATOMS
AND MOLECULES

A Dissertation

Presented to

The Faculty of the Department of Physics

The College of William and Mary in Virginia

In Partial Fulfillment

Of the Requirements for the Degree of

Doctor of Philosophy

by

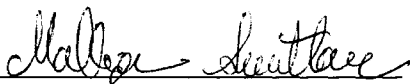
Malliga Suewattana

2005

APPROVAL SHEET

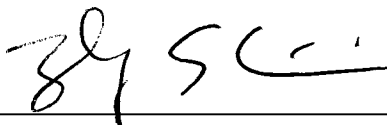
This dissertation is submitted in partial fulfillment of
the requirements for the degree of

Doctor of Philosophy

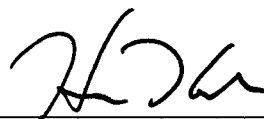


Malliga Suetana

Approved by the Committee, September 2005



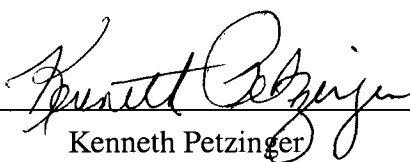
Shiwei Zhang, Chair



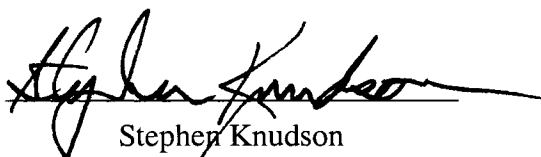
Henry Krakauer



Gina Hoatson



Kenneth Petzinger



Stephen Knudson
Chemistry

For my dear family.

Table of Contents

Acknowledgments	vii
List of Tables	viii
List of Figures	ix
Abstract	xi
CHAPTER	
1 Introduction	2
2 KMC Study of Crystal Growth in Ferroelectric Alloys	4
3 Theoretical Approach	8
3.1 The Electrostatic Model	10
3.2 Kinetic Monte Carlo method for long-range interactions	15
4 Growth Simulation Results	21
4.1 Crystal Growth	22
4.2 Energy Calculations	33
5 Concluding Remarks (Kinetic Monte Carlo Simulation of Crystal Growth)	41
5.1 Discussion	41
5.2 Summary	45
6 Phase-free AFQMC Study of Molecular Systems	46
6.1 Many-Electron Problems	47
6.1.1 Hartree-Fock approach	48

6.1.2	Density Functional Theory	50
6.2	Quantum Monte Carlo	50
7	Auxiliary-Field Quantum Monte Carlo	53
7.1	Imaginary Time Propagator	54
7.2	Slater Determinant Wavefunctions	55
7.3	Many-body Hamiltonian	58
7.4	Auxiliary-Field Formalism	58
7.5	Phase Problem	61
7.5.1	Auxiliary Field Force Bias	62
7.5.2	Rotational Invariant Projection	65
7.6	Implementations with a Planewave Basis	66
7.7	Statistical Errors	68
8	AFQMC Results	69
8.1	Pseudopotential Construction	70
8.2	LDA calculations	72
8.3	Cutoff Energy Convergence	73
8.4	Finite Size Convergence	74
8.5	Trotter Convergence	79
8.6	Ground State Properties	81
9	Concluding remarks (AFQMC Study of Molecular Electronic Structure)	89
APPENDIX A		
	Coulomb potential	91
APPENDIX B		
	Pseudopotentials	93
APPENDIX C		
	Charged Simulation Cell Correction	97
	Bibliography	99

Vita 105

ACKNOWLEDGMENTS

First and foremost, I wish to express my deep gratitude and appreciation to my advisors Prof. Shiwei Zhang and Prof. Henry Krakauer for their excellent guidance and support throughout my graduate study. I can truly say that without their teaching, encouragement and, most importantly, patience, this work would not have been possible. Thanks must also go to the members of my group Wirawan Purwanto, Eric Walter, Hendra Kwee, Wissam Al-Saidi and Dandan Mao whom I have worked closely, exchanged many useful conversations, and enjoyed much fruitful collaborations. I would also like to thank my committee members, Prof. Gina Hoatson, Prof. Kenneth Petzinger and Prof. Steven Knudson for the careful reading of this thesis and the valuable comments. A large portion of calculations were performed using computational facilities at the Center for Piezoelectric by Design and the William and Mary Sciclone clusters. I would like to thank the faculty, staff and graduate students of the Physics Department of the College of William and Mary for the education and friendship I have received. Paula Perry, Sylvia Stout, Carol Hankins and Dianne Fannin have always been friendly, kind and accessible when I needed something around the department.

I would not have been here without the financial support from the Development of Science and Technology Talented Project (DPST) of Thailand. I always thoroughly enjoyed being in the project and am sincerely grateful for the friendship from other DPST scholars. A special mention must go to Worakorn Neeyakorn, Rawee Suwandachochai and Wittaya Kaonongbua. I would like to thank everyone at the office of Educational Affair, the Royal Thai Embassy at Washington, DC who have been helping me with the administrative matter with the Thai government throughout my stay in the United States.

I would like to thank the many friends I have made outside the Physics Department who have made my experience at William and Mary much more fun. Special thanks are due to Lauren Gearhart and Heather Estes. I owe a great deal to Lou and Karol Roehr for their support and encouragement over the past three years. They have provided me with a place to call “home” in Williamsburg and of course the best home “cooked” meals ever!

I truly believe that I never could have made it through without all the love and encouragement I received from my family. I owe great deal to my parents who have always been there for me especially my mom for her support of my goals and dreams. I want to thank my big sister and my little sisters for the time we shared growing up and putting up with me always. Last, I would like to dedicate this dissertation to my late-grandfather who taught me everything I need in life. I always know that he will be proud of me.

LIST OF TABLES

8.1	Optimized pseudopotential parameters of atoms	72
8.2	The LDA total energies (from ABINIT) of severals atoms and molecules .	73
8.3	Electronic configurations of atoms and ionized atoms	84
8.4	The QMC total energies of atoms and molecules	85
8.5	Dissociation energy (eV) of selected molecules when calculated within the LDA, the AFQMC, and the HF.	86
8.6	First ionization energy (eV) of selected atoms,	86
8.7	Second ionization energy(eV) of selected atoms,	87

LIST OF FIGURES

2.1	A perovskite crystal structure.	5
2.2	A simplified diagram of the simulation restrictions,	7
3.1	Diagrams of crystal growth substrate directions.	9
4.1	Visualizations of grown BMN crystals.	25
4.2	Visualizations of rocksalt crystals.	25
4.3	Rocksalt growth rate vs. chemical potential	26
4.4	An expanded plot of rocksalt growth rate vs. chemical potential	27
4.5	BMN growth rate vs. chemical potential	27
4.6	An expanded plot of BMN growth rate vs. chemical potential	28
4.7	Illustrative results of the rocksalt growth	29
4.8	Illustrative results of the rocksalt growth	30
4.9	Rocksalt growth rate	31
4.10	BMN growth rate	32
4.11	BMN growth rate and 1:2 order parameter vs.chemical potential.	32
4.12	BMN growth rate and 1:2 order parameter vs.chemical potential.	33
4.13	Visualizations of 1:2 ordering BMN crystals.	35
4.14	Visualizations of 1:1 ordering BMN crystals.	35
4.15	Total energy per particle	36

4.16	Total energy per particle vs. Height.	37
4.17	Size-effect of 1:2 ordering for various tetravalent concentrations.	38
4.18	Total energy per particle vs. tetravalent	38
4.19	Free energy of BMN crystal	40
8.1	OPIUM generated wavefunction for Sulfur atom.	71
8.2	Convergence property of Phosphorous atom in a $14 \times 14 \times 14$ a.u. supercell.	73
8.3	Phosphorous simulation cell convergence of LDA and AFQMC.	75
8.4	Simulation cell size convergence for Al, S, Cl and As	75
8.5	Phosphorous Dissociation energy and total energy of P and P_2	76
8.6	Chlorine Dissociation energy and total energy of Cl and Cl_2	77
8.7	Illustration of the non-periodic charged supercell simulations to the convergence of total energy.	79
8.8	Series of Phosphorous ionization energy and P, P^+ and P^{++} total energy with respect to $1/V$	80
8.9	S and S_2 Trotter error extrapolations for LDA wavefunctions	80
8.10	S and S_2 Trotter error extrapolations for Hartree-Fock wavefunctions	81
8.11	Trotter error extrapolations for P, P^+ and P^{++}	82
8.12	LDA total energy as a function of interatomic distances	82

ABSTRACT

In this thesis, we explore two stochastic techniques to study properties of materials in realistic systems. Specifically, the kinetic Monte Carlo (KMC) method is utilized to study the crystal growth process of ferroelectric materials and the quantum Monte Carlo (QMC) approach is used to investigate the ground state properties of atoms and molecules.

In the growth simulations, we study the growth rates and chemical ordering of ferroelectric alloys using an electrostatic model with long-range Coulomb interactions. Crystal growth is characterized by thermodynamic processes involving adsorption and evaporation, with solid-on-solid restrictions and excluding diffusion. A KMC algorithm is formulated to simulate this model efficiently in the presence of long-range interactions. The growth process is simulated as a function of temperature, chemical composition, and substrate orientation. We carried out the simulations on two heterovalent binaries, those of the NaCl and the $\text{Ba}(\text{Mg}_{1/3}\text{Nb}_{2/3})\text{O}_3$ (BMN) structures. Compared to the simple rocksalt ordered structures, ordered BMN grows only at very low temperatures and only under finely tuned conditions. For materials with tetravalent compositions, such as $(1 - x)\text{Ba}(\text{Mg}_{1/3}\text{Nb}_{2/3})\text{O}_3 + x\text{BaZrO}_3$ (BMN-BZ), the model does not incorporate tetravalent ions at low-temperature, exhibiting a phase-separated ground state instead. At higher temperatures, tetravalent ions can be incorporated, but the resulting crystals show no chemical ordering in the absence of diffusive mechanisms.

In the second part of the thesis, we present results from an auxiliary field quantum Monte Carlo (AFQMC) study of ground state properties, in particular dissociation and ionization energy, of second-row atoms and molecules. The method projects the many-body ground state from a trial wavefunction by random walks in the space of Slater determinants. The Hubbard-Stratonovich transformation is employed to decouple the Coulomb interaction between electrons. A trial wave function $|\Psi_T\rangle$ is used in the approximation to control the “phase problem”. We also carry out Hartree-Fock (HF) and Density Functional Theory (DFT) calculations for comparison to AFQMC results and to serve as starting wavefunctions for our AFQMC calculations. Results of dissociation energy are in excellent agreement with experimental values. Ionization energy errors are somewhat larger than those of other methods. We conclude with a discussion of several possible sources of error as well as a direction for the improvement.

MONTE CARLO SIMULATIONS OF FERROELECTRIC CRYSTAL GROWTH AND
MOLECULAR ELECTRONIC STRUCTURE OF ATOMS AND MOLECULES

CHAPTER 1

Introduction

Modifications and designs of new materials using trial and error laboratory synthesis is time-consuming and costly. The last decade, it has become increasingly viable to determine and predict material properties using computer simulations. Because the computational capabilities are becoming more powerful, parameters which are not easily measured can be calculated sufficiently for our purpose. Species and atomic arrangements of the system can also be controlled directly. In this thesis we focus on two distinct studies: i) the kinetic Monte Carlo (KMC) of crystal growth in ferroelectric alloys and ii) the study of ground state properties of atoms and molecules within the framework of the auxiliary field quantum Monte Carlo (AFQMC).

The first part of this thesis, where the growth process of complex perovskite structure-based ferroelectric materials is investigated by kinetic Monte Carlo (KMC) method, consists of the following four chapters. Chapter 2 provides more insight on the motivation and background of the project. Chapter 3 is devoted to the theoretical approaches. An ionic model used to simulate the relaxor single crystals is reviewed in detail and our adaptation for the growth modeling, which includes the special handling of electrostatic interactions during the growth process is discussed. Furthermore, we describe the generalization and

modification of the KMC algorithm for long-range interactions. In Chapter 4, we present the results of our growth simulations for the perovskite $A(BB')O_3$ and $A(BB'B'')O_3$ crystals. Growth rates and order structure of NaCl and BMN type crystals as a function of temperature, chemical composition and growth orientation are shown. To help understand our growth results for systems where a (typically small) fraction of tetravalent B'' ions are mixed in, we carry out total energy calculations to study the compound stability. Chapter 5 addresses our crystal growth predictions and prospects for the model and points out the future directions. Most of the results described in these chapters have been published [1, 2].

Chapter 6-9 are devoted to the study of quantum mechanical ground state properties of atoms, ions, and molecules by using the auxiliary field quantum Monte Carlo. Chapter 6 introduces AFQMC method as well as several one-electron methods. Chapter 7 concentrates on several details of the auxiliary field quantum Monte Carlo formalism including the Trotter decomposition and the application of Hubbard Stratonovich Transformation. We also address the phase problem and discuss new formulations used to control it. In Chapter 8, we articulate details of the computational parameters. Illustrative convergence tests are given and we also present results on dissociation energy and ionization energy. Finally, several aspects of the results are discussed in Chapter 9. A manuscript describing this study is in preparation [3].

In Appendix A, we include some technical details on the treatment of the long-range interactions in our simulations. We describe the formalism of the optimized non-local pseudopotential in Appendix B. We devote Appendix C to the discussion of the charged simulated unit cell corrections, which are utilized in the study of ionization energy.

CHAPTER 2

KMC Study of Crystal Growth in Ferroelectric Alloys

Ferroelectric crystals are known for their important technological applications such as high-permittivity dielectrics, piezoelectric sensors, transducers, and mechanical actuators [4]. Recently, single-crystal relaxor perovskites such as $\text{Pb}(\text{Zn}_{1/3}\text{Nb}_{2/3})\text{O}_3\text{-PbTiO}_3$ (PZN-PT) and $\text{Pb}(\text{Mg}_{1/3}\text{Nb}_{2/3})\text{O}_3\text{-PbTiO}_3$ (PMN-PT) were synthesized and found to exhibit ultrahigh strain and very large piezoelectric constants [5]. The structure of alloys like PMN-PT can be viewed as a perovskite ABO_3 framework (a cubic lattice for the ideal perovskite crystal), with Pb ions on the A-site and a solid solution of (Mg^{+2} , Nb^{+5} , Ti^{+4}) ions on the B-sites, with average B-site ionic charge $+4$. Of course this is an idealized picture, neglecting vacancies, impurities, local structural distortions, and partial chemical ordering on the B-sites. The ideal cubic ABO_3 perovskite is pictured in Fig. 2.1. The A atoms are at the cube corners, the O atoms are at the face centers and the B atom is at the cube center which forms an octahedron with the O sites.

Partial B-site chemical ordering is a common feature of the high-piezoelectric solid solutions. While random B-site ordering is observed in isoelectronic solid solutions

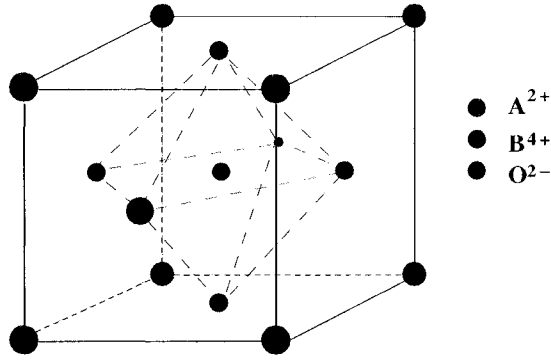


FIG. 2.1: A perovskite crystal structure. The locations of A, B and O site atoms are shown. The A atoms are usually group II metal while the B atoms can be several different elements.

like $\text{Pb}(\text{Zr}_{1-x}\text{Ti}_x)\text{O}_3$ (PZT), non-isoelectronic B-site solid solutions $\text{A}(\text{BB}'\text{B}'')\text{O}_3$, with B-site cations from group II, IV, and V, often exhibit compositionally-dependent B-site chemical ordering. At 1640°C , when the tetravalent composition x is increased in $(1-x)\text{Ba}(\text{Mg}_{1/3}\text{Nb}_{2/3})\text{O}_3 + x\text{BaZrO}_3$ (BMN-BZ), the following sequence of B-site ordering is observed: $[111]_{1:2}$ order for $x < 5\%$; then $[111]_{1:1}$ order for $5\% < x < 25\%$; and finally disorder for larger x [6]. The $[111]_{1:2}$ notation refers to x-ray observation of alternating $\beta\beta\beta'$ $[111]$ stacking of B-sites, where β and β' denote average scattering sites. For example, in BMN-BZ with $x = 0$, one can identify β with Nb and β' with Mg. The $[111]_{1:1}$ notation refers to x-ray observation of rocksalt-like alternating $\beta\beta'$ $[111]$ stacking of B-cations. In this case, the assignment of the β and β' sites has been debated, as discussed below in connection with the space-charge and random-site models [6]. Other Ba-based perovskites, e.g., $(1-x)\text{Ba}(\text{Mg}_{1/3}\text{Ta}_{2/3})\text{O}_3 + x\text{BaZrO}_3$ (BMT-BZ) [6], $(1-x)\text{Ba}(\text{Mg}_{1/3}\text{Nb}_{2/3})\text{O}_3 + x\text{BaZrO}_3$ (BMN-BZ) [7], display a similar sequence of B-site order. On the other hand, for Pb-based systems, e.g., $(1-x)\text{Pb}(\text{Mg}_{1/3}\text{Ta}_{2/3})\text{O}_3 + x\text{PbZrO}_3$ (PMT-PZ), $[111]_{1:2}$ order is not observed at $x = 0$; instead, annealing between 1325°C and 1350°C results in $[111]_{1:1}$ order all the way down to $x = 0$ [8, 9]. Other Pb-based perovskites, e.g., $\text{Pb}(\text{Mg}_{1/3}\text{Nb}_{2/3})\text{O}_3$ (PMN) [10, 11], display similar B-site ordering.

Since their discovery, growing large single crystals has been a major research goal,

but this effort has been largely unsupported by theory, because of the difficulty in modeling and simulating the non-equilibrium processes occurring in nucleation and crystal growth in such complex materials. In this thesis, we use kinetic Monte Carlo [12] simulations of a simple effective Hamiltonian to model the growth process of these ferroelectric crystals.

Given the ionic character of these materials, it is not surprising that the inclusion of Coulomb interactions has been found to be crucial in describing their properties. A simple, purely electrostatic model introduced by Bellaiche and Vanderbilt (BV) [13] has had considerable success in explaining the observed equilibrium B-site chemical ordering in many perovskite alloys. The BV model only considers Coulomb interactions between point charges (+2, +5, +4, etc., representing the different atomic species) that reside on the B-sites, which are constrained to lie on an ideal cubic sublattice.

This electrostatic model is the starting point of our growth simulations. Simplified models based on Ising like effective Hamiltonians H_{eff} have been used to model growth in simpler systems [14, 15]. These models often have only short-range interactions where the atoms only interact with the nearest-neighbors. To adapt the electrostatic model of BV to study crystal growth, we consider a slab-geometry with periodic boundary conditions in two-dimensions while having the third dimension (positive z) as the growth direction. The slab is viewed as being embedded in a liquid-phase melt, which is parametrized by a chemical potential difference $\Delta\mu$ with the solid bulk phase. Moreover, $\Delta\mu$ is the essential variable which dictates the growth kinetic as well as the growth modes. In our simulations, the spatial lattice is defined by the substrate lattice. The crystal configuration is updated according to the long-range Coulomb interactions. Atoms of the crystal normally are constrained to reside only on a discrete site. In addition, a solid-on-solid (SOS) restriction is imposed, which requires that adsorption only occur onto empty lattice sites directly above an occupied site, so void formation is neglected. In keeping with the simplicity of the model, diffusion in the bulk and at the surface is also neglected.

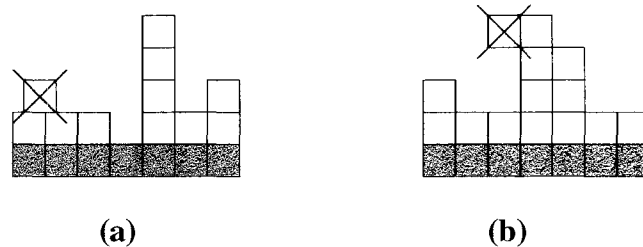


FIG. 2.2: A simplified diagram of the simulation restrictions, (a) a discrete placement and (b) solid-on-solid.

The non-equilibrium dynamics of the growth process are modeled using the kinetic Monte Carlo (KMC) method [16]. The KMC algorithm introduced by Bortz, Kalos, and Lebowitz (BKL) [12] has been quite successful in simulating crystal growth in Ising-like models with short-range interactions between adatoms, but the method is inefficient in the presence of long-range interactions. We discuss a generalization of the algorithm to efficiently handle the long-range interactions in the BV model.

CHAPTER 3

Theoretical Approach

Crystal growth is, by its nature, a non-equilibrium phenomenon. There are several contexts which need to be considered in the growth process i.e. the growth rate at which the crystals reach the equilibria and the adatoms behavior at the growth surface. In practice, crystal growth occurs as a transition of solid \rightarrow crystal(melt), liquid \rightarrow crystal(solution), or gas \rightarrow crystal(vapor) [17]. Normally crystals will grow from a melt much more rapidly than they will grow from a vapor or a solution phase. This is simply because the density of adatoms in the melt is comparable to those in a crystal, so the adatoms to be grown already exist [18]. For both vapor and solution growth, the density of adatoms is relatively low therefore, the growth rate will be much smaller than that of from the melt. Our simulations are mainly based on the crystal growth from the melt phase. At each stage of the simulation the crystal is modeled as a slab of finite thickness. However, it is convenient to index the allowed B-sites as in an infinite three-dimensional crystal lattice

$$\mathbf{l} = i \mathbf{a}_1 + j \mathbf{a}_2 + k \mathbf{a}_3. \quad (3.1)$$

Two-dimensional (2-D) periodic boundary conditions (PBC) are employed along the \mathbf{a}_1 and \mathbf{a}_2 directions. The \mathbf{a}_1 and \mathbf{a}_2 lattice vectors lie in the x - y Cartesian plane, and are used to define a $L_1 \mathbf{a}_1 \times L_2 \mathbf{a}_2 = \mathbf{A}_1 \times \mathbf{A}_2$ 2-D supercell. Growth proceeds along the

z -direction. In the calculations, we employ two substrate orientations, $[001]$ and $[\bar{1}\bar{1}\bar{1}]$, and their lattice vectors are depicted in Figure 3. The simulation is initialized as a slab of uniform thickness $H_0\mathbf{a}_3$, with a predefined B-atom configuration. A given simulation is terminated when either the maximum slab thickness or the maximum number of Monte Carlo (MC) time steps is reached. We use the notation $L \times L \times H_{\max}$ to label a particular simulation where H_{\max} is the number of layers for maximum slab thickness (the initial substrate included).

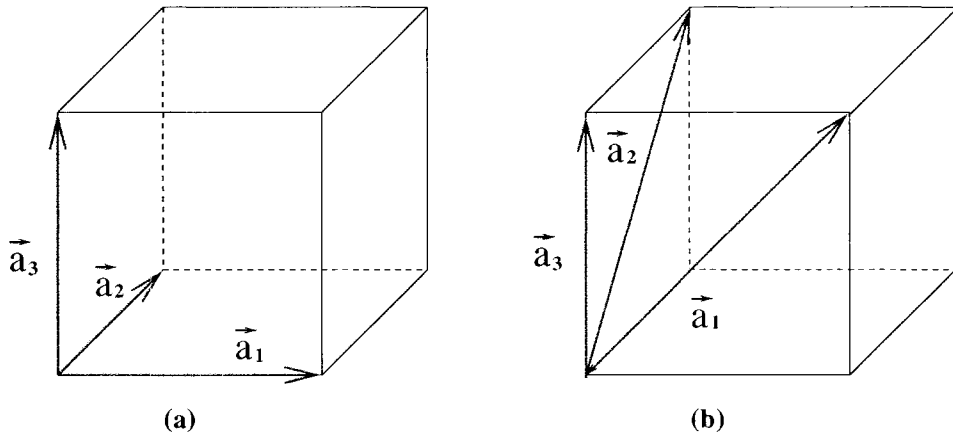


FIG. 3.1: Diagrams of crystal growth substrate directions. (a)[001] and (b)[$\bar{1}\bar{1}\bar{1}$]

Since the SOS restriction that we impose does not allow the formation of voids, the crystal configuration, \mathcal{C} , is specified at each stage of the simulation by the set of occupied sites $l = (i, j, k)$ and their charges q_l . The BV electrostatic model cannot be directly used in this slab geometry, due to ill-defined electrical boundary conditions in the z direction and the lack of exact charge neutrality during the growth simulation. Section 3.1 describes how we handle these issues. Similarly, a direct application of the KMC algorithm is inefficient due to the long-range Coulomb interaction. Section 3.2 describes the KMC method and our modifications to make it applicable to the model.

3.1 The Electrostatic Model

The BV model is derived by considering the total electrostatic energy for an $A(BB'B'')O_3$ compound:

$$E(C) = \sum_{(l,\tau,l',\tau')} \frac{Q_{l\tau}Q_{l'\tau'}}{\epsilon|\mathbf{R}_{l\tau} - \mathbf{R}_{l'\tau'}|}, \quad (3.2)$$

where $\mathbf{R}_{l\tau}$ is the position of the ion on site τ ($=A, B, O_1, O_2, O_3$) in cell l , and ϵ is the dielectric constant. For a given Bravais lattice, ϵ sets the energy scale. We consider the perovskite structure with group II A-site atoms (e.g. Ba, Pb), so the charges on the A and O sites have fixed values of $+2e$ and $-2e$, respectively. Since the average B-site charge is $+4e$, it is convenient to express the charges on the B-sites, $Q_{l,B}$, as

$$Q_{l,B} = 4e + q_l. \quad (3.3)$$

Up to a constant, the configurationally averaged electrostatic energy depends only on the B-site charges, since the configurational average of q_l is zero:

$$E_B(C) = \frac{1}{\epsilon a} \sum_{(l,l')} \frac{q_l q_{l'}}{|l - l'|}, \quad (3.4)$$

where we have for simplicity restricted ourselves in Eq. (3.4) to a cubic Bravais lattice with lattice parameter a , and $\mathbf{R}_{lB} = l a$. In this model each cell l is therefore reduced to a single lattice site with charge q_l , and the energy of the compound is given by the inter-site Coulomb interaction.

The long-range Coulomb interaction must be treated with care in a bulk simulation to ensure proper convergence. For 2-D and 3-D simulations with periodic boundary conditions, the method of Ewald sum is often used, in which periodic images of the charges and neutralizing background charges are introduced [19, 20, 21, 22, 23] so that the bare Coulomb form $1/|l - l'|$ is replaced with a reduced form $v(l - l')$. For our growth simulations, we are dealing with a slab geometry with PBC only in two dimensions (x - y). Some modifications are required before the Ewald method can be applied.

In the simulations, we will need to calculate the energy change from Eq. (3.4) due to the evaporation of a charged ion q_l at the surface of the crystal (see Eq. (3.25) below). The distribution of point charges that q_l “sees” can be described by the charge density

$$\rho(\mathbf{r}) = \sum_{\mathbf{l}} \sum_{\mathbf{R}} q_l \delta(\mathbf{r} - \mathbf{l} - \mathbf{R}) \quad (3.5)$$

where \mathbf{l} runs through the position vectors of the atoms within the simulation cell, and \mathbf{R} is a 2-D Bravais supercell lattice vector: $\mathbf{R} = n_1 \mathbf{A}_1 + n_2 \mathbf{A}_2$. Directly summing the Coulomb potentials of the individual point charges, $V(\mathbf{r} - \mathbf{l} - \mathbf{R}) = q_l / |\mathbf{r} - \mathbf{l} - \mathbf{R}|$, leads to an ill-defined and conditionally convergent result, as is well known. However, for three-dimensional periodic boundary conditions, a unique solution of Poisson’s equation exists (for an electrically neutral system), and it is conveniently calculated using Ewald’s method. Subject to some additional physically motivated conditions, a unique solution can also be found for finite thickness slabs that are infinite in extent along two spatial directions.

Solutions of Poisson’s equation, $\nabla^2 V(\mathbf{r}) = -4\pi\rho(\mathbf{r})$, in our simulations are subject to two-dimensional (2-D) PBC, $V(\mathbf{r} + \mathbf{R}) = V(\mathbf{r})$, as is the charge density $\rho(\mathbf{r})$. The 2-D PBC imply that $V(\mathbf{r})$ and $\rho(\mathbf{r})$ can be expanded as:

$$\begin{aligned} \rho(\mathbf{r}) &= \sum_{\mathbf{G}} \rho_{\mathbf{G}}(z) e^{i\mathbf{G} \cdot \mathbf{r}_p} \\ V(\mathbf{r}) &= \sum_{\mathbf{G}} V_{\mathbf{G}}(z) e^{i\mathbf{G} \cdot \mathbf{r}_p}, \end{aligned} \quad (3.6)$$

where \mathbf{G} is a 2-D supercell reciprocal lattice vector and \mathbf{r}_p is the x - y component of \mathbf{r} , $\mathbf{r}_p = \mathbf{r} - (\mathbf{r} \cdot \hat{\mathbf{z}})\hat{\mathbf{z}} = i\mathbf{a}_1 + j\mathbf{a}_2$.

Substitution of Eqs. (3.6) into Poisson’s equation yields

$$\frac{d^2 V_{\mathbf{G}}(z)}{dz^2} - G^2 V_{\mathbf{G}}(z) = -4\pi\rho_{\mathbf{G}}(z), \quad (3.7)$$

whose solution can be expressed as

$$V_G(z) = -4\pi \int_{-\infty}^{\infty} \mathcal{G}(z - z') \rho_G(z') dz', \quad (3.8)$$

where $\mathcal{G}(z - z')$ is the Green's function corresponding to Eq. (3.7).

If there are any ill-defined contributions to the Coulomb potential, they must arise from the $\mathbf{G} = \mathbf{0}$ solution in Eq. (3.7). This is because only the $\mathbf{G} = \mathbf{0}$ term of $\rho(\mathbf{r})$ in Eqs. (3.6) contributes to the net slab charge. In addition, even if the slab is electrically neutral, there may still be a net dipole moment D , which would lead to different asymptotic values of the Coulomb potential at $z = \pm\infty$. Again, D also depends only on the $\mathbf{G} = \mathbf{0}$ term of $\rho(\mathbf{r})$, where

$$D \equiv \int_{-\infty}^{\infty} z \bar{\rho}(z) dz, \quad (3.9)$$

and where

$$\bar{\rho}(z) = \frac{1}{A} \int_A \rho(\mathbf{r}) dx dy = \rho_{\mathbf{G}=\mathbf{0}}(z), \quad (3.10)$$

and A is the area of the 2D supercell.

We therefore first consider the solutions of Eq. (3.7) for $G \neq 0$. Physically meaningful results require that the solutions satisfy $\lim_{|z| \rightarrow \infty} V_G(z) = 0$, which leads to the following unique definition of the $G \neq 0$ Green's function:

$$\mathcal{G}(z - z') \equiv -\frac{[\vartheta(z - z')e^{-G(z-z')} + \vartheta(z' - z)e^{G(z-z')}]}{2G}, \quad (3.11)$$

where $G = |\mathbf{G}|$. For any reasonably localized charge distribution $\rho_G(z)$, Eqs. (3.8) and (3.11) result in well behaved exponentially decaying solutions $V_G(z)$ as $|z| \rightarrow \infty$.

For $G = 0$ Eq. (3.7) becomes

$$\frac{\partial^2 V_0(z)}{\partial z^2} = -4\pi \rho_0(z). \quad (3.12)$$

As adatoms are adsorbed or adatoms evaporate in the course of the growth simulations, the net charge will fluctuate so that the total charge in the simulation supercell will

not be precisely zero at each stage of the simulation. Similarly a net dipole D may form. However, in a real growth process there are always compensating charges that will cancel any ill-defined long-range effects due to the lack of charge neutrality or the presence of a dipole moment. In our calculations, we simulate this by a construction that ensures that $\rho_{G=0}(z)$ always represents a neutral charge distribution with $D = 0$. This leads to well-defined boundary conditions $\lim_{|z| \rightarrow \infty} V_0(z) = 0$.

As in the 3-D Ewald method, a diffuse localized charge density $g(\mathbf{r})$ is added and subtracted to each point charge to facilitate the decomposition of the potential into absolutely convergent direct- and reciprocal lattice sums:

$$\begin{aligned} \rho(\mathbf{r}) &= \sum_{\mathbf{l}} \sum_{\mathbf{R}} q_{\mathbf{l}} [\delta(\mathbf{r} - \mathbf{l} - \mathbf{R}) - g(\mathbf{r} - \mathbf{l} - \mathbf{R})] + \sum_{\mathbf{l}} \sum_{\mathbf{R}} q_{\mathbf{l}} g(\mathbf{r} - \mathbf{l} - \mathbf{R}) \\ &\equiv \rho_1(\mathbf{r}) + \rho_2(\mathbf{r}). \end{aligned} \quad (3.13)$$

The diffuse charge density $g(\mathbf{r})$ is chosen to be a normalized spherically symmetric Gaussian, as in the 3-D Ewald method:

$$g(\mathbf{r}) \equiv \left(\frac{\alpha}{\pi}\right)^{3/2} e^{-\alpha r^2}, \quad (3.14)$$

where the value of the Ewald convergence parameter α is arbitrary, but is usually chosen to optimize the convergence of both the direct- and reciprocal-lattice sums. The integrated charge of $\rho_1(\mathbf{r})$ is zero by construction, as is its dipole moment D , so its contribution $V_1(\mathbf{r})$ to the Coulomb potential can be obtained by a rapidly convergent direct-lattice sum, given in the Appendix A.

On the other hand, the procedure for calculating the Coulomb potential $V_2(\mathbf{r})$ due to $\rho_2(\mathbf{r})$ requires special handling. At each site \mathbf{l}' in the unit cell, the potential $V_2(\mathbf{l}')$ is effectively computed as arising from the true $\rho_2(\mathbf{r})$ plus an additional artificial density chosen to keep the slab neutral and cancel its dipole moment. We implicitly construct this artificial density by introducing two approximations, described below, into the usual

Ewald method. $V_2(\mathbf{l}')$ is due to: *i*) the $\mathbf{l} \neq \mathbf{l}'$ Gaussian charge densities and their periodic images $q_{\mathbf{l}}g(\mathbf{r} - \mathbf{l} - \mathbf{R})$, and *ii*) the periodic images $q_{\mathbf{l}'}g(\mathbf{r} - \mathbf{l}' - \mathbf{R})$. [As in the 3-D Ewald method, a spurious interaction of the point charge $q_{\mathbf{l}'}$ with its own Gaussian density $q_{\mathbf{l}'}g(\mathbf{r} - \mathbf{l}')$ is explicitly removed later.] Alternatively, the contribution (*ii*) above due to the \mathbf{l}' -sublattice Gaussian images can be replaced by the sum of Gaussian images *iiia*) $-q_{\mathbf{l}}g(\mathbf{r} - \mathbf{l}' - \mathbf{R})$. Note the replacement of $q_{\mathbf{l}'}$ by $-q_{\mathbf{l}}$ on the \mathbf{l}' -sublattice. These two formulations are equivalent in a bulk crystal simulation with 3-D PBC and a neutral simulation cell, since the integrated total charge vanishes:

$$\sum_{\mathbf{l} \neq \mathbf{l}'} -q_{\mathbf{l}} = q_{\mathbf{l}'}. \quad (3.15)$$

In the 2-D slab geometry of our growth simulations, this will not be the case in general. Overall charge neutrality is still satisfied in a statistical sense, however. Our procedure for calculating $V_2(\mathbf{r})$ consists of two approximations. The first approximation is to use formulation (*iiia*) above which effectively imposes charge neutrality. Regrouping the sums, the approach *iiia*) can alternatively be viewed as saying that the contribution of each $q_{\mathbf{l}}g(\mathbf{r})$ sublattice to $V_2(\mathbf{l}')$ is to be calculated as the potential due to the charge density:

$$\rho_2^{(\mathbf{l}, \mathbf{l}')}(r) = q_{\mathbf{l}} \sum_{\mathbf{R}} [g(\mathbf{r} - \mathbf{l} - \mathbf{R}) - g(\mathbf{r} - \mathbf{l}' - \mathbf{R})]. \quad (3.16)$$

Since the integrated charge of $\rho_2^{(\mathbf{l}, \mathbf{l}')}(r)$ is zero, the use of this approximation effectively imposes overall charge neutrality at each stage of the growth simulation.

The boundary conditions are still ill-defined however, since the sum of sublattice potentials due to the $\rho_2^{(\mathbf{l}, \mathbf{l}')}(r)$ may still have a dipole moment D . We therefore introduce a second approximation: the Gaussian image densities $-q_{\mathbf{l}}g(\mathbf{r} - \mathbf{l}' - \mathbf{R})$ are made coplanar with the $q_{\mathbf{l}}g(\mathbf{r} - \mathbf{l} - \mathbf{R})$ sublattice. In other words, the Gaussian densities $-q_{\mathbf{l}}g(\mathbf{r})$ are placed at positions that are the projections of the $q_{\mathbf{l}'}$ image positions onto the plane defined by the $q_{\mathbf{l}}$ sublattice. In place of Eq. (3.16), the contribution of each $q_{\mathbf{l}}g(\mathbf{r})$ sublattice is

thus calculated as the potential due to the charge density:

$$\tilde{\rho}_2^{(\mathbf{l}, \mathbf{l}')}(\mathbf{r}) = q_t \sum_{\mathbf{R}} \left[g(\mathbf{r} - \mathbf{l} - \mathbf{R}) - g(\mathbf{r} - \tilde{\mathbf{l}}' - \mathbf{R}) \right], \quad (3.17)$$

where $\tilde{\mathbf{l}}'$ denotes the projection of the position \mathbf{l}' onto the plane defined by the q_t sublattice. The charge density $\tilde{\rho}_2^{(\mathbf{l}, \mathbf{l}')}(\mathbf{r})$ has a rapidly convergent expansion in terms of 2-D planewaves given by Eq. (3.6). Moreover, the $\mathbf{G} = 0$ contribution of $\tilde{\rho}_2^{(\mathbf{l}, \mathbf{l}')}(\mathbf{r})$ vanishes, so the Coulomb potential $V_2(\mathbf{r})$ is readily found using the equations given in the Appendix. These two approximations ensure overall average-charge neutrality and vanishing dipole moment $D = 0$, resulting in a well-defined Coulomb potential at each stage of the growth simulation. Complete formulas for the potential $v(\mathbf{l}' - \mathbf{l})$ are given in the Appendix.

3.2 Kinetic Monte Carlo method for long-range interactions

The kinetic Monte Carlo (KMC) method is one of several simulation techniques commonly employed to model the relaxation processes of systems away from equilibrium (e.g. growth processes). It has been applied successfully to crystal growth and surface/interface phenomena, [16, 24] mostly in the context of kinetic Ising models. Due to the long-range interactions between ions in our electrostatic model, the usual implementation of KMC for Ising-like models is inefficient, with the acceptance rates of events becoming very low. We developed a modified sampling algorithm to make the simulation practical for this model. Here we briefly outline the basic theoretical background for the KMC method, and then describe our modifications and give the relevant implementation details.

In the KMC simulation, the dynamics of the system is described as stochastic processes such as adsorption, evaporation, and surface migration. We consider only the first two in our simulation. As mentioned, the adatoms represent the B-site ions in the single

crystal perovskite alloy. They are characterized entirely by their charges and they interact with each other by the interaction described above. The goal of our KMC method is to create a new configurational crystal from the grand canonical ensemble of a system at a given temperature. This can be accomplished by repeatedly updating a current configuration randomly with the Boltzman factor which identifies the event probability . The process evolves until an acceptable equilibrium (crystal height or simulation time) is achieved.

In the grand canonical ensemble, the Hamiltonian that will be used in the growth simulations can then be expressed in term of Eq. (3.4) as

$$\mathcal{H}(C) = E_B(C) + \Delta\mu N, \quad (3.18)$$

where N is the total number of adsorbed adatoms. The electrostatic energy term in the Hamiltonian is responsible for evaporation, while the second term, which depends on the chemical potential difference between the solid and the gas phases, controls the rate in which adatoms stick on the surface. On the other hand, $E_B(C)$ is the energy loss in the evaporation while the second term dictates the total energy loss caused by all adsorptions. The growth simulation is then characterized by competing adsorption and desorption events. The SOS restriction imposed in the simulation prevents formation of vacancies and allows us to write H as

$$\mathcal{H}(C) = E_B(C) + \Delta\mu \sum_{i,j} h_{ij}, \quad (3.19)$$

where h_{ij} is the number of layers in the present crystal configuration at the horizontal position $i\mathbf{a}_1 + j\mathbf{a}_2$.

In KMC the time evolution of the system is simulated through a Markov chain of configurations where the growth probability depends only on information from the one previous time step and not any other. Let us define $P(C, t)$ as a time-dependent distribution of configurations. The transition rate from C to C' , a crystal configuration related

to C by a single time step, is denoted by $w(C \rightarrow C')$. We then have the usual master equation [24]:

$$\frac{\partial P(C, t)}{\partial t} = - \sum_{C'} w(C \rightarrow C') P(C, t) + \sum_{C'} w(C' \rightarrow C) P(C', t), \quad (3.20)$$

where the first term on the right describes the loss because of transitions away from C , while the second term describes the gain because of transitions into C . Once again this confirms the competing process between adsorption and evaporation in the growth process. In the equilibrium limit (as $t \rightarrow \infty$), the Boltzmann distribution

$$P_{eq} = Z^{-1} \exp \left[\frac{-\mathcal{H}(C)}{k_B T} \right] \quad (3.21)$$

is reached, where k_B is the Boltzmann constant and Z is a partition function. To construct a transition which maintains thermal equilibrium with the Hamiltonian, we require that a detailed balance be satisfied:

$$\frac{w(C \rightarrow C')}{w(C' \rightarrow C)} = \frac{P_{eq}(C')}{P_{eq}(C)} = \exp \left[\frac{\mathcal{H}(C') - \mathcal{H}(C)}{k_B T} \right]. \quad (3.22)$$

We adopt the following choice of transition rates $w(C \rightarrow C')$

$$w_a = \exp(\Delta\mu/k_B T) \quad (3.23)$$

$$w_e = \exp(-\Delta E_B(C)/k_B T), \quad (3.24)$$

where w_a and w_e are the rates for adsorption and evaporation, respectively, of an adatom. It can be verified directly that this choice indeed satisfies Eq. (3.22). The rate w_e for an adatom of charge $q_{\tau'}$ to evaporate from the surface depends on the change in total potential energy in the crystal

$$\begin{aligned} \Delta E_B(C) &= E_B(C') - E_B(C) \\ &= \frac{q_{\tau'}}{\epsilon a} \sum_{\mathbf{l}} q_{\mathbf{l}} v(\mathbf{l}' - \mathbf{l}). \end{aligned} \quad (3.25)$$

We emphasize that the choice of the transition rates is not unique and can affect the dynamics in the KMC simulation. In the absence of additional knowledge, the choice

outlined above is a reasonable approximation and is commonly used. It is important, however, to keep in mind the somewhat artificial nature of the dynamics in KMC. This is also related to the issue of “time” in KMC, which we comment on at the end of this section.

For kinetic Ising models, the algorithm of BKL[12] allows an efficient stochastic realization of the kinetic process under the choice in Eq.’s (3.23) and (3.24). In this algorithm, a site (i, j) is selected randomly in each step at the surface of the grown crystal. An event is then selected by Monte Carlo sampling [25] from the list of three possible events, {adsorption, evaporation, nothing}. The interaction in Ising type models is limited to near-neighbors, and the energy difference $\Delta E_B(C)$ is completely determined by the *local* environment at site (i, j) . The global maximum of w_e , i.e., the minimum possible energy change, $\Delta E^{\min} = \min[\Delta E_B(C)]$, can be obtained straightforwardly by considering all possible local configurations. This gives a corresponding global maximum of the evaporation rates: $w_e^{\max} = \exp(-\Delta E^{\min}/k_B T)$, which defines a normalization factor:

$$W \equiv w_a + w_e^{\max}. \quad (3.26)$$

The relative probabilities for the three events are therefore

$$\{P_a \equiv \frac{w_a}{W}, P_e \equiv \frac{w_e}{W}, P_n \equiv 1 - P_a - P_e\}. \quad (3.27)$$

With the electrostatic model, however, the energy change in Eq. (3.24) depends on the *entire* configuration C . It is therefore difficult to determine the global minimum, ΔE^{\min} . Indeed, even if ΔE^{\min} could be identified, the energy change $\Delta E_B(C)$, which can vary greatly with C and the simulation cell size, would be much greater than ΔE^{\min} for most configurations. This would cause the evaporation and adsorption probabilities P_a and P_e to be small, with P_n approaching unity. As a result the acceptance rate of events becomes small, and the algorithm becomes ineffective.

To overcome this difficulty, we modify the standard algorithm so that all $N = L_1 \times$

L_2 surface sites are considered *simultaneously*, instead of sweeping through the surface sites. An event list is created which includes every possible event for every possible surface site. This increases the algorithm complexity, because of the need to store and update an array of surface potentials, calculate the event list, and sample an event from this list. The advantage is that an event is guaranteed to take place in each step of the algorithm and that the need for determining ΔE^{\min} is eliminated. Evaporation/adsorption rates for all possible sites are normalized. The sum of the probabilities for an adsorption or evaporation to occur at a surface site is unity. Specifically, the modified algorithm consists of the following steps:

- (i) Generate a list, \mathcal{E} , of all possible events per time step. There are $2N$ possible events: an evaporation or an adsorption could happen on each of the $N = L_1 \times L_2$ surface sites.
- (ii) Calculate the rates (w) of adsorption and evaporation for each site on the surface. Denote the total rates by W : $W = \sum_i^{2N} w_i$.
- (iii) Normalize these $2N$ rates by W , giving probabilities, P_i , for adsorption and evaporation on sites $1, 2, \dots, 2N$.
- (iv) Generate a random number $r \in [0, 1)$ and choose the first event \mathcal{E}_i such that $\sum_{k=1}^i P_k \geq r$. An event will always be chosen.
- (v) Generate the new configuration C' based on the chosen event \mathcal{E}_i .
- (vi) Assign a “real time” increment $\Delta t_{\text{real}} = -\ln(r')/W$ to this MC step, where r' is another random number on $[0, 1)$.

The last step is a result of our considering the global event list and forcing an event to occur in every step. The issue of real “time” in a KMC simulation is a subtle one. Often the Monte Carlo time, t_{MC} , is used as some measure of the real time. In the standard algorithm, the global normalization factor W (defined by w_e^{\max}) controls the overall rate of events and sets a “time scale.” In our approach, W is time-dependent, and an event is forced to happen in each step regardless of the total rate W for the configuration at hand.

When W is low, an evaporation or adsorption is less likely to happen but one is selected anyway. Conversely, when W is high, an evaporation or adsorption is more likely to happen but still only one is selected. This introduces a bias which should vanish in the limit of large system size but which should be corrected for at finite L . Based on the rate equation, we assume an exponential relation between time and W . A step in which W is high corresponds to a short time, and vice versa. Step (vi) is a way to account for this time scale stochastically, by rescaling Δt_{MC} with a MC sampling from an exponential distribution which is determined by the normalization factor W in each step.

CHAPTER 4

Growth Simulation Results

In this chapter, we present the results from our simulations for $A(BB')O_3$ and $A(BB'B'')O_3$ crystals. Growth simulations are presented in Section 4.1. Growth rates as a function of dual parameters temperature and chemical difference composition are studied, and charge-charge correlation functions are calculated to measure the degree of ordered growth for low-temperature crystals. The effects of varying the crystallographic orientation of the slabs were explored, with the slabs labeled according to the slab perpendicular (z) direction i.e. $[\bar{1}\bar{1}1]$ and $[001]$. The qualitative behaviors of growth crystal for different environments are discussed. In $A(BB'B'')O_3$ systems, we investigate a scenario when a fraction of tetravalent B'' ions are mixed in. In our growth simulations, these tetravalent ions do not appear to mix at low temperatures, choosing instead to phase-separate from the pure crystal. To further study this, we carried out the static total energy calculations for two different crystallographic orientations ($[\bar{1}\bar{1}1]$ vs $[001]$), atomic configurational orderings ($[111]_{1:2}$ vs $[111]_{1:1}$) and tetravalent structural models (phase separation vs random mixing). In addition, free-energy calculations for fixed slab configurations are explored in four different tetravalent ions percentages. Results are presented in Section 4.2.

4.1 Crystal Growth

The growth process is a function of temperature kT , chemical potential difference $\Delta\mu$, and the Coulomb interaction. These parameters are fixed throughout a given simulation. As previously described in Section 3.2, the rates of adsorption and evaporation are constructed from kT , $\Delta\mu$ and ΔE_B . Any choices of these parameters will therefore determine the crystal physical behaviors as well as their growth rates. Crystal growth is a competing process between adsorption and evaporation. In practice, we establish a fixed adsorption rate from a constant kT and $\Delta\mu$ but the evaporation rate is updated in each step of the growth simulations. The chemical potential difference $\Delta\mu$ plays a part in determining the rate of adsorption (see Eq. 3.23) while the temperature kT which appears in both Eq. 3.23 and Eq. 3.24 is responsible for the energy scale of the systems. In the simulations, we explored kT in the range of 0.025 to 2.4 while $\Delta\mu$ lies between -3.0 to 1.0. It is shown later on that the ordered crystals only grow within the certain range of these parameters depending on type and crystallographic orientations. As discussed in Section 3.1 and in the Appendix A, the potential $v(l' - l)$ is tabulated and stored in reduced units in order to easily extract it when needed in the simulations. The energies ($\Delta\mu$ and $E_B(C)$) are scaled by $\xi \equiv 1/\epsilon a$. However, there is only one free parameter between ξ and the temperature $k_B T$, which sets the energy scale of the problem, and the temperature $k_B T$ is given in reduced units. For example, for $a \sim 8$ a.u. and $\epsilon \sim 10$ (typical values of BMN solid solutions) in Eq. (3.4), 1350 C corresponds to $k_B T = 0.41$ in the simulation.

In the simulation, the lattice is initialized with $L \times L \times H_0$ matrix size which is configurationally decorated according to the species and charges of interest. The parameter L denotes the width and length of the surface supercell while H_0 denotes the initial (substrate) thickness of the crystal. The substrate lattice is subjected to periodic boundary conditions perpendicular to the growth direction. At a given kT and $\Delta\mu$, adatoms are

evaporated or adsorbed according to the Monte Carlo techniques described in Section 3.2. The crystal evolves until an acceptable thickness H or the MC step is reached. We define an MC step as an L^2 array and each time step is therefore $1/(L^2)$.

As an overview, Figs. 4.3 and 4.5 present a comparison of simulations of the simple $\text{III}_{1/2}\text{V}_{1/2}$ rocksalt alloy and a $\text{II}_{1/3}\text{V}_{2/3}$ heterovalent alloy such as BMN. (All substrates in our simulations have neutral surface layers). We measure the growth rate of crystal based on the KMC dynamics. The quantitative growth behaviors are described through the rate of growth which gives the number of adatoms gained with respect to KMC “real time”. If N_G adatoms are gained in m MC steps (each defined as one attempt at the procedure outlined in Section 3.2), the growth rate is defined as

$$\Gamma = \frac{N_G}{w_a \sum_{i=1}^m \Delta t_{\text{real}}(i)}. \quad (4.1)$$

Note that as defined the growth rate Γ is renormalized by the absorption rate. The growth rate is plotted as a function of the chemical potential for a range of temperatures. The rocksalt (NaCl) structure has layers of positive and negative charges alternating along the $[111]$ direction and exhibits the $[111]_{1:1}$ ordering. It typifies the crystal ordering of a wide variety of materials, including some of the heterovalent binaries perovskite alloys: $\text{II}_{1/2}\text{VI}_{1/2}$ ($q_B = \pm 2$) or $\text{III}_{1/2}\text{V}_{1/2}$ ($q_B = \pm 1$), which exhibit rocksalt B-site chemical order. The rocksalt structure is the simplest crystal our ionic model can grow, and we observe faster growth and longer range of ordered crystals compared to other structures. By contrast, in the $\text{II}_{1/3}\text{V}_{2/3}$ heterovalent binary BMN the equilibrium state shows $[111]_{1:2}$ ordering of two layers of metal group V ($q_B = +1$) alternating with one layer of the group II ($q_B = -2$) atom. Our interest in the BMN type crystal is due to its complex ordering which could allow us to further explore the efficacy of the ionic model. Both the rocksalt and BMN simulations were initialized with a 20-layer thick slab, with perfect $[111]_{1:1}$ and $[111]_{1:2}$ ordering, respectively. The rocksalt simulation used a 2-D 12×12 supercell, while the BMN simulations were done mostly with 6×6 supercells, although some simu-

lations with 12×12 and 15×15 were carried out to verify that the finite-size effects were small. The rocksalt structure simulations ran for $1,000L^2$ MC steps, up to a maximum thickness of 100 layers (including the initial thickness). For BMN, $10,000L^2$ MC steps were used, because for a given temperature and $\Delta\mu$ growth was significantly slower. As described above, an MC step is a simulating sweep through a single surface layer and is defined as L^2 . The simulation is terminated when either the maximum MC steps or thickness is reached. In Fig. 4.1 and Figure 4.2, we show visualizations of the grown BMN and rocksalts crystals to illustrate the simulation environments and the growth orders. The atomic ordering is demonstrated as the 1:1 order in rocksalt and 1:2 order in BMN. Fig. 4.1 shows structural patterns for the growth directions of BMN i.e. $[001]$ and $[\bar{1}\bar{1}\bar{1}]$. While both configurations indicate the same ordering crystal, the simulation results shows the evidence of a more ordered growth for the $[001]$ slab. Fig. 4.2 shows different types of observed growth, layer-by-layer growth and rough growth for rocksalt crystals. In the layer growth mode, adatoms are layers filled sequentially. The final crystal appears to have fewer imperfections and achieve more ordered growth. In contrast, rough growth usually occurs at very high adsorption rates where adatoms tend to adhere on the surface with less regard for charge-mismatch, and evaporation becomes insufficient to restore the ordering. In addition, the individual “towers” are developed on crystal surface.

The two sets of curves in Fig. 4.3 and 4.5 are qualitatively similar and are consistent with the model and the expected behavior of crystal growth. What is not evident from the figures, however, is the degree of order in each simulation. For a given temperature, as $\Delta\mu$ increases, the adsorption rate in Eq. (3.23) increases, and adatoms are more likely to stick. For fixed $\Delta\mu$, as $k_B T$ decreases, the adsorption rate will increase, but more importantly, the “selectiveness” of evaporation will increase. A lower $k_B T$ will, in effect, increase the energy differences between competing configurations. The direct result, as growth is concerned, will be that adatoms will increasingly prefer to have more instead of less neighbors with correct charge ordering (layer-by-layer growth vs. rough growth), and

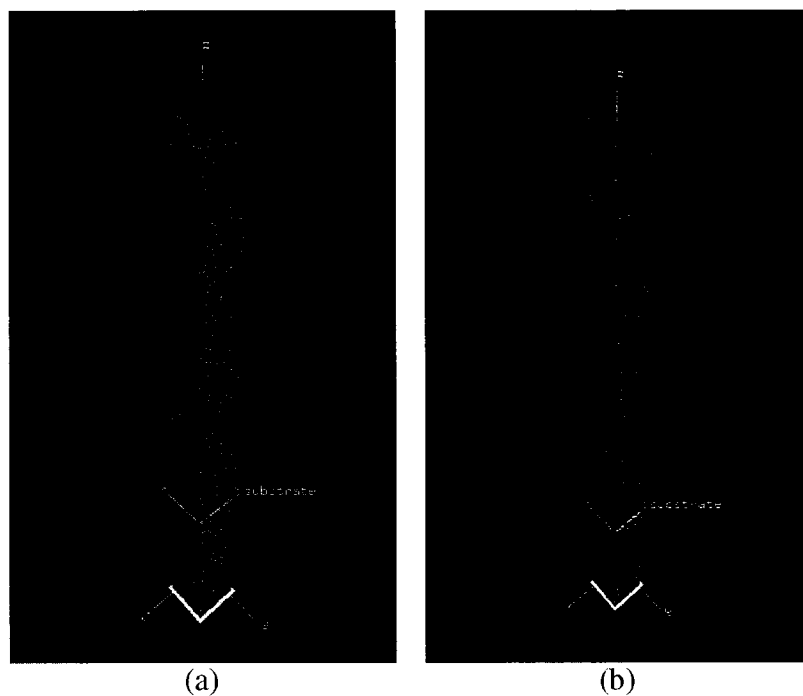


FIG. 4.1: Visualizations of grown BMN crystals. Shown are 6×6 supercells with: (a) growth direction along $[001]$, $k_B T = 0.1$ and $\Delta\mu = -1.0$; (b) growth direction along $[\bar{1}\bar{1}1]$, $k_B T = 0.1$ and $\Delta\mu = -1.1$. The latter gives less ordered growth.

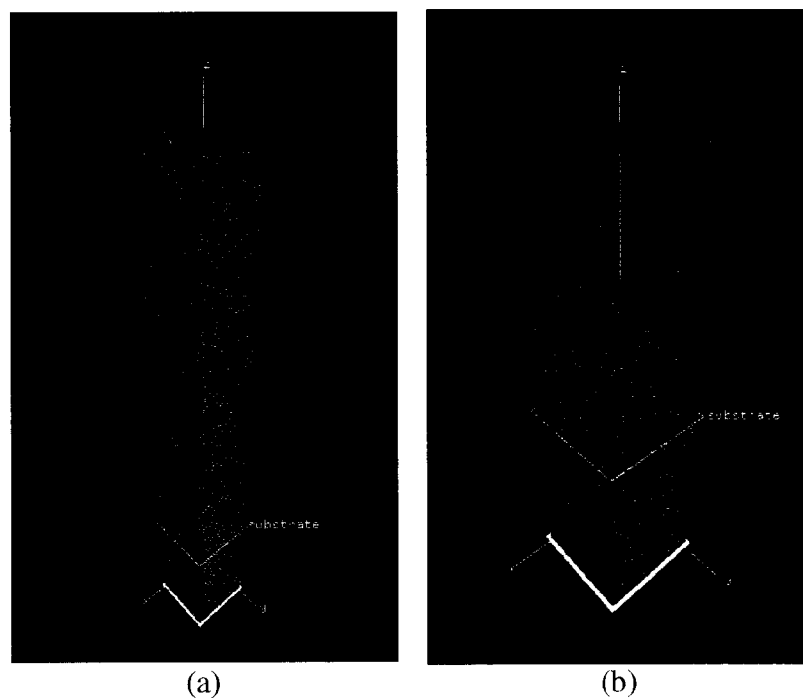


FIG. 4.2: Visualizations of rocksalt crystals. Shown are 12×12 supercells with: (a) $k_B T = 0.1$ and $\Delta\mu = -0.625$; (b) $k_B T = 2.4$ and $\Delta\mu = 0.0$. The substrate indicates 20 layers of initial growth seed. While the first diagram shows the layer-by-layer growth, the second one illustrates a rough growth mode where the evidence of “towers” is visible.

adatoms with the same charge will seem more repulsive. For very high $\Delta\mu$, adatoms will stick anywhere, no matter what the location or ionic adversity is, and the growth rate will be high. Alternatively, if the temperature becomes too high, the crystal will evaporate and result in negative growth.

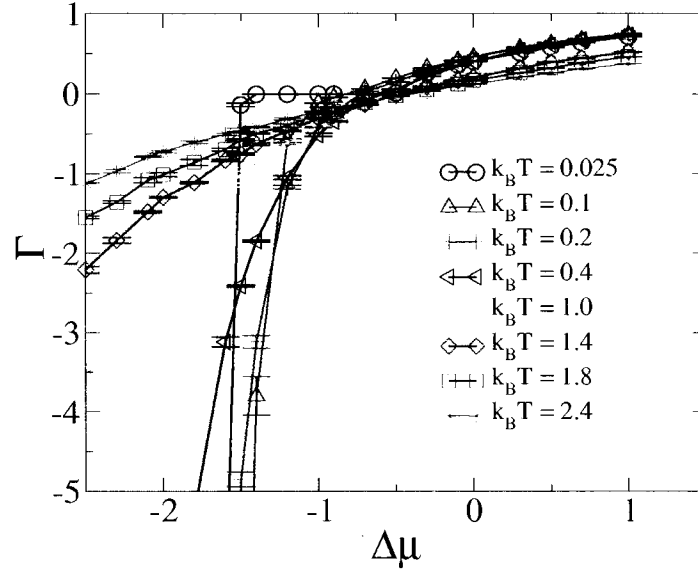


FIG. 4.3: Rocksalt growth rate vs. chemical potential for a [001] slab. Behaviors from various temperatures are also compared.

In addition, we focus on the region where rocksalt and BMN crystals make a transition from a negative growth into a positive one as shown in Fig. 4.3 and Fig. 4.5 respectively. Following from the above observation, the crystals growth rates increases in the region of high $\Delta\mu$. As might be expected, the positive growth of BMN is described in a much narrow range of parameters than those of rocksalt.

To examine the degree of ordering, we computed the charge-charge correlation function. The Fourier transform of this correlation function, which we will denote by $\eta(\mathbf{k})$, gives the structure factor:

$$\eta(\mathbf{k}) = \alpha \sum_{l'} q_l q_{l'} \exp(-i\mathbf{k} \cdot \mathbf{l}') \quad (4.2)$$

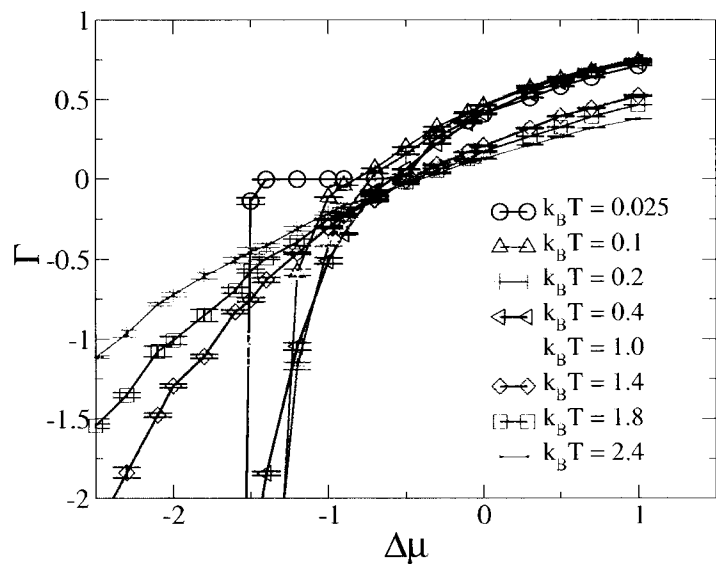


FIG. 4.4: An expanded plot of rocksalt growth rate vs. chemical potential for a [001] slab. Behaviors from various temperatures are also compared.

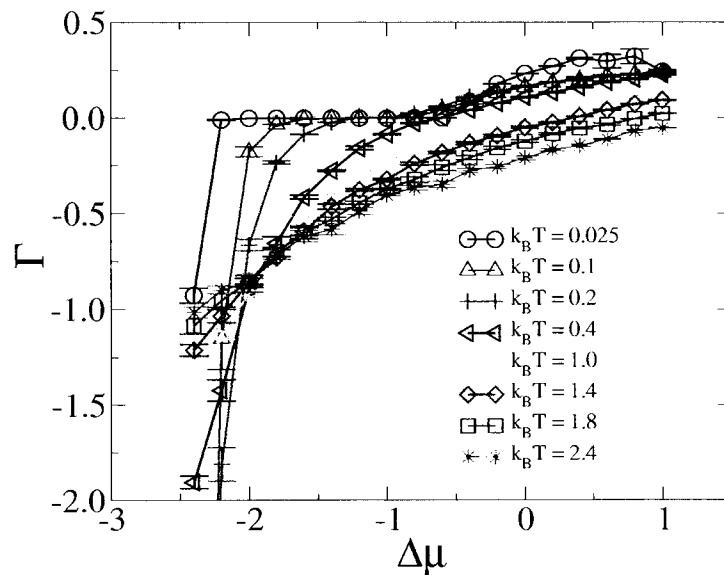


FIG. 4.5: BMN growth rate vs. chemical potential for a $[\bar{1}\bar{1}1]$ slab. Behaviors from various temperatures are also compared.

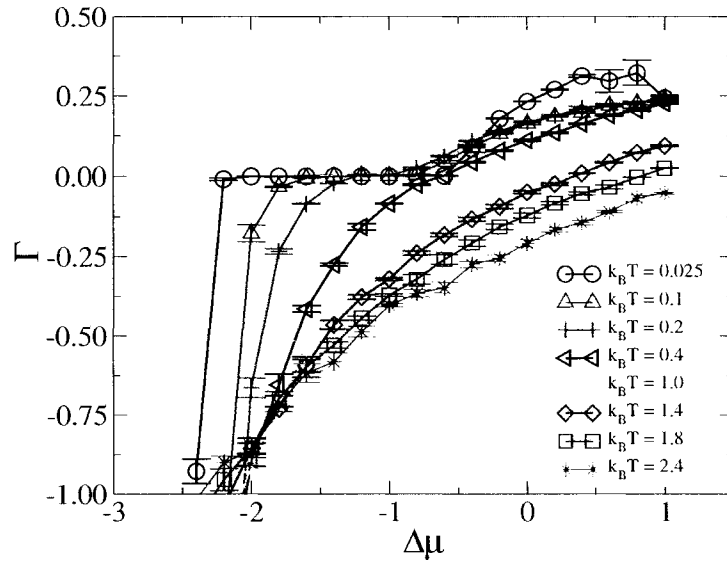


FIG. 4.6: An expanded plot of BMN growth rate vs. chemical potential for a $[\bar{1}\bar{1}\bar{1}]$ slab. Behaviors from various temperatures are also compared.

where α is the normalization factor, and \mathbf{k} is the wave vector in the Brillouin zone of the unit cell. The magnitude of $\eta(\mathbf{k})$ characterizes the B-site order, e.g., a large value of η at $\mathbf{k} = \frac{2\pi}{a} (\frac{1}{2}, \frac{1}{2}, \frac{1}{2})$ indicates a strong $[111]_{1:1}$ order while one at $\mathbf{k} = \frac{2\pi}{a} (\frac{1}{3}, \frac{1}{3}, \frac{1}{3})$ indicates a strong $[111]_{1:2}$ order.

The growth rate Γ and the charge-charge structure factor η are plotted in Figs. 4.9-4.12. In each figure, the displayed range of $\Delta\mu$ was chosen to coincide with the range where the order parameter η decreases from nearly unity (perfect order) to essentially zero (disorder). As $\Delta\mu$ increases the adsorption rate increases, but the growth is disordered and there is greater surface roughness. Indeed there is only a limited range where ordered growth occurs. The grown crystal structures are consistent with the observed ground state configuration of rocksalt (Fig. 4.9) and BMN (Fig.'s 4.10-4.12). The most striking difference between the growth behaviors of rocksalt and BMN is the enormous reduction of the growth rate of BMN compared to that of the rocksalt structure. Three distinct regions can be seen in the figures. The first region has $\eta \sim 1$, and the growth rate increases monotonically with increasing $\Delta\mu$. The next is the transitional region where η

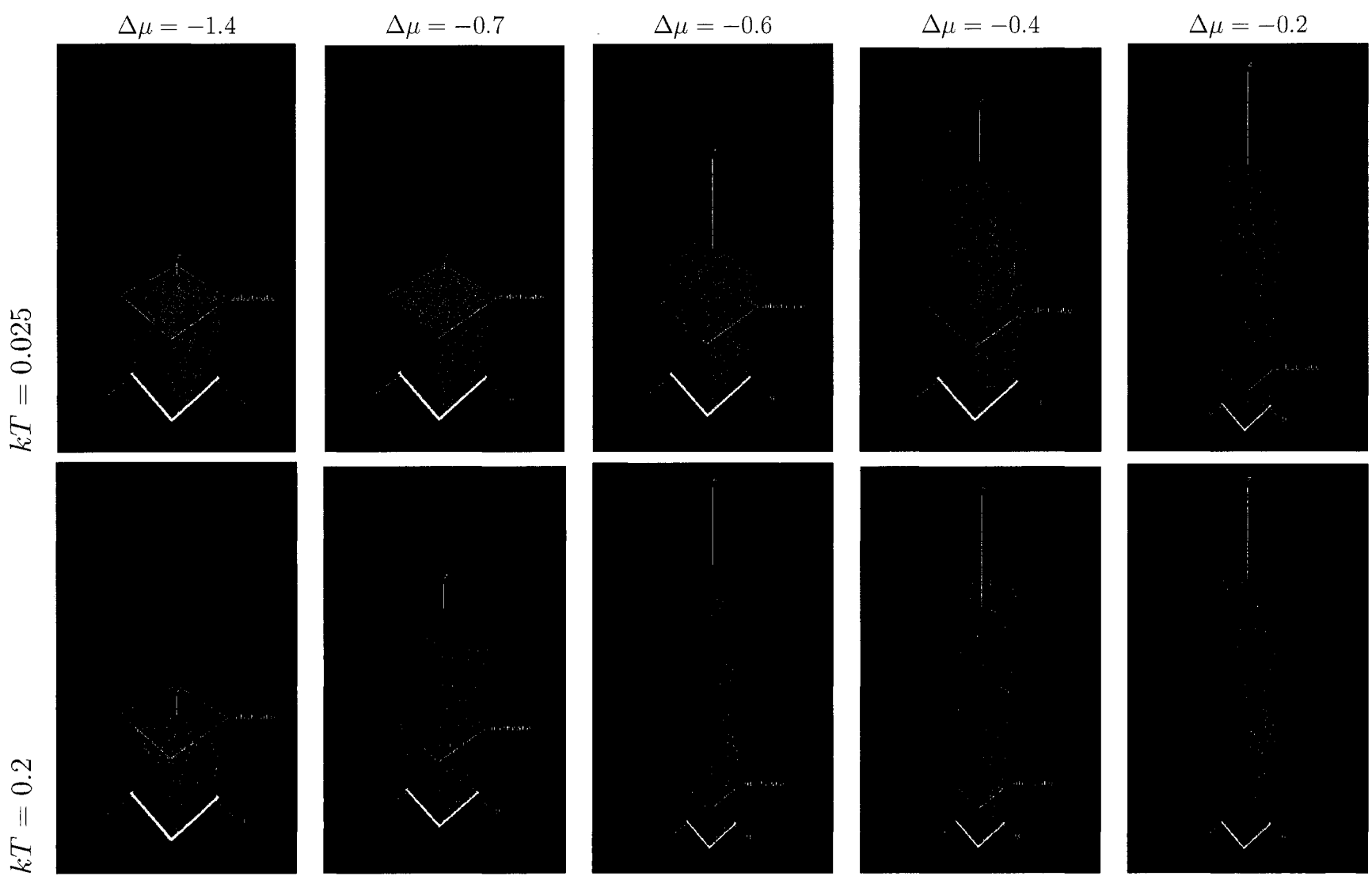


FIG. 4.7: Illustrative results of the rocksalt growth for different $\Delta\mu$ at low temperature $kT = 0.025$ and 0.2 . The simulations were run for $12 \times 12 \times 100$ matrix with 1000 MC steps.

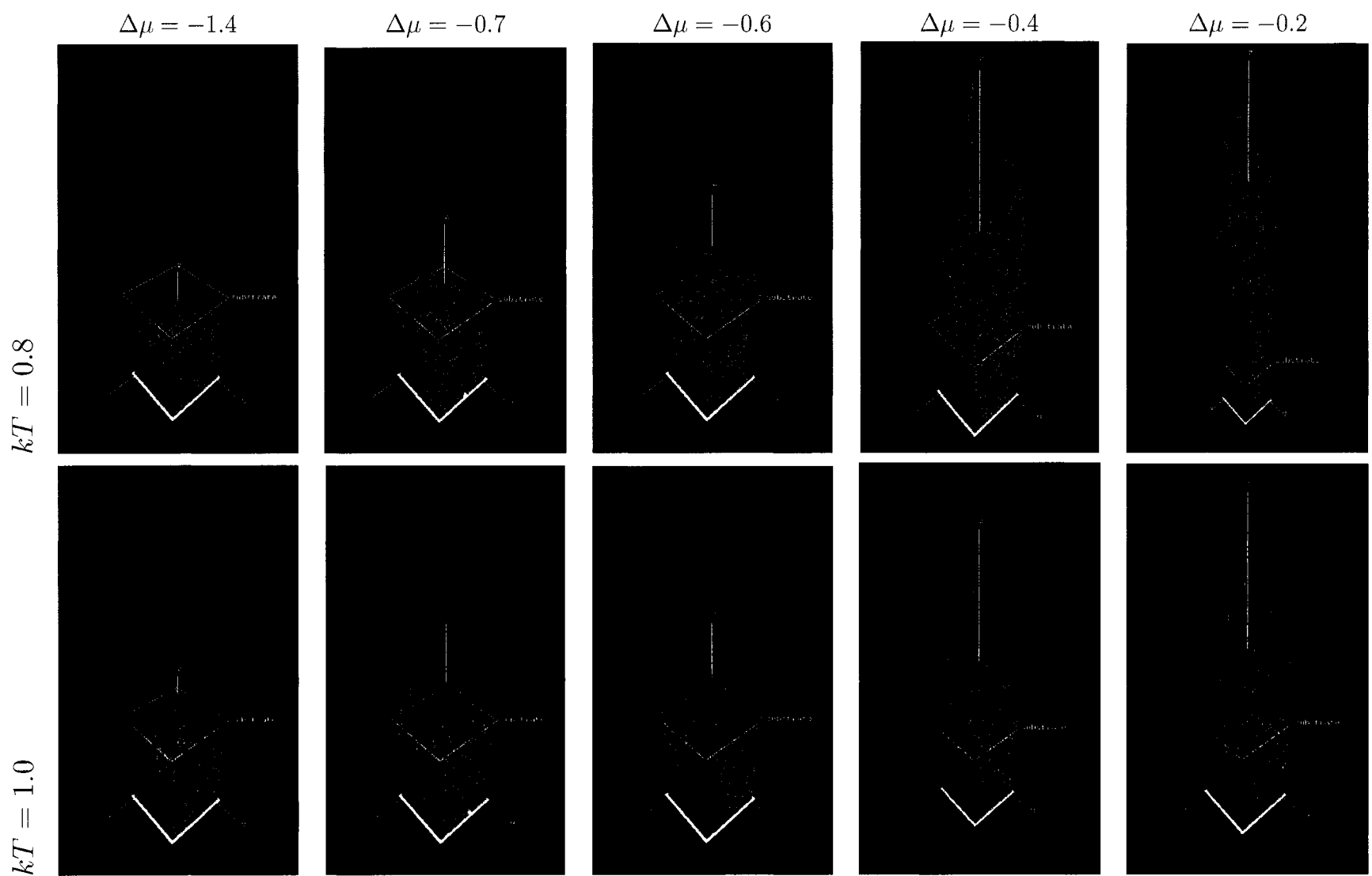


FIG. 4.8: Illustrative results of the rocksalt growth for different $\Delta\mu$ at temperature $kT = 0.8$ and 1.0 . The simulations were run for $12 \times 12 \times 100$ matrix with 1000 MC steps. At this high temperature, towers are more visible than those of lower temperatures (Fig. 4.7).

decreases rapidly. In this region the rocksalt growth rate increases as a function of $\Delta\mu$, while the BMN growth rate is relatively constant. Also note that as η starts to decrease there is an initial decrease in the growth rate, likely due to additional evaporation of energetically unfavorable configurations. In rocksalt, such ionic adversity is less pronounced, and consequently Fig. 4.9 shows only a slight hint of this change in Γ . In the last region $\eta \sim 0$. As $\Delta\mu$ increases there is a sudden onset of larger Γ , but the resulting crystals are disordered.

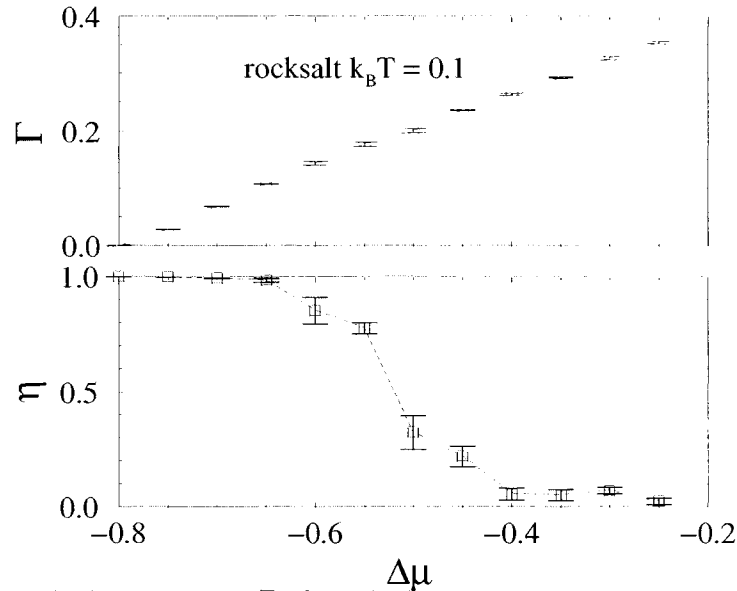


FIG. 4.9: Rocksalt growth rate Γ of Eq. (4.1) (top panel) and 1:1 order parameter $\eta(\mathbf{k} = \frac{2\pi}{a}(\frac{1}{2}, \frac{1}{2}, \frac{1}{2}))$ (bottom panel) vs. chemical potential. The temperature is $k_B T = 0.1$ and the growth direction is [001]. A 12×12 supercell is used, with 1000 MC time steps.

We next attempted to model the growth of BMN-BZ $(1-x)$ ($\text{Mg}_{1/3}\text{Nb}_{2/3}$) + x Zr solid solutions. In the electrostatic Hamiltonian in Eq. (3.4), tetravalent Zr corresponds to a neutral charge $q_t = 0$, so sites occupied by Zr have zero interaction energy. As in the simulations of pure BMN systems, the chemical composition determines the probabilities with which different charge species are adsorbed at the surface. In the initial substrate, tetravalent ions with the corresponding concentration were incorporated, using random mixing (next section). With a 1:2-ordered substrate, we studied concentrations $x \sim 10\%$,

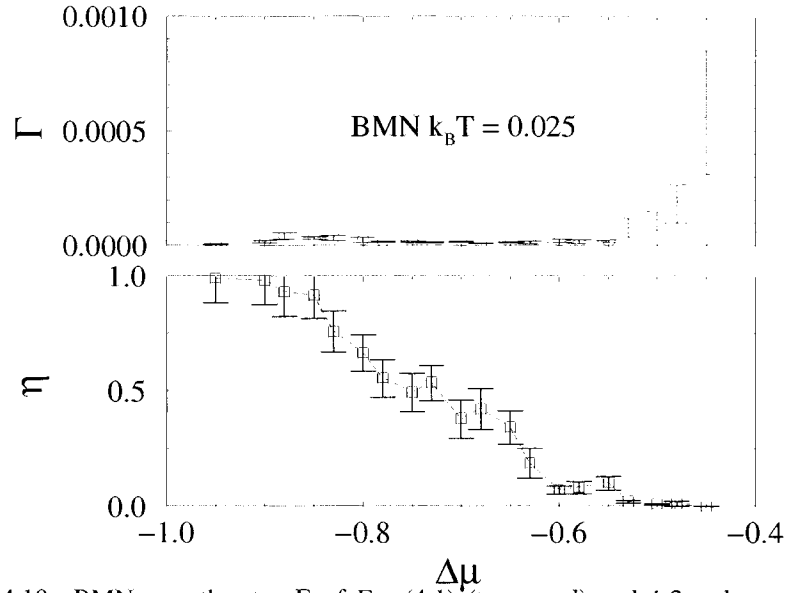


FIG. 4.10: BMN growth rate Γ of Eq. (4.1) (top panel) and 1:2 order parameter $\eta(\mathbf{k} = \frac{2\pi}{a}(\frac{1}{3}, \frac{1}{3}, \frac{1}{3}))$ (bottom panel) vs. chemical potential. The temperature is $k_B T = 0.025$ and the growth substrate direction is $[\bar{1}\bar{1}1]$. A 6×6 supercell is used, with 300,000 MC time steps.

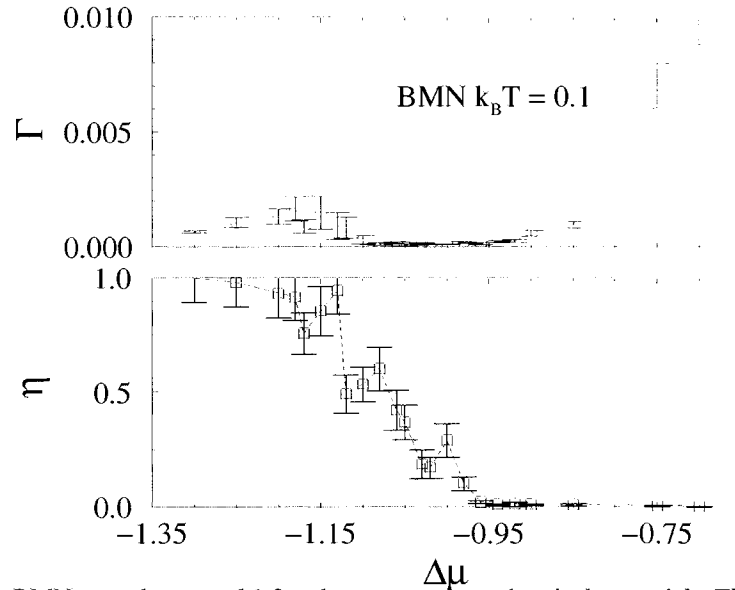


FIG. 4.11: BMN growth rate and 1:2 order parameter vs. chemical potential. The temperature is $k_B T = 0.1$. Other parameters are the same as in Figure 4.10.

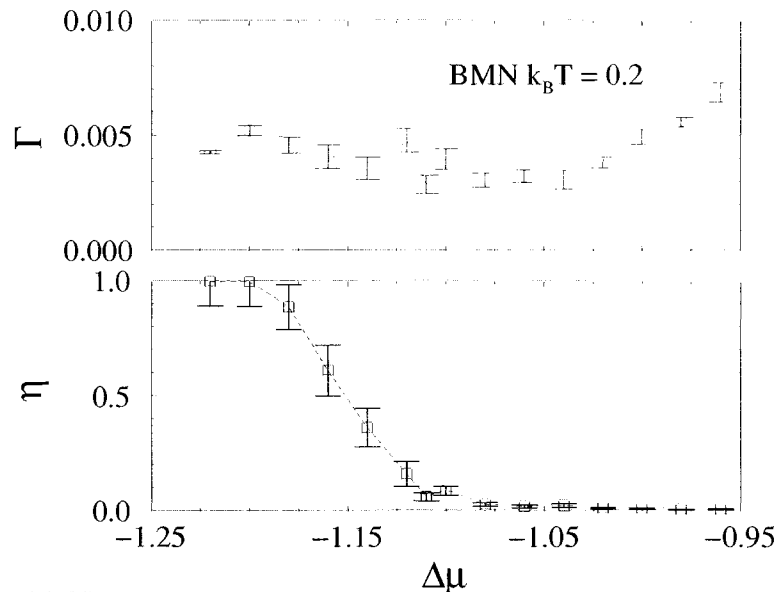


FIG. 4.12: BMN growth rate and 1:2 order parameter vs.chemical potential. The temperature is $k_B T = 0.2$. Other parameters are the same as in Figure 4.10 .

with temperatures of $k_B T \sim 0.1$ to 0.2 , and varying the chemical potential $\Delta\mu \sim -1.0$ to -0.5 . Very little incorporation of the tetravalent ions occurred. We found similar results with an initially 1:1-ordered substrate (random-site model; see below), where a wider range of x was explored. Again the order of the substrate was not sufficient to induce the incorporation of tetravalent ions in the growth phase. Instead the system seemed to favor evaporating the adsorbed tetravalent ions more than the charged particles, to grow pure BMN.

4.2 Energy Calculations

The initial attempts to study systems with tetravalent ions suggest that the simple electrostatic effective Hamiltonian has obvious limitations in describing these solid solutions. To further study the inability to incorporate tetravalent ions at low temperatures, we examined the total energy per particle ε_N of fixed slab configurations of B-site order. A phase separated model, in which all the tetravalent adatoms were situated in the

outermost surface layers as depicted in Fig. 4.13a and Fig. 4.14a was compared with various structural models that incorporated tetravalent ions. In each model, the calculations were performed for two different configurational B-site orderings of the +2 and +5 ions ($q_{\mathbf{l}} = -2, +1$, respectively). These configurations were the 1:1 and 1:2 layering along [111] directions.

The $[111]_{1:2}$ ordering corresponds to the $x = 0$ order of BMN, with a layer of $q_{\mathbf{l}} = -2$ alternating with two layers of charge $q_{\mathbf{l}} = +1$ along the [111] direction. We chose the $[111]_{1:1}$ ordering to correspond to the random-site model [6], which is observed in the BMN-BZ equilibrium simulations for $x > 0.05$ [13, 26]. In the random-site model there are [111] layers of $q_{\mathbf{l}} = +1$ alternating with a mixed layer of charges $q_{\mathbf{l}} = -2, +1, 0$ which is schematically shown in Figure 4.14. The random-site model is meant to represent the presence of short-range B-site order from experimental observations. No long-range ordering has been observed. Nevertheless in our simple model here we will fix the ordered $q_{\mathbf{l}} = +1$ layers and choose the mixed layers to be a random mixture of $(-2)^{\frac{2}{3}(1-x)}(+1)^{\frac{1}{3}(1-4x)}(0)^{2x}$.

We first examine finite-size effects in Fig. 4.15, which plots ε_N as a function of slab thickness for various 2-D supercells containing no tetravalent ions, for $[111]_{1:2}$ ordering with two different choices of $\{\mathbf{a}_1, \mathbf{a}_2\}$. In each slab geometries, three different lattice sizes, 12×12 , 15×15 , and 18×18 , were also studied in order to verify the size effects on the plane of periodic boundary condition. Results for [001] and $[\bar{1}\bar{1}1]$ slabs are shown, both of which correspond to neutral surface layers. As $H \rightarrow \infty$, $\varepsilon_N \sim \varepsilon_N^B + \text{const.}/H$ is as expected, where the constant ε_N^B represents the average bulk value and H is the slab thickness. Moreover, energies that correspond to the three different periodic cell sizes are almost identical for both [001] and $[\bar{1}\bar{1}1]$ slabs.

A comparison of ε_N between $[111]_{1:1}$ and $[111]_{1:2}$ ordering with and without randomly mixed 10% tetravalent ions is shown in Fig. 4.16. The 1:1 ordered crystal has a higher energy than the 1:2 ordered crystal, which is consistent with our results from the

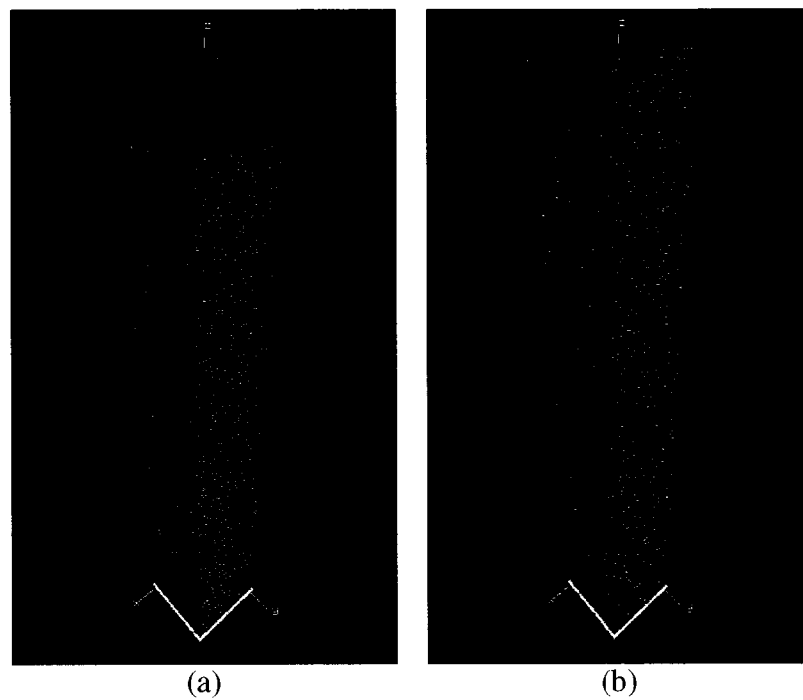


FIG. 4.13: Visualizations of 1:2 ordering BMN crystals. Shown are 100 layers of the 15×15 supercell. Tetravalent concentration is 10 % with the configuration shown in (a) phase separated model; (b) random mixing model.

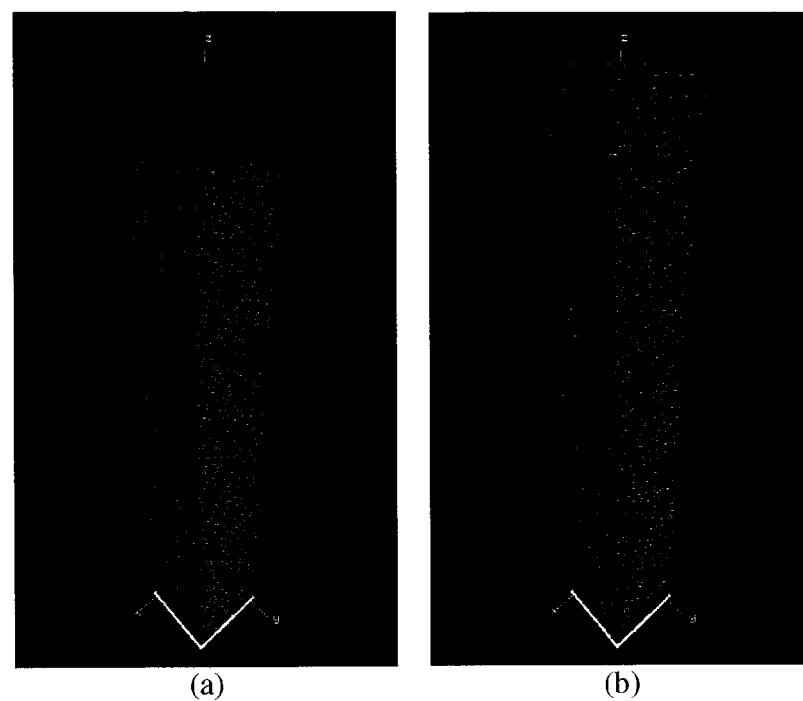


FIG. 4.14: Visualizations of 1:1 ordering BMN crystals. Shown are 100 layers of the 15×15 supercell. Tetravalent concentration is 10 % with the configuration shown in (a) phase separated model; (b) random mixing model.

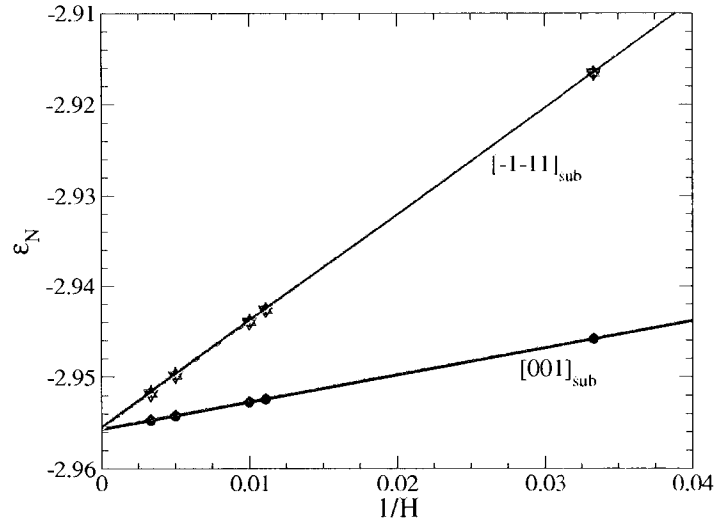


FIG. 4.15: Total energy per particle for B-site $[111]_{1:2}$ ordering as a function of slab thickness $1/H$ and slab crystallographic orientation. Each set has three barely distinguishable curves, corresponding to three lattice sizes: 12×12 , 15×15 , and 18×18 .

growth simulation and with the observed $x = 0$ ground state configuration of BMN. We also see that the finite-size effect for the 1:1 ordered system is similar to the 1:2 ordered system, again with rapid convergence with slab thickness H . When the 10% tetravalent concentration is present, the energy of the 1:1 ordered crystal remains almost unchanged within statistical error especially in the limit of a large H where the energies are nearly identical. This is also confirmed in Fig. 4.18. In contrast, ϵ_N of the 1:2 ordered crystals rapidly increases with increasing x approximately linearly as shown in Fig. 4.18. However, the 1:2 ordered crystals energy is still less than those of the 1:1 ordered, which results from the less favorable configuration when adding tetravalent ions.

In the following, we studied size effects of crystals with incorporated tetravalent ions. Fig. 4.17 plots ϵ_N for $[111]_{1:2}$ ordering as a function of slab thickness for various concentrations of randomly mixed tetravalent ions, using a $[001]$ slab and 15×15 supercell. These calculations are for a random distribution of +0 (tetravalent) ions replacing -2 or +1 ions in an otherwise perfectly ordered $[111]_{1:2}$ slab at each thickness H as shown schematically in Fig. 4.13b. We studied the effect of x to the energy up to

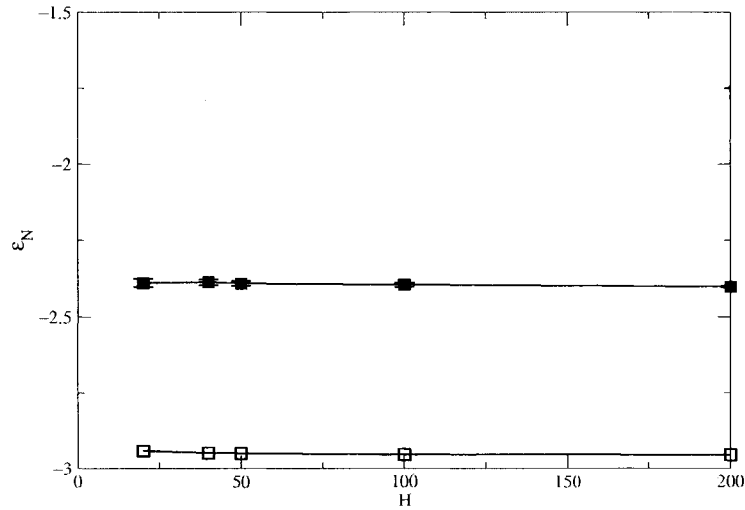


FIG. 4.16: Total energy per particle vs. Height. Closed symbols denote results obtained with 10% tetravalent concentration, and open symbols denote those without. $[111]_{1:1}$ is represented with yellow line, while the blue line correspond to the $[111]_{1:2}$ ordering. Results with $[111]_{1:1}$ atomic ordering are denoted by circles and those with $[111]_{1:2}$ are denoted by squares.

25% of tetravalent concentration which is the highest allowed concentration in order to maintain neutral-charged crystals. We can see that ε_N increases rapidly as the percentage tetravalent concentrations increase. In addition, within statistical error bars, the asymptotic H -dependence is similar to that without tetravalent ions.

Fig. 4.18 plots ε_N as a function of tetravalent concentration x for random-mixing and phase-separation models, showing results for $[111]_{1:1}$ and $[111]_{1:2}$ ordered of 12×12 system size with $H = 200$ and $[001]$ slabs. For the phase-separation model, the total number of ions includes the outermost layers of tetravalent ions. For random-mixing, ε_N increases linearly with x for $[111]_{1:2}$ ordering while it is essentially independent of x for $[111]_{1:1}$ ordering. In the phase-separation model, ε_N increases linearly for both orderings. These results show that phase separation is favored for the $[111]_{1:2}$ ordering, while random mixing is favored by $[111]_{1:1}$ ordering.

Fig. 4.18 illustrates why the growth simulations failed to incorporate tetravalent ions at low temperature. In the electrostatic model, the 1:2 ordered state is the ground state and

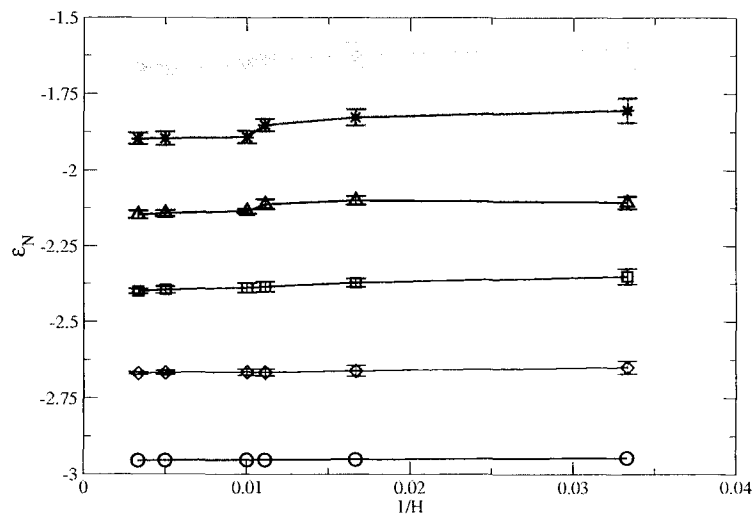


FIG. 4.17: Size-effect of 1:2 ordering for various tetraivalent concentrations. Total energy per particles as a function of slab thickness $1/H$ for [001] slabs and 15×15 system size. The curves descendingly correspond to 25%, 20%, 15%, 10%, 5% and 0%.

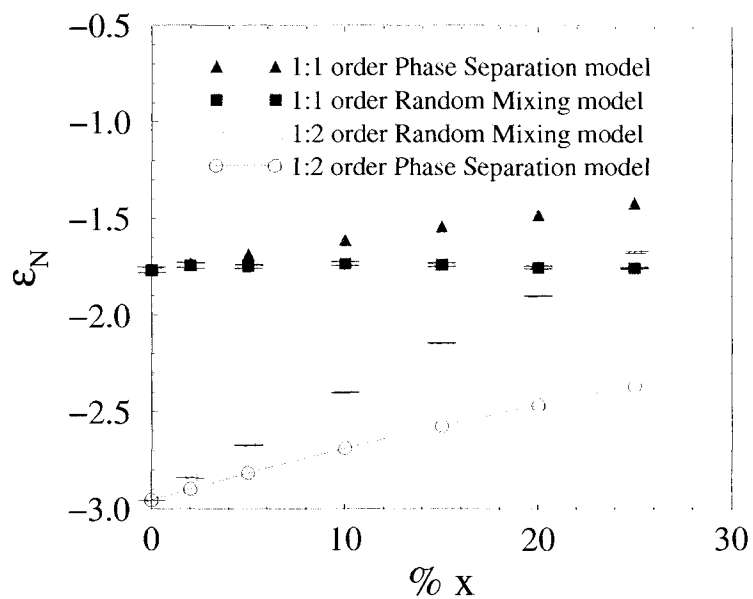


FIG. 4.18: Total energy per particle vs. tetraivalent concentration x for random-mixing and phase-separation models. Results are shown for $[111]_{1:1}$ and $[111]_{1:2}$ ordered 12×12 [001] slabs ($H = 200$).

is optimally ordered. The potential energy between any charge and all other charges in the system is negative. For example, with a 18×18 slab this potential energy is ~ -5.92 for a -2 charge and ~ -1.48 for a $+1$ charge. Thus, replacing a charge (either -2 or $+1$) by a neutral tetravalent ion in this state raises the total energy of the system, while a phase-separated configuration in which the tetravalent ion is placed away from the ordered slab keeps the total energy unchanged. To examine this more closely, we calculated the free-energy ($F = \varepsilon_N - TS$), where S is the mixing entropy due to the incorporated tetravalent ions. Fig. 4.19 plots the free-energy as a function of temperature for four concentrations of tetravalent ions. The free energy of the phase-separated 1:2 ordered slabs is constant in our model, because it is perfectly ordered and has vanishing entropy. The free energy of the phase-separated 1:1 ordered slabs decreases with increasing temperature, despite the perfectly ordered outermost layers of tetravalent ions, due to the mixing entropy of the random layers with -2 , $+1$, and 0 charges. In all cases in Fig. 4.19, the phase-separated 1:2 ordered slabs have the lowest free energy at low temperatures, where ordered crystal growth occurs in our simulations, but at temperatures between $k_B T \sim 1 - 2$ the 1:2 ordered and the 1:1 ordered random mixing models start to be favored.

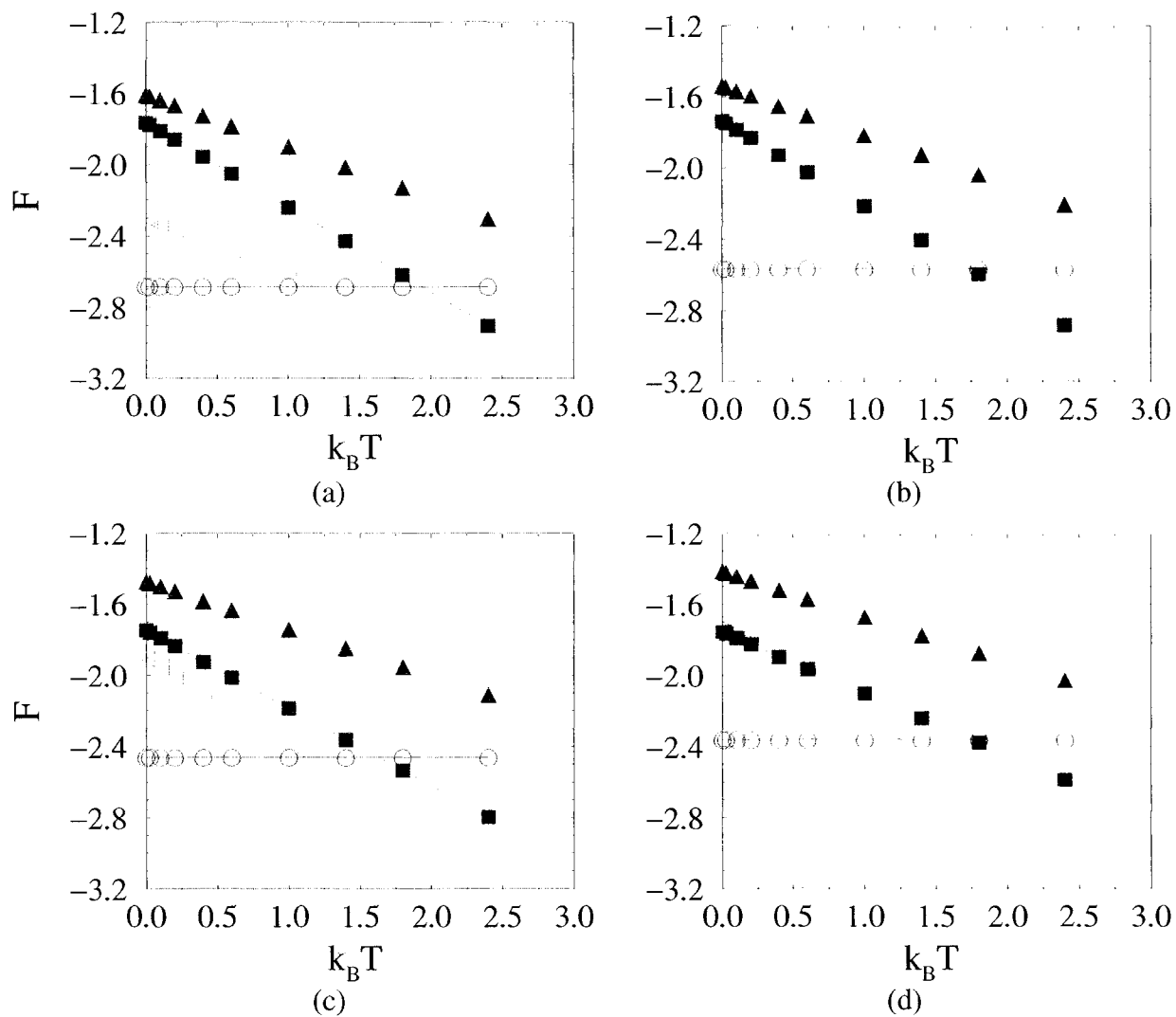


FIG. 4.19: Free energy of BMN crystal for (a) 10% (b) 15% (c) 20% (d) 25% tetraivalent concentrations. Symbols have the same meaning as in Fig. 4.18.

CHAPTER 5

Concluding Remarks (Kinetic Monte Carlo Simulation of Crystal Growth)

5.1 Discussion

There are striking differences between the growth behavior of the $\text{III}_{1/2}\text{V}_{1/2}$ rocksalt ordered structure and the $\text{II}_{1/3}\text{V}_{2/3}$ BMN structure. The ordered rocksalt structure forms over a wide range of $\Delta\mu$ (absorption rates) as shown in Figure 4.3. By contrast, ordering of the 1:2 structure in BMN type crystals is more difficult to achieve experimentally [27, 28]. When these materials are initially synthesized, they crystallize in a disordered structure. With extended annealing the 1:2 structure is approached. [27] As discussed by Davies *et al.* [27], the initial synthesis and processing are controlled by irreversible kinetic processes rather than by thermodynamic factors, and a more correct description of the formation of the 1:2 ordered structures is in terms of the nucleation and growth of small ordered domains with increasing annealing time and temperature. Eventually large (>100 nm) 1:2 ordered domains are observed.[27, 28] The need for long annealing times is consistent with our simulations. Figures 4.10 - 4.12 show that the range of $\Delta\mu$ where

ordered 1:2 growth occurs narrows as the temperature increases from $k_B T = 0.025$ to 0.2. In this range, the growth rate is approximately constant as a function of $\Delta\mu$. Moreover, when ordered crystal growth occurs, the BMN growth rate is much smaller than that of the rocksalt structure at the same temperature. Highly ordered growth was possible in the BMN simulations but required low temperatures and a delicate balance with the chemical potential. Neither of these requirements is likely to be met under experimental synthesis conditions. At temperatures corresponding to the actual sintering temperature of BMN ($k_B T \sim 0.5$), large growth rates can be achieved, as shown in Figure 4.5, but the growth is highly disordered. The long annealing times allow the slow formation of the 1:2 ordered regions. In our KMC simulations, diffusion processes are excluded so there can be no annealing. We also note that the growth rate was sensitive to the slab orientation. For example, we found that growth rate along $[\bar{1}\bar{1}1]$ direction was almost an order of magnitude larger than that along $[001]$, while growth with charged surfaces along $[111]$ was extremely slow.

Our results are also qualitatively consistent with the long experimental history of failed attempts to coarsen the 1:1 ordered nanoscale domains in PMN type crystals. Prior to the experiments of Akbas and Davies [28], the 1:1 ordered regions were apparently limited to nanoscale size and represented only a small volume fraction of the crystal. The space-charge model, which was invoked to explain this behavior, hypothesized that the 1:1 ordered regions arose from a rocksalt ordering of the -2 and +1 B-site charges, implying charge-imbalanced 1:1 domains. The apparently limited size of these domains could be explained by the rapidly increasing energy of larger domains due to Coulomb repulsion. With careful annealing at much higher temperatures than had previously been tried, however, some fully 1:1 ordered crystals were synthesized [28]. Our calculations show that long-range ionic interactions favor the growth of disordered crystals, and ordering occurs only after annealing. Moreover, ionic interactions appear to favor the 1:2 ordering. However, entropic contributions to the free energy and short-range covalent interactions

tend to favor 1:1 ordering. Covalent bonding is negligible for Ba ions but very important for Pb ions. Thus there is a delicate competition between 1:2 and 1:1 ordering for doping with small concentrations of the tetravalent ions in $(1-x)\text{BMN}-x\text{BZ}$ and $(1-x)\text{PMN}-x\text{PT}$. In $(1-x)\text{BMN}-x\text{BZ}$, there is a crossover from 1:2 to 1:1 ordering as x increases to about 5%, while in $(1-x)\text{PMN}-x\text{PT}$, the stronger short-range covalent bonding of Pb favors 1:1 ordering at all concentrations.

For pure systems, our minimal paradigm for growth simulations captures the differences in growth rate and ordering between rocksalt-type and BMN-type crystal growth. This indicates that the simple ionic model is a reasonable starting point for describing the growth of perovskite solid solutions. More direct and quantitative comparisons with experiment will require additional ingredients such as short-range interactions and the inclusion of diffusive processes.

For systems with tetravalent ions, our results show that the ground state is a phase-separated state of tetravalent ions and 1:2 ordered BMN over a wide range of tetravalent compositions. On the other hand, equilibrium simulations of the ionic model [13, 26] suggest that for $x > 0.05$ the 1:1 ordering is preferred, with no phase separation. Several factors distinguish these calculations, which likely have to do with the apparent contradiction in their observations. The first is the difference in the nature of the simulations. In our growth simulation, tetravalent ions are allowed to evaporate from the crystal, which facilitates phase separation. The equilibrium calculations were done in the canonical ensemble with the tetravalent ions mixed in, where it is more difficult to detect phase separation without large simulation cell sizes. Our simulations were at lower temperatures where ordered growth could be induced by tuning the chemical potential $\Delta\mu$ (adsorption rate). At these temperatures the system is essentially in the ground state, as Figure 4.1 shows. Incorporation of tetravalent ions could be induced at larger $\Delta\mu$, which is expected as adsorption dominates evaporation, but in this case random growth occurs. Secondly, since our $[111]_{1:1}$ structure is an artificial model of *random mixing* of -2 , $+1$, and neutral

charges in one layer and perfectly ordered +1 in another, its energy must be higher than the actual 1:1 structure achieved in the equilibrium simulations. This means that the actual cross-over of the random-mixing $[111]_{1:1}$ structure will occur at lower temperatures. Indeed, the $k_B T \sim 0.25$ equilibrium calculations show $[111]_{1:1}$ ordering for concentrations x greater than about 0.05. Thus the absence of phase separation in the equilibrium calculations might be due to a lower free-energy than our estimate in Fig. 4.19 from the artificial random-site structure. Our results combined with the equilibrium calculations therefore suggest the following picture of the equilibrium state of the ionic model. In the ground state phase-separation takes place for $x > 0$. Beyond some x -dependent critical temperature tetravalent ions are incorporated, most likely in a structure that favors 1:1 order.

To determine if the new phase (phase-separation) at low temperatures that we have found is realistic for these alloys, the ionic model must be improved. One possibility is first-principles based effective Hamiltonians H_{eff} , which have shown great promise in describing ferroelectrics and simple solid-solutions [29]. Like the Ising model these H_{eff} project out what are considered to be the most important ionic degrees of freedom. In addition to the long-range Coulomb interaction, short-range interactions are also included. The H_{eff} parameters are fitted to the results of a set of first-principles density-functional calculations, so there is effectively no experimental input (except sometimes the average crystal volume). The simplified form of H_{eff} for ferroelectrics and ferroelectric alloys has permitted simulations of equilibrium properties on thousands of atoms as a function of temperature and applied external electric field. A main difficulty in applying these in a growth simulation is computational cost, which has typically required fixed distributions of B-site ions even in equilibrium simulations of solid-solutions. In our kinetic Monte Carlo model, another possibly important factor that is not included is surface diffusion. Coupled with the solid-on-solid restriction, the simulation is severely limited in its ability to “heal” disorder, and these approximations may have contributed to low ordered

growth rates and raised the critical temperature for phase separation. Removal of these restrictions would improve the model and increase its applicability.

5.2 Summary

In the part of the thesis, the growth of the technologically important BMN type perovskite alloys was studied by kinetic Monte Carlo using an ionic model. An enhanced KMC algorithm was formulated to treat long-range Coulomb interactions efficiently. We found that this minimal paradigm was capable of describing ordering features of the growth of pure BMN and PMN type single crystals. The largest growth rates were observed along the $[\bar{1}\bar{1}1]$ direction, but best ordered growth rates are substantially less than those of rocksalt. Highly ordered growth was possible, but required very low temperatures and a delicate balance with the chemical potential. For mixed systems such as BMN-BZ, we found that the $T = 0$ ground state of the model was one in which tetravalent ions phase separate from a 1:2 ordered pure system. As a result, little incorporation of tetravalent ions occurs in the growth process at low temperatures. At higher temperatures, tetravalent ions can be incorporated, but the resulting crystals show no chemical ordering. The tendency of the purely ionic model to favor phase separation was further studied using free energy calculations determined from $T = 0$ total energy calculations and including a mixing entropy. This indicated that, if diffusive mechanisms were included, chemical orderings consistent with those found in equilibrium studies could develop at the higher temperatures characteristic of realistic alloy synthesis.

CHAPTER 6

Phase-free AFQMC Study of Molecular Systems

Modern theoretical studies of electronic structure often rely on solving the Schrödinger equation of many-body systems. The calculations are, in nature, first-principle and can be carried out without knowledge from experiments or any external parameters. The difficulties of solving the Schrödinger equation arise from the interactions of electrons with each other and to the nucleus. The problem can be simplified by the adiabatic approximation, which treats the many-electron system while freezing the motion of the nuclei. But even this problem is immensely complicated and often cannot be solved directly without approximations. Traditional approximations such as Hartree-Fock (HF) and Density Functional Theory (DFT) have been applied to many problems with great success. Here, the many-body interactions are replaced by single particles interacting with the mean-field generated by other particles. The interacting many-body problem is thus reduced to an independent-particle problem. These methods have seen tremendous success, and are the standard approach in electronic structure. However, they have well known limitations in materials with significant electron-electron correlations.

A more accurate approach is the quantum Monte Carlo (QMC) method which has been shown to be among the most effective methods for many-electron problems. In QMC, electron-electron interactions are in principle treated without any approximations. Unlike explicit correlated methods such as exact diagonalization or configuration interaction (CI), QMC computational times have power law scaling [30]. QMC has been successfully applied to calculate the ground and excited states in atoms and small molecules [31, 32, 33, 34] as well as the study of large atomic clusters [35].

In the past decade, QMC has shown much promise in the calculations of real solid or system containing large number of electrons. Part of the reason for this progress is the availability of growing computing power. The main reason has been the increasing development of QMC methodology: the implementation of pseudopotentials, better trial wavefunctions, etc. Recently, new QMC method for electronic structure has been developed in our group which shows promising characteristics for improving and expanding the capabilities of QMC. The goal of the present study is to further test this new method, and study its various characteristics. In this chapter, we first give an overview of some of the mean-field methods, which we will use as a starting point in our QMC. We then give a brief introduction of the QMC method before discussing the new auxiliary-field quantum Monte Carlo method in the next chapter.

6.1 Many-Electron Problems

The many-electron problem refers to the difficulties of obtaining the exact solution of the Schrödinger equation in which strong interaction of electrons is present. When the system involves more than two particles, the problem becomes complicated. The most common approach is to apply the Born-Oppenheimer approximation [36] which assumes the separation of nuclear and electron motion. The approximation is based on the idea that nuclear mass is so much larger than electron mass that the electron motion can basically

be decoupled from the nuclei. That is, the electrons respond instantaneously to the motion of the nuclei, and are in the ground state with fixed configurations of the nuclei. With this assumption, the full Schrödinger equation for many-body problems containing separate kinetic energy and interaction energy of electrons and nuclei can be expressed as:

$$\left[-\frac{\hbar^2}{2m_e} \sum_i \nabla_i^2 + \sum_{i,I} \frac{Ze^2}{|r_i - R_I|} + \frac{1}{2} \sum_{i \neq j} \frac{e^2}{|r_i - r_j|} \right] \psi(r) = \epsilon \Psi(r). \quad (6.1)$$

The first sum contains the kinetic energy of electrons; the second sum is the potential energy of the attractions between the electrons and the fixed nucleus of charge Z ; the last sum is the potential energy of the inter-electronic repulsion. The index i and j run over the number of electrons $i = 1, 2, \dots, N$. The index I demonstrates the nuclei R_I given the position (fixed) of the I^{th} nucleus. The kinetic energy are neglected in the Hamiltonian. The interaction energy between nuclei are also left out because it is a constant and does not contribute to the description of the electron motions. Even this form of Schrödinger equation is still too complex to solve directly, because we can not separate the Schrödinger equation due to the electron-electron repulsion term, $e^2/|r_i - r_j|$. There are numerous methods that aim to explain the physical properties of material through this equation. The one-electron method (or the mean-field method) which is approximate, is one of the successful approaches. In this method, electrons are considered separately. Each single electron interacts with an external potential and with a mean-field generated by all other electrons. The most common methods include the Hartree-Fock (HF) and Density Functional Theory (DFT) under a local-density approximation (LDA).

6.1.1 Hartree-Fock approach

The Hartree-Fock theory [37] is basically a correction to the Hartree approach [38] which approximates the potential through the interaction of each electrons to all other. Even though the Hartree technique successfully implements the mean-field idea to the electronic structure calculations, the absence of exchange or correlation between electrons

generally gives inaccurate results. The Hartree-Fock theory is more effective than the Hartree method. In practice, the wavefunction is written in the form of a single Slater determinant of N spin orbitals which is antisymmetric with respect to an interchange of any two electron positions as required by the Pauli exclusion principle. In Hartree-Fock theory the single electron Schrödinger equation for the i^{th} orbital can be expressed as

$$\left(-\frac{\hbar^2}{2m}\nabla^2 + V_{\text{ion}}(r)\right)\psi_i(r) + \sum_j \int \frac{dr' |\psi_j(r')|^2}{|r-r'|} \psi_i(r) - \sum_j \delta_{\sigma_i\sigma_j} \int dr' \frac{\psi_j^\dagger(r')\psi_i(r')}{|r-r'|} \psi_j(r) = \epsilon_i \psi_i(r), \quad (6.2)$$

where the sum j runs over all occupied states. The first three terms on the left hand side are common to the Schrödinger equation of the Hartree method. The third term or the Hartree term, in particular, is simply electrostatic potential arising from the charge distribution of electrons. When Pauli principle is included, the fourth term is added in order to cancel out the self-interaction contribution from the third term. This extra term is called the exchange term which gives a lower ground state total energy for the system when comparing to that of the Hartree calculations.

With this form of Schrödinger equation, the potential depends on single particle wavefunctions, the equation must be solved self-consistently. Since the method includes the exchange interaction between electrons, it is rather computationally demanding and more suitable for studying smaller systems. By definition, the HF method neglects correlations between electrons. Although qualitatively correct in many materials and compounds, Hartree-Fock theory is often inadequate for predicting quantitative results. In our study, the HF method is used for providing qualitative predictions or as the starting guess for the quantum Monte Carlo (See Chapter 8).

6.1.2 Density Functional Theory

Density function theory (DFT) is in principle an exact theory [39]. In practice, it is implemented approximately under the local density approximation (LDA) or one of the gradient-corrected exchange-correlation functionals [40, 41]. In LDA, the fully interacting many-body Hamiltonian is replaced by the self-consistent single-particle equations called the Kohn-Sham equation [42]:

$$\left[-\frac{\hbar^2}{2m} \nabla_{r_i}^2 + V_{eff}(r, [n(r)]) \right] \psi_i(r) = \epsilon_i \psi_i(r) \quad (6.3)$$

where $n(r)$ is the density and the effective one-electron potential consists of three contributions: external potential, Hartree potential and the exchange-correlation potential. The Kohn-Sham equations can be viewed as the equation which minimizes the energy functional of the non-interacting electrons moving in the effective potential V_{eff} . Frequently in LDA the approximate exchange-correlation energy, V_{eff} is obtained from the energy of an electron in an homogeneous electron gas at the same density [43].

Density Functional theory within the LDA has been a remarkable success in performing electronic structure calculations. It is often significantly more accurate than the Hartree-Fock. However, this method is not ideal when systems with strong electron correlations are of interest.

6.2 Quantum Monte Carlo

Both HF and LDA have difficulties to treat electron correlation adequately. The Hartree-Fock method ignores the electron correlations completely. The LDA approximates the correlation in the form of the functional but often leads to incorrect results for highly correlated problems. These methods reduce the many-body Schrödinger equation to one-electron equations. In contrast, the quantum Monte Carlo (QMC) [44] method aims to solve the many-body Schrödinger equation directly.

In this thesis, we focus on the ground state properties of real materials. In particular, we compute the dissociation and ionization energies of many atoms and molecules within the framework of the auxiliary-field quantum Monte Carlo (AFQMC) method under the phase-free Slater determinant random walk formalism [45]. The standard AFQMC [46, 47, 48, 49, 45] is a stochastic method which has been widely used to study fermion systems extensively in many areas of research, including condensed-matter problems and nuclear shell-model calculations [50, 51]. It experiences a sign problem for “simple” forms of interactions and a phase problem [45] for realistic two-body interactions. Our method builds upon the constraint path Monte Carlo (CPMC) and the diffusion Monte Carlo (DMC). Just as in DMC, we apply an imaginary-time evolution operator \mathcal{P} , often in the form of $\mathcal{P} = e^{-\Delta\tau\mathcal{H}}$, successively on a trial wave function, $|\Psi_T\rangle$ which has a nonzero overlap with the real ground state. After a large number of iterations, the ground state wave function $|\Psi_G\rangle$ is obtained— $\lim_{n\rightarrow\infty}(e^{-\Delta\tau\mathcal{H}})^n|\Psi_T\rangle \rightarrow |\Psi_G\rangle$. The Hamiltonian is written in the form of the one-body and two-body interactions in second quantization which automatically accounts for the symmetry of system. In practice, the one-body operator is easily managed in the space of single Slater determinant but the two-body contribution introduces complications to the projection. To bypass this difficulty, the two-body propagator is transformed into a multi-dimensional integral of one-body propagators by using the Hubbard-Stratonovich transformation [52, 53]. This transforms the problem of interacting particles into the problem of non-interacting particles in fluctuating external auxiliary field. By doing this, we have introduced the complex field σ in which the integral can be evaluated by means of the Monte Carlo sampling of σ .

The AFQMC technique is formulated in a space spanned by any one-particle basis. In practice, any basis used in independent-particle methods together with all its machinery, can be applied. This feature is beneficial to AFQMC because it allows one to take full advantage of the well-established techniques like LDA or HF. In our calculations, we use a single Slater determinant as a trial wave function and planewaves as the one-particle

basis. Using planewaves is appealing for several reasons: it is unbiased, suitable for periodic systems and greatly simplifies the mathematics involved. However, it is inefficient for describing atomic core states because of the requirement of an intractable number of planewaves. To reduce the number of planewaves, we use a norm-conserving Kleinman-Bylander pseudopotential [54] in our calculations. It reduces the number of electrons (core orbitals are removed) and decreases the energy scales, both of which reduce the calculation time substantially.

A long-standing problem in standard AFQMC has been the presence of large statistical fluctuations caused by a sign or phase problem, similar to the “sign problem” in the standard DMC in electronic structure [54]. Generally, the fermion matrix operator may be negative or complex. The sign or phase of these fermions wavefunctions can lead to dramatic cancellations in the statistical samples, which result in large statistical errors. This problem long hindered the application of auxiliary-field-based QMC methods in realistic systems. Zhang and Krakauer [45] have alleviated this issue by proposing an approximate phase-free method. This method built upon the constrained path Monte Carlo method, and applies an importance sampling dependent on trial wave functions $|\Psi_T\rangle$. In this formalism, the statistical random walkers are guided to be sampled in the region governing large contribution of ground state as well as the least phase fluctuation. The resulting ground state energy is then expressed in term of the local energy independent of any phase factor.

CHAPTER 7

Auxiliary-Field Quantum Monte Carlo

In Chapter 6, we have discussed several well-established methods which apply to many-electron problems and outlined the basic idea of the quantum Monte Carlo formalism. This chapter aims to provide the theory and algorithm underlying the new auxiliary-field quantum Monte Carlo method developed in our group [45]. The overall objective is to solve the many-body Schrödinger equation which describes the electrons in the atomic or bulk materials. The material properties are completely determined by the Schrödinger equation. QMC methods introduce an artificial “randomness” on the electron motion, which is consistent with the underlying Schrödinger equation. This makes it possible to build up statistical estimates of the ground state properties of the system, which allows solution of the many-dimensional partial differential Schrödinger equation without requiring growing exponentially computer time with system size.

The type of the QMC simulation used in this thesis is the new phaseless auxiliary-field quantum Monte Carlo method which is a ground state method. In principle the method generates exact solutions of the many-electrons Schrödinger equation and the only errors present, in practice, are due to the approximations to control the infamous phase problem. Unlike DMC which yields upper bounds of the true ground state, our

method is not variational. The remainder of this chapter is organized as follows: in Section 7.1, we highlight the fundamental idea of the imaginary time propagation which is the kernel of the AFQMC method. Starting from an imaginary time Schrödinger equation, we show a given trial state can be iteratively projected to lead to the ground state. In the next two sections, we write out the formalism on a single Slater determinant which is a key ingredient of our method, and the many-body Hamiltonian in second-quantized form. We discuss the algorithm of auxiliary-field quantum Monte Carlo in section 7.4. The next section devotes to the discussion of the phase problem that arises in the AFQMC. Conceptually similar to real-space diffusion Monte Carlo (DMC), the AFQMC phase problem differs considerably from the analogous minus-sign problem. We present the phaseless formalism [45] which allows us to control the phase problem. The last portion of this chapter is devoted to the detail of implementation in the realistic systems. The expressions of the one-body and two-body Hamiltonian in planewave basis are given explicitly and the statistical technique used to compute the expectation value of observables is described.

7.1 Imaginary Time Propagator

The AFQMC is a projector based method where the ground state is projected out by an imaginary time propagator. The central idea of the propagator is based on the time-dependent Schrödinger equation:

$$i\hbar \frac{\partial |\Psi\rangle}{\partial t} = \mathcal{H}|\Psi\rangle. \quad (7.1)$$

By allowing $\tau = it$, the Schrödinger equation can be expressed as

$$\hbar \frac{\partial |\Psi\rangle}{\partial \tau} = -\mathcal{H}|\Psi\rangle. \quad (7.2)$$

Following the basic derivation of the time-evolution Schrödinger equation [55], the propagated state can be expanded in terms of the eigenvectors $|\phi_1\rangle, |\phi_2\rangle, \dots, |\phi_n\rangle$ with the corresponding eigenvalues $\epsilon_1, \epsilon_2, \dots, \epsilon_n$ as

$$|\Psi(\tau)\rangle = \sum_{i=1}^n c_i(\tau) |\phi_i\rangle, \quad (7.3)$$

where the prefactor $c_i(\tau)$ is the time-dependent overlap function $\langle\Psi(\tau)|\phi_i\rangle$. For any propagator in the form of $e^{-\Delta\tau\mathcal{H}}$, the solution Eq. (7.1) suggests that

$$\begin{aligned} |\Psi(\Delta\tau)\rangle &= e^{-\Delta\tau\mathcal{H}}|\Psi(0)\rangle \\ &= \sum_i c_i(0) e^{-\Delta\tau\epsilon_i} |\phi_i\rangle. \end{aligned} \quad (7.4)$$

If we apply the propagator $e^{-\Delta\tau\mathcal{H}}$ to the vector $|\Psi\rangle$ for n times, the new vector is written as

$$|\Psi(n\Delta\tau)\rangle = c_0(0)e^{-n\Delta\tau\epsilon_0}|\phi_0\rangle + c_1(0)e^{-n\Delta\tau\epsilon_1}|\phi_1\rangle + c_2(0)e^{-n\Delta\tau\epsilon_2}|\phi_2\rangle + \dots \quad (7.5)$$

Assuming that the summation is ordered such that the eigenenergies ϵ_i ascend with the index i , all states with higher energy than the ground state energy, ϵ_0 , decay away faster for the limit of $n \rightarrow \infty$. Thus the ground state can be projected from any known trial state as long as the non-orthogonality condition is satisfied:

$$\lim_{n \rightarrow \infty} e^{-n\Delta\tau\mathcal{H}} |\Psi_T\rangle \rightarrow |\Psi_G\rangle. \quad (7.6)$$

This projection has been applied extensively and is the basis for most ground-state techniques.

7.2 Slater Determinant Wavefunctions

The most commonly used form for an anti-symmetric wavefunction is a single Slater determinant or a linear combination of Slater determinants. A Slater determinant provides a simple representation which maintains the fermion symmetry (or anti-symmetry)

characteristics. Below we briefly outline some basic formalism [56, 57] to facilitate our discussion of the AFQMC method. Given the nature of the method which can be formulated in a Hilbert-space spanned by any one-particle basis, there exists infinite choices of wavefunctions. In principle, a wavefunction $\Psi(x)$ depends on the electronic spatial and spin coordinates which can be derived by simply expanding $|\Psi\rangle$ in terms of a set of one-electrons orbitals $|\chi_i\rangle$. States and operators in the AFQMC are formulated in terms of the second quantization representation, in which basis states are defined with respect to their occupation number. The single particle orbitals can be written in terms of the the fundamental fermion creation and annihilation operators, $c_{i\sigma}^\dagger$ and $c_{i\sigma}$ which obey the anti-commutation relations:

$$\{c_{i\sigma}^\dagger, c_{j\sigma'}^\dagger\} = 0, \quad \{c_{i\sigma}, c_{j\sigma'}\} = 0, \quad \{c_{i\sigma}, c_{j\sigma'}^\dagger\} = \delta_{ij}\delta_{\sigma\sigma'}. \quad (7.7)$$

For a system of N particles, the n^{th} single particle orbital is given as;

$$\sum_i \varphi_{i,n} |\chi_i\rangle = \sum_i c_i^\dagger \varphi_{i,n} |0\rangle = \hat{\varphi}_n^\dagger |0\rangle, \quad (7.8)$$

which can also be written as an M -dimensional vector:

$$\Phi_n = \begin{pmatrix} \varphi_{1,n} \\ \varphi_{2,n} \\ \vdots \\ \varphi_{M,n} \end{pmatrix}.$$

The creation operator, $\hat{\varphi}_n^\dagger$, produces an electron in the n^{th} single particle orbital and is expressed as;

$$\hat{\varphi}_m^\dagger \equiv \sum_i c_i^\dagger \varphi_{i,m}. \quad (7.9)$$

For N identical fermions, the single-particle orbitals, $\varphi_{i,m}$, give rise to the many-body

state in form of the $M \times N$ matrix:

$$\Phi = \begin{pmatrix} \varphi_{1,1} & \varphi_{1,2} & \cdots & \varphi_{1,N} \\ \varphi_{2,1} & \varphi_{2,2} & \cdots & \varphi_{2,N} \\ \vdots & \vdots & & \vdots \\ \varphi_{M,1} & \varphi_{M,2} & \cdots & \varphi_{M,N} \end{pmatrix}$$

where M is again the size of basis function. The row of the matrix Φ is labeled for the electrons, the column is labeled for spatial-spin orbital. In other words, the i_{th} column of the matrix Φ describes the single-particle orbital of the i_{th} electron through its M -dimensional vector. The many-body wavefunction is given by:

$$|\phi\rangle \equiv \hat{\varphi}_1^\dagger \hat{\varphi}_2^\dagger \cdots \hat{\varphi}_N^\dagger |0\rangle \quad (7.10)$$

For the system containing N_\uparrow of the “up” and N_\downarrow of the “down” electrons where $N = N_\uparrow + N_\downarrow$, the Slater determinant is generalized as the product of the up-spin and down-spin orbitals:

$$|\phi\rangle = \underbrace{|\phi_\uparrow\rangle}_{M \times N_\uparrow} \otimes \underbrace{|\phi_\downarrow\rangle}_{M \times N_\downarrow} \quad (7.11)$$

In our QMC, each random walker is a single Slater determinant, whose orbitals coefficients $\{\phi_{i,m}\}$ evolve stochastically. Our trial wavefunctions are single Slater determinants: $|\Psi_T\rangle = |\phi\rangle$. The one-particle orbitals in $|\Psi_T\rangle$ are obtained from the independent one-particle methods i.e. DFT or HF. Either “restricted” or “unrestricted” trial wavefunctions are used. By restricted determinant, we mean that the up-spin and down-spin share the same orbitals, which is specified by the determinant of the majority spin electrons. In contrast to the restricted calculations, to write the determinant in an unrestricted manner, the two spin components are allowed to have different orbitals.

7.3 Many-body Hamiltonian

We express the Hamiltonian for a many-fermion system with two-body interaction in the general terms of the one- and two-particle operators:

$$\begin{aligned}\mathcal{H} &= \mathcal{H}_1 + \mathcal{H}_2 \\ &= \sum_{i,j}^M \mathcal{T}_{ij} c_i^\dagger c_j + \frac{1}{2} \sum_{i,j,k,l}^M \mathcal{V}_{ijkl} c_i^\dagger c_j^\dagger c_k c_l,\end{aligned}\quad (7.12)$$

where c_i^\dagger, c_i are the corresponding creation and annihilation operators for one-particle basis $|\chi_i\rangle$ respectively; the index i, j, k, l sum over all the one-particle basis. The one-body \mathcal{T}_{ij} and two-body \mathcal{V}_{ij} matrix elements are known. Since the one-particle Hamiltonian \mathcal{H}_1 is defined on a single-particle state described by the coordinate r_a , the matrix element \mathcal{T}_{ij} is simply

$$\mathcal{T}_{ij} = \int dr_a \chi_i^*(r_a) \mathcal{T}(r) \chi_j(r_a), \quad (7.13)$$

where $\mathcal{T}(r)$ is a one-particle operator, say the kinetic energy operator, $-\frac{\hbar^2}{2m} \nabla_{r_a}^2$. Similarly, the matrix element \mathcal{V}_{ijkl} represents the Coulomb interaction of two particles and is derived from;

$$\mathcal{V}_{ijkl} = \int dr_a dr_b \chi_i^*(r_a) \chi_j^*(r_b) \mathcal{V}(r) \chi_k(r_a) \chi_l(r_b), \quad (7.14)$$

where r_a and r_b give the coordinates of the two particles and $V(r) = V(r_a - r_b)$.

7.4 Auxiliary-Field Formalism

With the well-defined many-particles Hamiltonian, the ground-state projection is performed by applying the propagator (Eq. 7.6) to a trial state for n successive iterations. Since \mathcal{H}_1 and \mathcal{H}_2 in general do not commute, an approximation needs to be introduced. For a small imaginary time steps $\Delta\tau$, the propagator can be accurately separated into the

one-particle and two-particle constituents by applying the Trotter-Suzuki decomposition [58, 59]. The projection operator becomes

$$e^{-\Delta\tau\mathcal{H}} = e^{-\Delta\tau\frac{\mathcal{H}_1}{2}} e^{-\Delta\tau\mathcal{H}_2} e^{-\Delta\tau\frac{\mathcal{H}_1}{2}} + \mathcal{O}(\Delta\tau^3) \quad (7.15)$$

With this approximation, we have introduced a so-called Trotter error to the calculations, which in principle can be easily controlled. In practice, we identify the error by performing an array of calculations with several $\Delta\tau$ and then extrapolating to determine the $\Delta\tau \rightarrow 0$ limit. In cases without an explicit extrapolation, we carry out calculations with a very small value of $\Delta\tau$ whose corresponding Trotter error is smaller than the statistical error.

This projection is evaluated in the space of single Slater determinants, in which planewaves are used as the one-particle basis. Following the same procedure as the iterative Monte Carlo technique, the initial wavefunction is iterated into the projected functions as

$$|\Psi(\tau + \Delta\tau)\rangle = e^{-\Delta\tau\frac{\mathcal{H}_1}{2}} e^{-\Delta\tau\mathcal{H}_2} e^{-\Delta\tau\frac{\mathcal{H}_1}{2}} |\Psi(\tau)\rangle. \quad (7.16)$$

In applying the operators to a Slater determinant, the exponential form of the one-body operator, $e^{-\Delta\tau\mathcal{H}_1}$, is guaranteed to have the result of another Slater determinant (detailed derivation is given in ref. [48] and ref. [60]). The projector containing the two-body operator, on the other hand, is more complicated; propagating this operator on a Slater determinant does not give another Slater determinant. Nevertheless, if the two-body Hamiltonian is manipulated into a linear form of the one-body operator, the problem once again can be treated as the iteration of single Slater determinants. We rewrite \mathcal{H}_2 as the following [45, 61]:

$$\mathcal{H}_2 = -\frac{1}{2} \sum_{\alpha} \lambda_{\alpha} \hat{v}_{\alpha}^2, \quad (7.17)$$

where the prefactor λ_{α} is a real number, defined by the matrix element \mathcal{V}_{ijkl} , and \hat{v}_{α} is

a one-body operator. We then introduce the Hubbard-Stratonovich(HS) transformation [52, 53], transforming the exponential of the quadratic one-body operator into a linear combination of the one-body exponential. The resulting multi-dimensional integration is

$$e^{-\Delta\tau\hat{H}_2} = \prod_{\alpha} \left(\frac{1}{\sqrt{2\pi}} \int_{-\infty}^{\infty} e^{-\frac{1}{2}\sigma_{\alpha}^2} e^{\sqrt{\Delta\tau}\sigma_{\alpha}\sqrt{\lambda_{\alpha}}\hat{v}} d\sigma_{\alpha} \right). \quad (7.18)$$

Here, the variable σ_{α} is a set of Hubbard-Stratonovich auxiliary fields. The constant λ_{α} can be either positive or negative, hence the one-body propagator can be either real or imaginary. It is important to note that the auxiliary fields which appear in the Hubbard-Stratonovich transformation are solely mathematical constructions. Their purpose is to provide a convenient integral representation of the two-body Hamiltonian. They map the system of interacting particles into the system of non-interacting particles in complex fields σ_{α} . The particle interactions will be recovered at the end when we sum up all the auxiliary fields.

Defining the vector representations of $\{\sigma_{\alpha}\}$ and $\{\sqrt{\lambda_{\alpha}}\hat{v}_{\alpha}\}$ as $\sigma \equiv \{\sigma_1, \sigma_2, \dots\}$ and $\hat{v} = \{\sqrt{\lambda_1}\hat{v}_1, \sqrt{\lambda_2}\hat{v}_2, \dots\}$ respectively. The propagator is expressed as

$$e^{-\Delta\tau\mathcal{H}} = \int P(\sigma)B(\sigma)d\sigma, \quad (7.19)$$

where

$$B(\sigma) = e^{-\frac{\Delta\tau\mathcal{H}_1}{2}} e^{\sqrt{\Delta\tau}\sigma\cdot\hat{v}} e^{-\frac{\Delta\tau\mathcal{H}_1}{2}}, \quad (7.20)$$

which contains only one-body operators in the exponent. The probability density function, $P(\sigma)$, is a multi-dimensional Gaussian function.

Defined in this manner, the propagator is now translated into a multi-dimensional integration over a finite time slice, n , and the auxiliary fields, σ_{α} . Instead of directly evaluating such an integral, we apply the Monte Carlo sampling through a random walk

in which an initial state $|\phi\rangle$ is propagated by the operator $B(\sigma)$ and obtain the new state as

$$|\phi'\rangle = B(\sigma)|\phi\rangle, \quad (7.21)$$

where σ is sampling from the probability distribution $P(\sigma)$. Conceptually, we can think of the random walkers as representing the many-body ground state by:

$$|\Psi_G\rangle = \sum_{\phi'} |\phi'\rangle, \quad (7.22)$$

Importance sampling is introduced to improve the efficiency of the random walks in Slater determinant space [45, 61].

7.5 Phase Problem

It is well-known that QMC computations involving fermions often experience a noise called *fermion sign problem*. The origin of the problem arises from the fundamental symmetry of the fermion ground states. Because a wavefunction when multiplied by -1 is indistinguishable from the original wavefunction, the coexistence of the positive and the negative states increases the fluctuations of the random walk projections. The sign problem is common to many Monte Carlo methods. In the standard DMC algorithm, for example, a fixed-node approximation [62] is applied in most realistic applications. We encounter a similar problem termed the *phase problem*, which can be identified by considering the parameter λ_α that appeared in Eq. 7.18. Normally, λ_α can be either positive or negative and as a result, the one-body operator \hat{v} in Eq. 7.20 is complex. The walkers now have an infinite number of symmetry, e.g. $e^{i\theta}|\phi\rangle$ for $\theta \in [0, 2\pi]$. The Monte Carlo sampling lacks the ability to distinguish these different phases. The degree of randomness exponentially increases as the projection time, β , increases and causes the fluctuation to

dominate the random walk. To improve the ability of the method to treat the phase problem, a phasefree scheme was developed [45, 61]. The principle idea consists of two parts, which are described briefly below in Section 7.5.1 and 7.5.2 respectively.

7.5.1 Auxiliary Field Force Bias

The first ingredient in the new method is an importance sampling transformation. It is possible to describe it. We will adopt one involving a shift in the integration [63] in Eq. 7.18. Without altering the potential projection, the Hubbard-Stratonovich transformation of $e^{-\Delta\tau\mathcal{H}_2}$ can be rewritten with an arbitrary shift to the auxiliary fields, as follows:

$$\begin{aligned} e^{-\Delta\tau\mathcal{H}_2} &= \frac{1}{\sqrt{2\pi}} \int_{-\infty}^{\infty} e^{-\frac{1}{2}(\sigma-\bar{\sigma})^2} e^{\sqrt{\Delta\tau}(\sigma-\bar{\sigma})\sqrt{\lambda\hat{v}}} d\sigma \\ &= \frac{1}{\sqrt{2\pi}} \int_{-\infty}^{\infty} e^{-\frac{1}{2}\sigma^2} e^{\sigma\bar{\sigma}-\frac{\bar{\sigma}\cdot\bar{\sigma}}{2}} e^{\sqrt{\Delta\tau}(\sigma-\bar{\sigma})\sqrt{\lambda\hat{v}}} d\sigma. \end{aligned} \quad (7.23)$$

Analogous to Eq. 7.19, the new propagator becomes;

$$\widetilde{e^{-\Delta\tau\mathcal{H}_2}} = \int e^{\sigma\bar{\sigma}-\frac{\bar{\sigma}\cdot\bar{\sigma}}{2}} P(\sigma) B(\sigma - \bar{\sigma}) d\sigma, \quad (7.24)$$

where $\bar{\sigma}$ is a multidimensional vector (like σ) to be determined. The goal of $\bar{\sigma}$, which we will call force bias in analogy with DMC, is to avoid sampling points uniformly in phase spaces. To accomplish this we direct the sampling process to the more ‘‘important’’ regions by using the importance sampling technique. In this formulation, points will be sampled from a non-uniform distribution which utilizes the trial wavefunctions, which contain our best a priori. The important function is expressed in term of the overlap $\langle\Psi_T|\phi\rangle$. We can think of the importance sampled walker as

$$|\phi\rangle \rightarrow \frac{|\phi\rangle}{\langle\Psi_T|\phi\rangle}. \quad (7.25)$$

The auxiliary fields σ can be evaluated by selecting points from the probability density function:

$$\widetilde{P}(\sigma) = \frac{\langle \psi_T | \phi' \rangle}{\langle \psi_T | \phi \rangle} P(\sigma) \quad (7.26)$$

The new propagator is

$$\begin{aligned} \widetilde{e^{-\Delta\tau\mathcal{H}}} &= \int \frac{\langle \Psi_T | \phi' \rangle}{\langle \Psi_T | \phi \rangle} P(\sigma) e^{\sigma\bar{\sigma} - \frac{\bar{\sigma}\cdot\bar{\sigma}}{2}} B(\sigma - \bar{\sigma}) d\sigma \\ &= \int P(\sigma) W(\sigma, \phi) B(\sigma - \bar{\sigma}) d\sigma \end{aligned} \quad (7.27)$$

where

$$W(\sigma, \phi) \equiv \frac{\langle \Psi_T | B(\sigma - \bar{\sigma}) | \phi \rangle}{\langle \Psi_T | \phi \rangle} e^{\sigma\bar{\sigma} - \frac{\bar{\sigma}\cdot\bar{\sigma}}{2}}. \quad (7.28)$$

The weight factor $W(\sigma, \phi)$ plays an important role in controlling the collection of walkers. In the beginning of the stochastic evolution, the configuration of random walkers (often called population of walkers) is generated straightforwardly from a set of trial wavefunction $|\Psi_T\rangle$. The ground-state propagation proceeds by sampling an auxiliary field σ from the probability density $P(\sigma)$. Then the walker is propagated to a new state by having $B(\sigma - \bar{\sigma})$ operate on the original state;

$$|\phi'\rangle \leftarrow B(\sigma - \bar{\sigma})|\phi\rangle \quad (7.29)$$

It is important to comment here that from this point on the walker $|\phi\rangle$ is an importance-sampled walker. At each iteration, the weight of each walker is updated according to

$$w'_i = W(\sigma, \phi) \times w_i. \quad (7.30)$$

This weight factor controls the distribution of the walkers. At the end of each imaginary time step, the weight of each walker is examined so that they are within some pre-set bounds. Walkers with low weight are removed with some probability, while large weight

walkers are multiplied and are assigned smaller weight. This is referred to as population control [60]. Even though this procedure balances the weights of the walker population, occasionally the total number of walkers is either too high or too low, due to statistical fluctuations. We implement an additional population control procedure which periodically adjusts the overall walker population. The walkers will be duplicated when the population is low and will be eliminated when the population is high. This ensures that throughout the calculation, the number of walkers falls within the appropriate bound after the equilibrium ground state is reached. It can be easily seen that $W(\sigma, \phi)$ depends on both initial and final states, therefore the propagated walkers with large overlap with the trial states tend to survive and those with small overlap are likely to be eliminated. This justifies that the final walkers will share the most resemblance with the ground state while maintaining weights with the least fluctuations. At equilibrium, we obtain the following (schematically) representation of the ground state:

$$|\Phi_G\rangle \equiv \sum_{\phi'} w_{\phi'} \frac{|\phi'\rangle}{\langle \Phi_T | \phi' \rangle}. \quad (7.31)$$

The ground state energy and other quantities can then be calculated from the distribution of walkers.

The shift $\bar{\sigma}$ is an arbitrary constant. Any choice of $\bar{\sigma}$ would yield the faithful evolution of the imaginary-time propagation, and the formalism, which was obtained via a similarity transformation is exact. We choose the value of $\bar{\sigma}$ for which the fluctuation of σ -dependent weight factor is at the minimum. To determine this optimal value of $\bar{\sigma}$, we follow the customary minimization procedure by taking the derivative of the weight function $W(\sigma, \phi)$ with respect to σ , setting the derivation to zero and deriving $\bar{\sigma}$ at $\sigma = 0$:

$$\left. \frac{\partial W(\sigma, \phi)}{\partial \sigma} = \frac{\partial}{\partial \sigma} \left[\frac{\langle \Psi_T | B(\sigma - \bar{\sigma}) | \phi \rangle}{\langle \Psi_T | \phi \rangle} e^{\sigma \bar{\sigma} - \frac{\bar{\sigma} \cdot \bar{\sigma}}{2}} \right] \right|_{\sigma=0} = 0. \quad (7.32)$$

The result is expanded in terms of $\Delta\tau$. All the higher order terms vanish. The

remaining leading terms containing $\sqrt{\Delta\tau}$ give

$$\bar{\sigma} = -\sqrt{\Delta\tau} \frac{\langle \Psi_T | \hat{v} | \phi \rangle}{\langle \Psi_T | \phi \rangle}. \quad (7.33)$$

The weight factor $W(\sigma, \phi)$ can now be further manipulated by substituting back the $\bar{\sigma}$ derived in Eq. 7.33 into the expression in Eq. 7.28. We can expand $W(\sigma, \phi)$ in terms of $\Delta\tau$ and ignore some terms of order $\Delta\tau$ or higher.

We then obtain $W(\sigma, \phi)$ in the following simplified form

$$W(\sigma, \phi) \doteq e^{-\Delta\tau \frac{\langle \Psi_T | \hat{H} | \phi \rangle}{\langle \Psi_T | \phi \rangle}} \equiv e^{-\Delta\tau E_L(\phi)}. \quad (7.34)$$

The local energy, E_L which is calculated from the mixed estimator of the trial state and a walker at position $|\phi_i\rangle$ is introduced. E_L tends to a real constant in the limit of exact $|\Psi_T\rangle$. As a result, the weight $W(\alpha, \phi)$ of each walker is real and is independent of any overall phase factor. In a realistic system, however, the trial wave function is not exact. It is necessary to substitute the real part of the local energy rather than the complex one in Eq. 7.34. The ground state energy can be rearranged into the form of the local energy as follows:

$$E_G = \frac{\langle \Psi_T | \hat{H} | \Phi_G \rangle}{\langle \Psi_T | \Phi_G \rangle} \equiv \frac{\sum_{\phi'} w_{\phi'} E_L(\phi')}{\sum_{\phi'} w_{\phi'}}. \quad (7.35)$$

As shown, the ground state energy is defined by real, positive and phase independent parameters, E_L and $w_{\phi'}$.

7.5.2 Rotational Invariant Projection

In the previous section, we modified the propagator with the force bias which removes the phase-dependent factor from the random walkers. However, the phase problem still remains due to the characteristics of the walkers populating a two-dimensional plane. The walkers are *rotationally invariant* [45] in the complex plane defined by $\langle \Psi_T | \phi \rangle$ as

they undergo the random walk process. The overlap between the trial wave functions and the walkers propagates rapidly with imaginary time. As $n\Delta\tau \rightarrow \infty$, the walkers will fill the complex plane without any consideration of the origin. As a result, some walkers build up at $\langle\Psi|\phi\rangle = 0$ where the constant shift $\bar{\sigma}$ and the local energy diverge, therefore the random walk process encounters these diverging fluctuations, and the phase problem returns. In order to control this additional problem, we perform an approximation, by applying a one-dimensional projection to the weight of each walker. The projecting depends on the phase different between between the original and the new walker position. We obtain

$$w'(\sigma, \phi) \equiv w(\sigma, \phi) \times \{\min(0, \cos(\Delta\theta))\} \quad (7.36)$$

where

$$\Delta\theta = \frac{\langle\Psi_T|\phi'\rangle}{\langle\Psi_T|\phi\rangle}.$$

As a result of this projection, the density of walkers vanish at the origin and the divergence is circumvented. This step combined with Section 7.5.1 yields the desired phaseless formulation.

7.6 Implementations with a Planewave Basis

We carry out the calculations using planewave basis and supercells under periodic boundary conditions. The planewave basis, $\{\vec{k}\}$, is given by the corresponding kinetic energy cutoff, E_{cut} as

$$\frac{\hbar^2}{2m}|\mathbf{k}|^2 \leq E_{\text{cut}}. \quad (7.37)$$

In this work, the one-body Hamiltonian consists of the kinetic energy and electron-ion potential, while the two-body Hamiltonian contains the electron-electron interactions.

The Hamiltonian is:

$$\mathcal{H} = \mathcal{H}_1 + \mathcal{H}_2. \quad (7.38)$$

Within the planewave one-particle basis, terms in the one-body Hamiltonian \mathcal{H}_1 is $\mathcal{H}_1 = \mathcal{K} + \mathcal{V}_{ie}$, where terms are:

$$\begin{aligned} \hat{T} &= \frac{1}{2} \sum_{k,\sigma} k^2 c_{k,\sigma}^\dagger c_{k,\sigma} \\ \hat{V}_{i,L} &= \sum_{k \neq k',\sigma} V_L(\mathbf{k} - \mathbf{k}') c_{k,\sigma}^\dagger c_{k',\sigma} \\ \hat{V}_{i,NL} &= \sum_{k,k',\sigma} V_{NL}(\mathbf{k}, \mathbf{k}') c_{k,\sigma}^\dagger c_{k',\sigma}. \end{aligned} \quad (7.39)$$

where $\hat{V}_{i,L}$ and $\hat{V}_{i,NL}$ are local and non-local pseudopotentials respectively; $c_{k,\sigma}^\dagger$, $c_{k,\sigma}$ are creation and annihilation operators of an electron of momentum \mathbf{k} and spin σ . Reduced units are used in which $\hbar = m = 1$. The non-local pseudopotential is given in the Kleinman-Bylander form (Appendix B). Two-body Hamiltonian $\mathcal{H}_2 = \mathcal{V}_{ee}$ can be rearranged into the following form:

$$\begin{aligned} \hat{V}_{ee} &= \frac{1}{2\Omega} \sum_{kk',\sigma\sigma'} \sum_{q \neq 0} \frac{4\pi}{q^2} c_{k+q,\sigma}^\dagger c_{k'-q,\sigma'}^\dagger c_{k',\sigma'} c_{k,\sigma} \\ &= \frac{1}{2\Omega} \sum_{q \neq 0} \frac{4\pi}{q^2} \rho^\dagger(q) \rho(q) \end{aligned} \quad (7.40)$$

where $\rho(q) = \sum_{k,\sigma} c_{k+q,\sigma}^\dagger c_{k,\sigma}$ and Ω is the unit cell volume. The k and k' are the momenta within the cutoff. The ground state propagation is reduced to

$$\begin{aligned} B(\sigma) &= e^{-\Delta\tau\mathcal{H}_1/2} e^{(\sqrt{\Delta\tau}\sigma \cdot \mathbf{v})} e^{-\Delta\tau\mathcal{H}_1/2} \\ &= e^{-\Delta\tau\mathcal{H}_1/2} e^{(\sqrt{\frac{4\pi}{q^2}\Delta\tau}\sigma\rho(\mathbf{q}))} e^{-\Delta\tau\mathcal{H}_1/2} \end{aligned} \quad (7.41)$$

The number of Hubbard-Stratonovich fields depends on the q-vectors and scales linearly with the number of basis function ($\mathcal{O}(M)$). In practice, the application of the one-body propagator in $B(\sigma)$ on a single Slater determinant is efficiently achieved by iterative applications using fast Fourier transforms (FFT). The overall computational time scales like $N^2 M \ln(M)$.

7.7 Statistical Errors

We are often interested in the difference of energies of two systems rather than an absolute energy of a single system. The properties of interest are dissociation energy or ionization energy, ΔE is the difference of two energies independently computed for each system. The composite statistical error is expressed in terms of $\sigma_{\Delta E} = \sqrt{\sigma_1^2 + \sigma_2^2}$ where σ_1 and σ_2 are the statistical error associated with each energy. The statistical accuracy of the AFQMC method improves as we increase the number of iterations. However, there are other factors that must be considered i.e. the relaxation time and the serial correlations in the data. The relaxation time determines the amount of propagation needed to reach the equilibrium (ground state). We therefore exclude sufficient number of initial steps during the simulations. The autocorrelation comes from the fact that successive steps in the random walk are correlated, and must be treated with care to obtain an accurate estimate of the error bar. We suppress the correlation effects by a reblocking technique. Data are divided into M sets each of which contains n points. We then take average of each set of n points and compute global error of the grand average from the variance of these averages until the variance does not change anymore, to obtain true error bar.

CHAPTER 8

AFQMC Results

Our calculations were performed using the new phase-free AFQMC method [45] described in Chapter 7. The trial wavefunction is the starting point of our simulation and is of importance to the final accuracy of our calculations. We used trial wavefunctions in the form of single Slater determinants whose orbitals are obtained either from density functional theory (DFT) with local density approximation (LDA) or Hartree-Fock (HF) calculations. The LDA wavefunctions were generated from the ABINIT software [64], while the HF starting wavefunctions were obtained from an in-house program. As mentioned, we use planewaves as the one-particle basis, which provides many advantages including convenience and ease in controlling the convergence. In order to achieve an accurate representation of realistic systems, a large number of planewaves are often required. This number is reduced greatly by using optimized norm-conserving Kleinman-Bylander(KB) pseudopotentials [54] to effectively remove the core electrons in each atom.

8.1 Pseudopotential Construction

The OPIUM package [65] is used to construct pseudopotentials based on the norm-conserving non-local Kleinman-Bylander formalism. The method is explained in more detail in Appendix B. To achieve a good pseudopotential, the key ingredients are the transferability and the all-electron convergence errors which will be described below. All parameters are adjusted aiming to optimize these two qualities.

To construct a pseudopotential, an atomic reference electronic configuration is chosen. Then, the Kohn-Sham equations [42] are solved, which yields all-electron one-particle wavefunctions and eigenvalues. A pseudoatom core radius r_c is chosen for each angular momentum. The smaller r_c , the closer pseudopotentials mimic the all-electron properties, but smaller r_c 's will result in more singular potentials and require more planewaves. In the study of diatomic molecules, r_c should also be larger than the neighboring distance of pseudoatoms. Nodeless pseudo valence orbitals are constructed, which are identical to the all-electron orbitals for $r \geq r_c$ and the Kohn-Sham equation is inverted to obtain the pseudopotentials. Transferability describes the absolute of the atomic pseudopotential to reproduce all-electron results in the target system (molecules, solid, etc.).

The all-electron and pseudopotential valence wavefunctions of different angular momentum are illustrated in Fig. 8.1. Cutoff radii r_c are shown as vertical lines for each angular momentum which in this case are 1.75 a.u. In this figure, several important features of pseudopotential are apparent. For example, beyond r_c , the all-electron and the pseudopotential wavefunctions are identical but in the core region, the smooth nodeless pseudopotential wavefunctions are in contrast with the rapidly varying wavefunctions for those of the all-electron. For this particular reference configuration, the Sulfur pseudopotential yields roughly 18.30 meV energy deviation from that of the all-electrons and test configurations give good transferability. However, this convergence error can be reduced

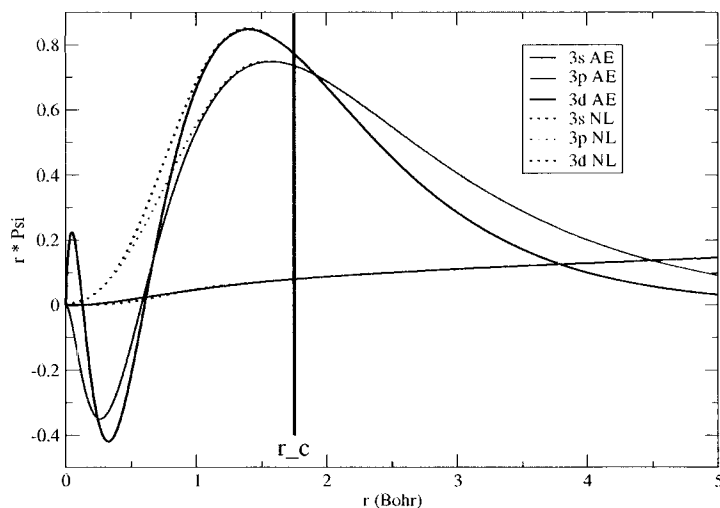


FIG. 8.1: OPIUM generated wavefunction for Sulfur atom. Wavefunction of all-electron (solid lines) and pseudopotential (dash lines) are shown for the three valence orbitals. This configuration is generated with an s-local.

by adjusting either q_c (define cutoff energy) or r_c (control transferability). Increasing q_c yields a better convergence to the all-electron but the number of plane waves also increase considerably hence increasing the computational effort. Similarly, decreasing the core radius r_c moves the pseudo-orbitals closer to the all-electron orbitals and improves the transferability. Therefore, it is necessary to keep a good-balance between the all-electron convergence and transferability. Often, while the quality of the pseudopotential can be determined by inspecting only the convergence errors and transferability, other tests can be performed to verify the pseudopotential quality as well. These include reproducing known properties i.e. molecular vibrational frequencies and crystal properties.

Table 8.1 presents the OPIUM parameters of atoms used in the simulations. We list the optimized cutoff radii, cutoff energy, along with the reference configurations of each atoms. All but arsenic uses the neutral atom reference configuration. We include the d-electron states in the reference configurations of P, S and As, which strikingly show substantial improvement to the transferabilities.

TABLE 8.1: Optimized pseudopotential parameters of atoms in the calculations. This includes cutoff radius, cutoff energy and reference configurations.

Atom	Cutoff radius (a.u.)	Cutoff energy (Ry)	Reference Configuration
Al	2.10	12.50	[Ne]3s ² 3p ¹
Si	2.20	12.25	[Ne]3s ² 3p ²
P	1.72	36.00	[Ne]3s ² 3p ^{5/2} 3d ^{1/2}
S	1.75	36.00	[Ne]3s ² 3p ^{7/2} 3d ^{1/2}
Cl	1.75	36.00	[Ne]3s ² 3p ⁵
As	1.80	36.00	[Ar]4s ² 4p ^{5/2} 4d ⁰

8.2 LDA calculations

We utilize the ABINIT [64] software to calculate the LDA total energies and generate trial wavefunctions for the AFQMC simulations. The total energy is computed self-consistently within density functional theory calculations, using pseudopotentials and planewaves as a basis.

Results of the LDA calculations are presented in Table 8.2. Owing to the good convergence of total energies with respect to system size, energies of each atom are reported for a single supercell. For various supercells, the basis size ranges from about 7000 to 21000 planewaves. We present the total energy of neutral atoms, molecules, singly and doubly ionized atoms. Dissociation energy D_e , the energy required to separate atoms from one another in the dimer, is calculated as $[2E_X - E_{X_2}]$. Similarly, first (IP) and second (IIP) ionization energies are obtained from the difference between the total energy of neutral atoms and ionized atoms, $[E_{X^+} - E_X]$ and $[E_{X^{++}} - E_X]$ respectively. In addition, the given IP and IIP have been size-corrected for long-range spurious periodic image interactions. The correction process is described in Section 8.4 and the formalism is given in more details in Appendix C.

TABLE 8.2: The LDA total energies (from ABINIT) of several atoms and molecules as well as dissociation energy and ionization energy. The supercell size is listed in the second column. The given ionization energies have been corrected based on the charge-simulation cell corrections discussed in Appendix C. Energy is in eV; length is in a.u.

Atom	Supercell size	Total Energy				D_e	IP	IIP
		X	X_2	X^+	X^{++}			
Al	$19 \times 19 \times 19$	-52.31	-	-48.47	-35.98	-	5.99	24.26
Si	$19 \times 19 \times 19$	-102.67	-	-96.54	-86.30	-	8.15	24.50
P	$19 \times 16 \times 16$	-175.52	-357.55	-167.66	-154.60	5.97	20.38	30.21
S	$14 \times 14 \times 14$	-274.42	-	-266.87	-251.61	-	10.30	33.84
	$16 \times 14 \times 14$	-274.45	-554.73	-	-	5.80	-	-
Cl	$18 \times 18 \times 18$	-403.66	-810.41	-392.84	-375.68	3.07	12.97	36.56
As	$20 \times 16.5 \times 16.5$	-168.17	-341.33	-	-	5.04	-	-

8.3 Cutoff Energy Convergence

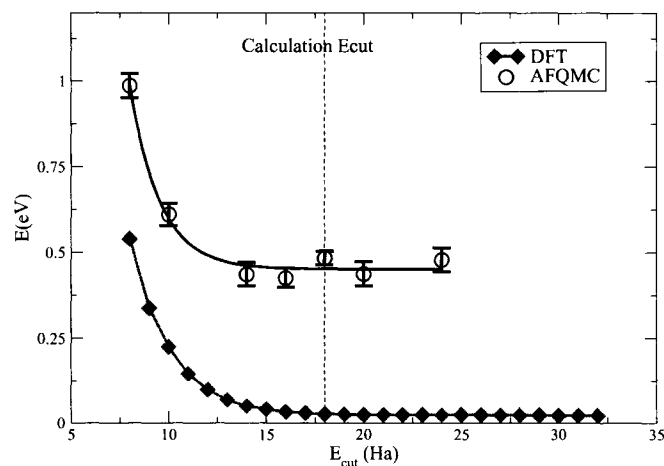


FIG. 8.2: Convergence property of Phosphorous atom in a $14 \times 14 \times 14$ a.u. supercell. The results agree for both the DFT and AFQMC methods. In the calculations, we chose 18 Ha which yields 5.18 meV convergence error with asymptotic value.

To achieve high numerical accuracy, we optimized several parameters in our calculations by performing convergence tests. In practice, we examine the dependence of the total energy on a single parameter, e.g. the planewave cutoff. Fig. 8.2 shows results of convergence with respect to E_{cut} for P atom for both LDA and AFQMC calculations. We

consider a system of a single Phosphorous atom in a cubic supercell of length $L = 14$ a.u. Predicted convergence of the OPIUM q_c parameter is a good prediction of the required E_{cut} in ABINIT. The two sets of data show the same behavior as E_{cut} increases. It is also worthwhile to note that the total energy converges when E_{cut} is above 16 Ha in LDA and, within statistical error, roughly the same value in QMC. We used the 18 Ha cutoff energy for Phosphorous in the calculations, which gives about 5 meV convergence error with respect to the asymptotic value in LDA. All other atoms are tested in the same manner. In summary, our fully converged basis set parameter is a cutoff energy of 7.5 Ha for Al, 6.1 Ha for Si, 19 Ha for S and 18 Ha for Cl and As.

8.4 Finite Size Convergence

Because periodic boundary conditions are imposed in the calculations, the interactions between electrons in the simulation cell and other periodic cells may cause a large finite size error if the supercell is too small. To determine an adequate choice for a supercell, we study the convergence of the total energy with respect to cells size $L \times M \times N$. In Fig. 8.3, the phosphorous supercell convergence results are shown for AFQMC and LDA calculations. As the supercell size increases, the energy decreases in LDA but increases in QMC. In both cases, energy start to converge at approximately $L = 14a.u.$ Compared to the largest $18 \times 18 \times 18$ a.u. supercell, the total energy at $14 \times 14 \times 14$ a.u. yields convergence error of 0.05 eV. In addition, as an illustrative comparison between LDA and AFQMC, Fig. 8.3 indicates a reasonable consistent finite size effect between the two methods. It is sufficient to carry on the test for size-dependent supercell for all other atoms only within the LDA approximations. In Fig. 8.4, LDA finite size convergence of Al, S, Cl, and As is shown.

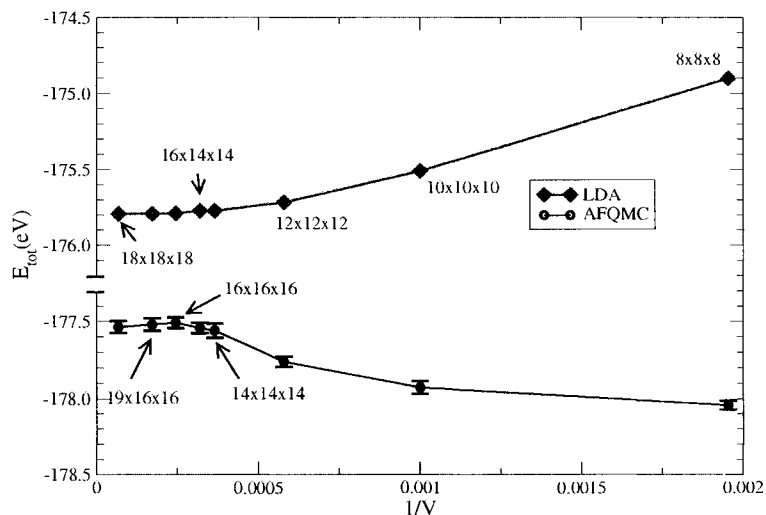


FIG. 8.3: Phosphorous simulation cell convergence of LDA and AFQMC. The diamond symbols denote the results of LDA calculations while the circle symbols denote those of the AFQMC. The convergence take places when the length of the supercells is above 14 a.u.

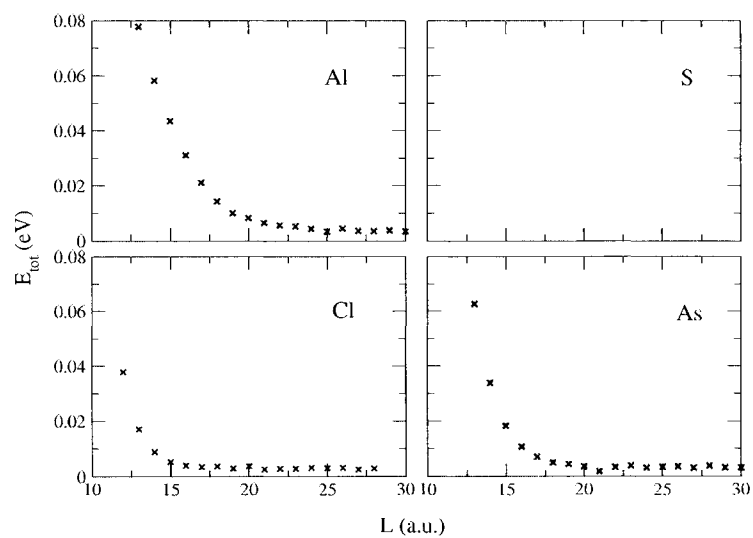


FIG. 8.4: Simulation cell size convergence for Al, S, Cl and As from LDA calculations. Each data corresponds to the scaled absolute total energy which has been subtracted/added by some constant.

To demonstrate the size effect on the dissociation energy and ionization energy, we show results of D_e , IP and IIP and their corresponding total energies with respect to volume, V . AFQMC phosphorous dissociation energy and atom/dimer total energies as a function of $1/V$ given in Fig. 8.5. The top panel shows system size dependence of dissociation energy, and the bottom panel illustrates the convergence error of P and P_2 for supercell ranging from $14 \times 14 \times 14$ to $18 \times 18 \times 18$ a.u. The dimer dissociation energy shows about a 0.5 eV energy variation from the smallest to the largest system size. To investigate the finite size effects more thoroughly, we specify E_{conv} as the total energy of the largest supercell, $18 \times 18 \times 18$ a.u. and plot $(E - E_{\text{conv}})$ vs. $1/V$. Fig. 8.5 shows that P energy converges more rapidly than that of P_2 . The main contribution to the finite size errors in dissociation energy therefore comes from the dimer in P. Another illustration of finite size behavior is presented for Cl molecules. As shown in Fig. 8.6, the Cl_2 D_e converges more rapidly than for P_2 Dissociation energies only vary within about 0.1 eV across the length L . applied to the total energies in

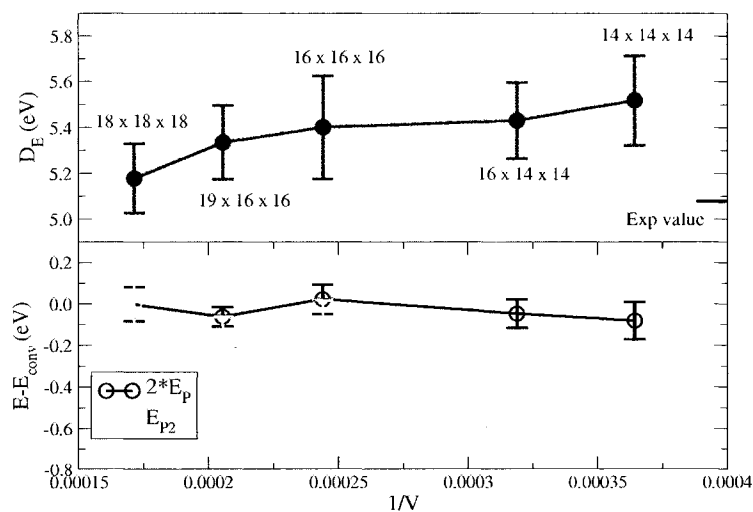


FIG. 8.5: Phosphorous Dissociation energy and total energy of P and P_2 are plotted for different system sizes. The bottom panel plots the difference between total energy and convergence value which is taken from the largest supercells. The biggest supercell is $18 \times 18 \times 18$ a.u. represents the best value closest to the experimental data of 5.08 eV (shown by the solid dash on the left of the top panel).

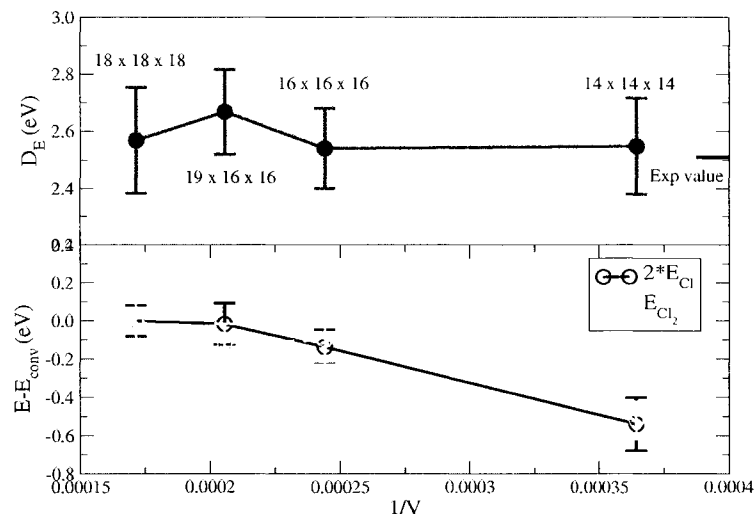


FIG. 8.6: Chlorine Dissociation energy and total energy of Cl and Cl₂ are plotted for different system sizes. The bottom panel plots the difference between total energy and convergence value which is taken from the largest supercells.

In the ionization energy calculations, the supercells are charged $+|e|$ and $+|2e|$ for X^+ and X^{++} cells respectively. When working with periodic boundary conditions, the charged cells become ill-defined since they no longer satisfy charge neutrality. In using the usual interaction potential derived from the Ewald potential, an additional neutralizing charge is artificially introduced in the cell to maintain charge neutrality. The calculated energy converges slowly with the system size because of the interactions between the artificial neutralizing charge and its images in periodic cells. This is shown in the bottom panel of Fig. 8.7, for P, P⁺ and P⁺⁺. To properly treat charged cells in the simulations, we follow the correction scheme introduced by Makov et.al. [66, 67]. A brief introduction to this correction is given in Appendix C. In practice, the calculations of E_{X^+} and $E_{X^{++}}$ depends on the correcting energy, $E_c = q^2 \alpha / 2L = q^2 \xi$ where q is the number of corresponding ionized charge, and α is the Madelung constant which derived from $\alpha = - \sum_j \frac{\pm R}{r_j}$ where R is the nearest-neighbor distance and r_j is the distance between the reference ion and the j^{th} ion [68]. In ABINIT, we correct the total energies by simply subtracting with the Madelung size-correction energy E_c . In AFQMC, the total energy is corrected with $E_c + q\xi$. The idea of the correction is identical; the extra term is due to the particular

way the constant ξ is calculated in our QMC program when the total energy is reported. An example of the CI total energy correction in a charged simulation cell is given below. Comparison between corrected and uncorrected energy is shown in Fig. 8.7 as we plot the modified total energy vs. $1/V$ in the top panel and the corrected total energies converge much more rapidly with supercell size, as expected.

Sample Madelung size-correction for Chlorine[†] ionization energy

LDA			
Charge	$E_{\text{tot}}(\text{Ry})$	Corrected $E_{\text{tot}}(\text{Ry})$ $E_{\text{tot}} - q^2\xi$	IP/IIP (eV)
0	-29.669		
1	-28.873	-28.715	12.97
2	-27.612	-26.982	36.56

QMC			
Charge	$E_{\text{tot}}(\text{Ry})$	Corrected $E_{\text{tot}}(\text{Ry})$ $E_{\text{tot}} - (q + q^2)\xi$	IP/IIP (eV)
0	-29.805(3)		
1	-29.188(3)	-28.873(3)	12.68(6)
2	-28.089(3)	-27.143(3)	36.22(6)

†Simulations in $18 \times 18 \times 18$ a.u., $\xi = 0.1576$ Ry

Figure 8.8 presents the finite size dependence of ionization energy and total energy of P, P⁺ and P⁺⁺. Once again, the bottom panel describes the deviation of total energy from the converged energy, marked at $18 \times 18 \times 18$ a.u., for several supercells. Total energy of the neutral atom is well converged with approximately 0.1 eV deviation from asymptotic value at the smallest size. Singly and doubly ionized atoms show good convergence behaviors beyond $16 \times 14 \times 14$ a.u. The first (IP) and second (IIP) ionization energies have similar shapes, indicating that the source of the finite size errors is the same in each case. Both IP and IIP illustrate nearly 0.3 eV discrepancy at smaller supercells, which is also visible at the total energy level but they are well converged for the higher supercells.

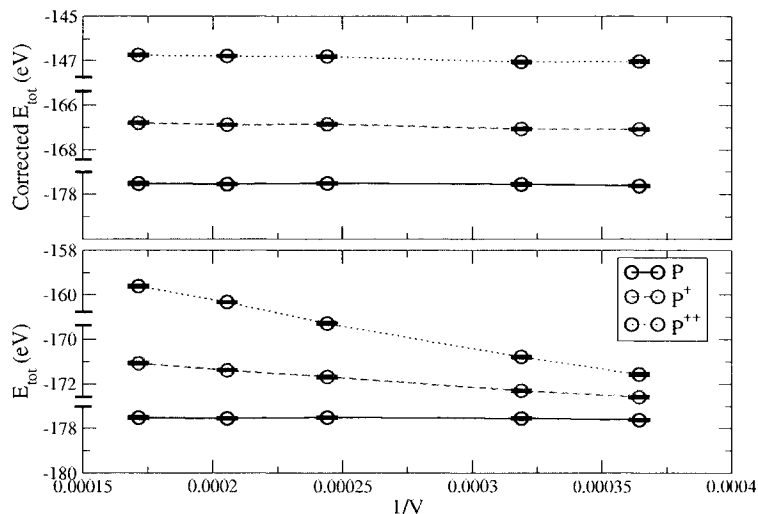


FIG. 8.7: Illustration of the non-periodic charged supercell simulations to the convergence of total energy. The top panel shows the corrected total energy for P, P+ and P++ while bottom panel corresponds to the uncorrected energy. Supercell sizes have the same values as those of Figure 8.5. The calculations are based on AFQMC formulations.

8.5 Trotter Convergence

A systematic Trotter error is introduced due to the noncommutativity of the one-body and two-body Hamiltonians. When the Trotter-Suzuki decomposition [45] is applied to separate these terms in Eq. 7.15, an error of order $\mathcal{O}(\Delta\tau^3)$ is introduced due to the neglected terms. In the calculations, the choice of $\Delta\tau$ is important. If $\Delta\tau$ is too small, the calculations will have high computational demand. On the other hand, a large $\Delta\tau$ will give results with large Trotter errors. These errors can be controlled either by having $\Delta\tau$ sufficiently small so that errors in the approximations are of the same order as the statistical fluctuations from the QMC, or, by extrapolating to $\Delta\tau = 0$. In our study, we carry out AFQMC simulations at different values of $\Delta\tau$, typically, $\Delta\tau = 0.0125$ to 0.075 and extrapolate to $\Delta\tau = 0$. This procedure allows us to remove the trotter error from the calculations. To demonstrate the Trotter errors and the extrapolations in the calculations of dissociation energy and ionization energy, we plot total energy vs. $\Delta\tau$ for S, and S₂ in Fig. 8.9 (LDA trial wavefunctions) and Fig. 8.10 (HF trial wavefunctions). In Fig. 8.11,

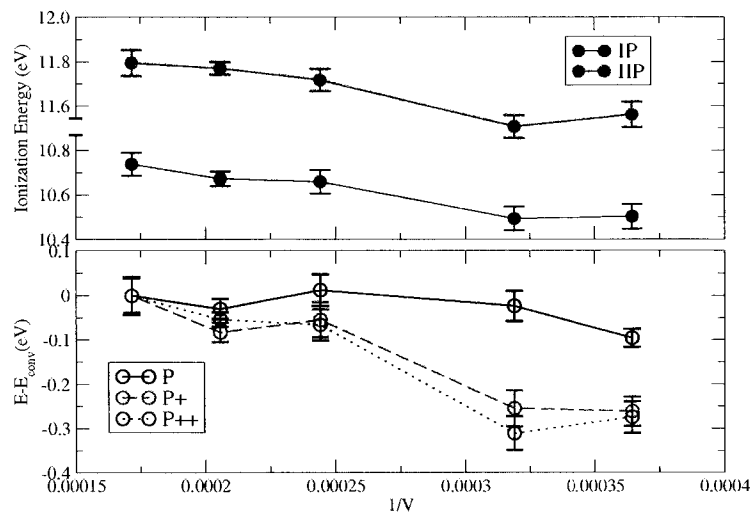


FIG. 8.8: Series of Phosphorous ionization energy and P, P+ and P++ total energy with respect to $1/V$. The bottom panel plots the difference between total energy and the convergence value taken at the largest supercell, $18 \times 18 \times 18$ a.u.

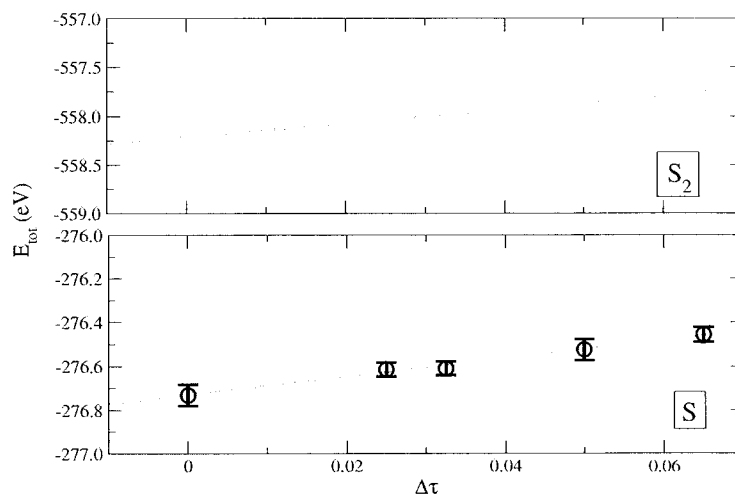


FIG. 8.9: S and S_2 Trotter error extrapolations for LDA wavefunctions (shown in the top and bottom panels respectively) in a $16 \times 14 \times 14$ a.u. supercell. The extrapolated error to remove the Trotter error are shown at $\Delta\tau = 0$, together with the estimated statistical error.

we show similar data for P, P⁺ and P⁺⁺. Energies are extrapolated to remove the error due to the trotter discretization. We would like to point out that in the region of small $\Delta\tau$ for most cases, the trotter errors are less than the AFQMC statistical errors. For the rest of the study, we have exploited this fact and carried out AFQMC calculations at a single value of $\Delta\tau$ where appropriate.

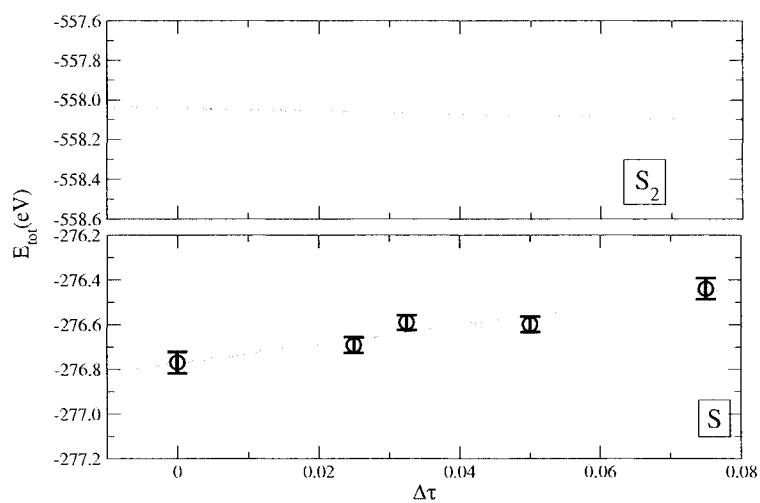


FIG. 8.10: S and S₂ Trotter error extrapolations for Hartree-Fock wavefunctions (shown in the top and bottom panels respectively) in a $16 \times 14 \times 14$ a.u. supercell. The extrapolated value to remove the Trotter error are shown at $\Delta\tau = 0$, together with the estimated statistical error.

8.6 Ground State Properties

We study dissociation energy and ionization energy of the second-row atoms/molecules and As. Atomic and molecular orbitals configurations of interest are summarized in Table 8.3. Dimer dissociation energy (D_e) is calculated as the difference between the total energy corresponding to the dimer at the equilibrium distance and the energy of the isolated

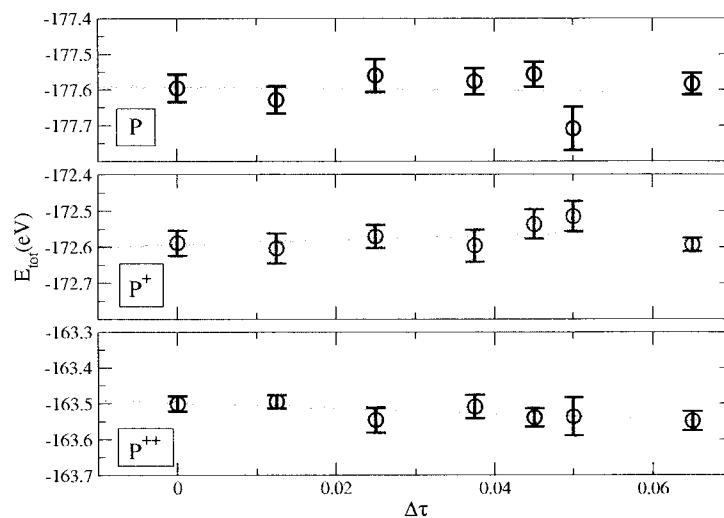


FIG. 8.11: Trotter error extrapolations for P, P+ and P++ (shown in the top, middle and bottom panels respectively) in a $14 \times 14 \times 14$ a.u. supercell. The extrapolated value to remove the Trotter error are shown at $\Delta\tau = 0$, together with the estimated statistical error.

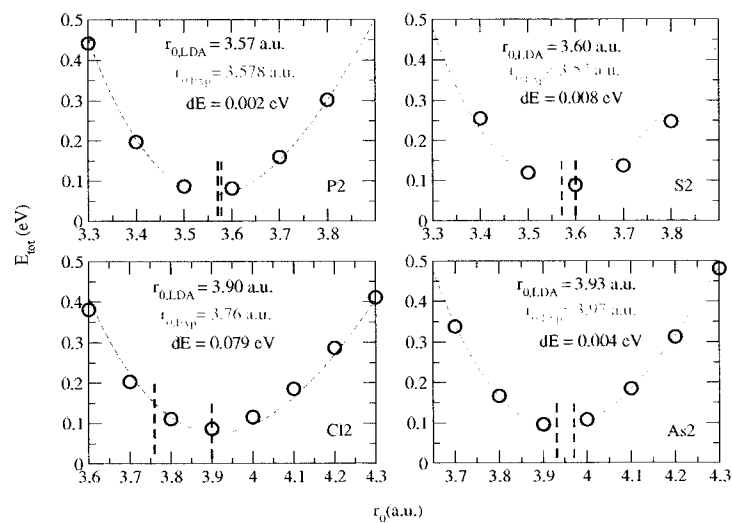


FIG. 8.12: LDA total energy as a function of interatomic distances for P_2 , S_2 , Cl_2 and As_2 . The minima correspond to the LDA estimated bondlengths, and the red vertical lines refer to the equilibrium experimental bondlengths. dE denotes the estimated energy shift from the experiment value when the LDA bondlength is used.

atoms. In LDA, we calculated the equilibrium interatomic distances by plotting several total energies vs. bond distance. The molecule bondlength is then derived by minimizing the fitting function as demonstrated in Fig. 8.12, which gives the value of 3.57 for P_2 , 3.60 for S_2 , 3.90 for Cl_2 , and 3.94 for As_2 (in a.u.). The LDA bondlengths are compared with the experimental bondlengths. For Phosphorous, the bondlengths are nearly identical and the energy deviation is negligible. Although Sulfur and Arsenic bondlength differences are noticeable, the shallow energy curves also cause negligible energy deviation. Chlorine by far gives the largest energy difference between LDA and the experimental bondlengths. We have thus carried out QMC calculations at both the LDA and the experimental bondlengths of Cl_2 . The values at the latter (3.757 a.u.) are reported. Similar to D_e calculations, we compute ionization energy as the difference between total energy of neutral atoms and of ionized atoms. The charged neutralized corrections are applied in order to obtain the convergent results with finite supercell size. The calculated total energies, dissociation energies and ionization energies are given in Table 8.4 for various system sizes. Statistical errors are in the last digits and are indicated in parenthesis. Results were computed with LDA trial wavefunctions. Both restricted and unrestricted trial wavefunctions were tested, but there was no noticeable improvement in the results. Unless otherwise noted, the results are reported using the restricted wavefunctions. It can be easily seen from Table 8.4 that total energies of neutral atoms are generally well converged with system sizes. The fact that size effect is more significant on dimer and ionized atoms than on those of neutral atoms indicates that any size effect for D_e or IP can be alleviated by increasing the size in the dimer/ionized calculations.

In Table 8.5, we report the AFQMC dissociation energy of P_2 at $19 \times 16 \times 16$ a.u., S_2 at $16 \times 14 \times 14$ a.u., Cl_2 at $18 \times 18 \times 18$ a.u. and As_2 at $20 \times 16.5 \times 16.5$ a.u., together with LDA and GGA results [69], and experimental values which have been removed the zero-points effects. Sulfur dimer is worth a special consideration because of its open-shell configuration, therefore we compare the results with those of Hartree-Fock trial

TABLE 8.3: Electronic configurations of atoms and ionized atoms used in the calculations

	atomic orbitals	dimer molecular orbitals
Al	[Ne]3s ² 3p ¹	
Si	[Ne]3s ² 3p ²	
P	[Ne]3s ² 3p ³	$\sigma_{3s}^2 \sigma_{3s}^{*2} \sigma_{3p}^2 \pi_{3p}^4$
S	[Ne]3s ² 3p ⁴	$\sigma_{3s}^2 \sigma_{3s}^{*2} \sigma_{3p}^2 \pi_{3p}^4 \pi_{3p}^{*2}$
Cl	[Ne]3s ² 3p ⁵	$\sigma_{3s}^2 \sigma_{3s}^{*2} \sigma_{3p}^2 \pi_{3p}^4 \pi_{3p}^{*4}$
As	[Ar]4s ² 4p ³	$\sigma_{4s}^2 \sigma_{4s}^{*2} \sigma_{4p}^2 \pi_{4p}^4$

wavefunctions as well as results from Hartree-Fock calculations. The dissociation energy calculated with LDA and HF wavefunctions are in agreement with each other, which demonstrates an insensitivity of the AFQMC to the details of trial wavefunctions that is very desirable.

The comparisons between the AFQMC and the experimental data show excellent agreements (D_e lies within the statistical errors to the experimental values for most cases). The LDA and GGA calculations tend to overestimate the dissociation energy, while the HF seems to significantly underestimate. The biggest dimer we calculated, As₂, also show a better agreement to the experiments than other available methods. For example with the experimental dissociation energy of 3.97 eV, results of the complete active space self-consistent-field (CASSCF) molecular calculations show the As₂ dissociation energy of 3.18 eV [70] and 2.74 eV [71] comparing to that of our AFQMC, 3.97(17) eV. The comparison of these calculations shows that our method gives, for the isolated molecule, results of accuracy similar to or better than other well-established methods.

In Table 8.6 and 8.7, first and second ionization energies are given with the corresponding supercell size of 19×19×19 for Al and Si, 19×16×16 for P, 14×14×14 for S, and 18×18×18 for Cl respectively. Again, we make the standard comparison between AFQMC with LDA and experimental data. In some cases (Si and S), results from DMC,

TABLE 8.4: The QMC total energies of atoms and molecules as well as dissociation energy and ionization energy for different supercells. The given ionization energies have been corrected based on the charge-simulation cell corrections discussed in Appendix C. Energy is in eV ;length is in a.u. The statistical error is listed in the parenthesis. The zero error denotes the values less than 0.005 eV.

	Supercell size	Total energy				D_e	IP	IIP
		X	X_2	X^+	X^{++}			
Al	$15 \times 15 \times 15$	-52.85(1)	-	-46.98(1)	-27.99(0)	-	5.87(2)	24.86(1)
	$19 \times 19 \times 19$	-52.76(1)	-	-46.88(1)	-28.10(0)	-	5.87(2)	24.65(1)
Si	$19 \times 19 \times 19$	-103.58(4)	-	-95.40(4)	-79.09(3)	-	8.18(6)	24.49(5)
P	$14 \times 14 \times 14$	-177.62(2)	-360.64(17)	-167.05(3)	-147.00(3)	5.41(18)	10.56(4)	30.62(4)
	$16 \times 14 \times 14$	-177.54(3)	-360.52(15)	-167.05(4)	-147.04(4)	5.43(17)	10.50(5)	30.51(5)
	$16 \times 16 \times 16$	-177.51(4)	-360.42(22)	-166.85(4)	-146.79(4)	5.40(23)	10.66(5)	30.72(5)
	$19 \times 16 \times 16$	-177.55(2)	-360.43(15)	-166.88(2)	-146.78(2)	5.33(16)	10.67(3)	30.77(3)
	$18 \times 18 \times 18$	-177.52(4)	-360.22(13)	-166.78(4)	-146.73(4)	5.18(15)	10.74(6)	30.79(6)
S	$14 \times 14 \times 14$	-276.85(4)	-	-266.55(6)	-242.56(5)	-	10.30(7)	34.29(7)
	$16 \times 14 \times 14$	-276.73(5)	-558.09(14)	-	-	4.63(17)	-	-
Cl	$14 \times 14 \times 14$	-405.78(7)	-814.11(10)	-392.96(4)	-369.48(3)	2.55(17)	12.83(8)	36.30(7)
	$16 \times 16 \times 16$	-405.58(5)	-813.82(14)	-392.79(3)	-369.41(4)	2.66(17)	12.79(5)	36.18(6)
	$19 \times 16 \times 16$	-405.52(5)	-813.71(10)	-	-	2.67(15)	-	-
	$18 \times 18 \times 18$	-405.51(4)	-813.60(17)	-392.83(4)	-369.30(3)	2.57(19)	12.68(6)	36.21(5)
As	$19 \times 16 \times 16$	-169.23(3)	-342.54(12)	-	-	4.07(13)	-	-
	$18 \times 18 \times 18$	-169.26(3)	-342.97(11)	-	-	4.46(12)	-	-
	$20 \times 16.5 \times 16.5$	-169.21(4)	-342.38(16)	-	-	3.97(17)	-	-

TABLE 8.5: Dissociation energy (eV) of selected molecules when calculated within the LDA, the AFQMC, and the HF. QMC (LDA) and QMC (HF) refer to QMC with LDA wave function and QMC with HF wave function respectively. The statistical errors are given in the parentheses. DMC, HF, GGA and experimental values are from Ref. [72], [73], [69] and [74] respectively.

	QMC (LDA)	QMC (HF)	DMC	HF	LDA	GGA	Exp
P ₂	5.19(16)		4.43(2)	1.73	5.97	5.22	5.08
S ₂	4.63(17)	4.48(19)	4.22(3)	2.23	5.61	4.94	4.41
Cl ₂	2.69(14)		2.28(2)	0.74	3.12	2.76	2.51
As ₂	3.97(17)				5.04	4.35 ¹	3.96

[1] ABINIT with an LDA wavefunctions

TABLE 8.6: First ionization energy (eV) of selected atoms, computed as $\{E_{X^+} - E_X\}$. All QMC calculations are computed with the LDA non-local pseudopotentials. The statistical errors are given in the parentheses. Experimental, HF and DMC values are from [74], [73] and [34] respectively. LDA and GGA are generated from ABINIT.

	QMC	DMC	HF	LDA	GGA	Exp
Al	5.88(2)		5.61	5.87	5.99	5.99
Si	8.18(6)	8.166(14)	7.64	8.15	8.17	8.152
P	10.67(3)		9.88	10.38	10.25	10.49
S	10.09(7)		9.33 ²	10.30	10.24	10.36
Cl	12.68(6)		11.67	12.97	12.94	12.96

[2] In-house calculation

TABLE 8.7: Second ionization energy(eV) of selected atoms, computed as $\{E_{X^{++}} - E_X\}$. All QMC calculations are computed with the LDA non-local pseudopotentials. The statistical errors are given in the parentheses. Experimental and DMC values are from [74] and [34]. LDA and GGA are generated from ABINIT.

	QMC	DMC	HF	LDA	GGA	Exp
Al	24.66(2)			24.46	24.81	24.81
Si	24.49(5)	24.444(42)		24.50	24.41	24.428
P	30.77(3)			30.21	30.10	30.26
S	34.16(7)		32.42	33.84	33.63	33.69
Cl	36.21(5)			36.56	36.52	36.78

HF and GGA are readily available, which we have also included. Al and Si first ionization energies show good agreement with experimental values e.g. with a difference of 0.1 eV from experimental value for Al-IP. A somewhat smaller deviation from experimental value corresponds to Si first ionization energy where only 0.03 eV is observed, similar to the DMC result [34]. However, some results show a larger deviation. For example, first ionization energies of P, S and Cl show nearly 0.3 eV discrepancy from experimental and LDA values. The worst case appears in Sulfur second ionization energy which is reported with nearly 0.5 eV error from the experimental value. We also show the results of IP from HF, DFT-LDA and DFT-GGA calculations. We see than DFT results, particularly those of GGA, are extremely accurate for the ionization energies. Not surprisingly, Hartree-Fock calculations give significant errors underestimating IP and IIP in S by about 1.0 eV.

While the atomization results from AFQMC are uniformly excellent, the ionization results are more mixed. Several factors may have contributed to the larger discrepancies between our QMC ionization potentials and experimental values. It may be that the systematic error from the phaseless approximation is magnified because the absolute energies in the ionization potentials are larger (~ 20 eV for IP, and ~ 20 eV for IIP, compared to ~ 5 eV for dissociation energies). The pseudopotential may also have had an impact. The OPIUM pseudopotentials are generated with DFT-LDA. Whether they are sufficiently ac-

curate to be used in a many-body calculation (such as our QMC) is not firmly established. For example, the effect from non-linear core corrections [75], which can be put in explicitly in an LDA calculation, is less clear in a many-body context. In addition, our trial wavefunctions for open-shell (e.g. in P^+) systems have ignored the shell degeneracies. In LDA calculations this is treated “properly” with fractional fillings in calculating the density. In, QMC, however, we simply create a single-determinant trial wavefunction to use by selecting one of the degenerate orbitals. It is unclear whether this has impacted the results. These factors await further investigation in the future to quantify their effects.

CHAPTER 9

Concluding remarks (AFQMC Study of Molecular Electronic Structure)

The phase-free auxiliary-field quantum Monte Carlo method is a new ground-state many-body approach still being developed in our group. Unlike standard independent-particle approaches for electronic structure, it aims to solve the many-body Schrödinger equation directly, and offers the promise of a more accurate method for strongly correlated systems, where there is tremendous fundamental and technological interest and for which reliable computational methods are needed. Although computationally more demanding, the use of stochastic sampling allows the QMC method to have essentially the same scaling as independent-particle approaches. Compared to the standard diffusion Monte Carlo method, our approach has several promising new features. It imposes second quantization and handles particle symmetry automatically. It allows the use of any one-particle basis, and can incorporate state-of-the-art techniques (non-local pseudopotential, plane-waves and FFT's, etc.) straightforwardly from independent-particle approaches. Further, the results so far have demonstrated an insensitivity to the quality of the trial wave function, thereby reducing the demand for wavefunction optimization in QMC. Applications to

date have yielded results comparable to DMC and some of the most accurate theoretical results in atoms, molecules, and several extended systems.

In this thesis we have further tested the new phase-free auxiliary-field QMC method, and studied its various characteristics in atoms and diatomic molecules. Our AFQMC calculations were performed using the LDA wavefunctions and planewave basis sets, and non-local pseudopotentials generated from LDA to represent the pseudo ions. The use of a planewave basis set offers many advantages, although it also requires large amount of computational time for isolated atoms and molecules. In this sense, these systems represent somewhat unfavorable situations and provide rather stringent tests for our method.

We presented validation and testing of several parameters: cutoff energy, system size and Trotter errors. We computed dissociation energy and ionization energy of the first-row atoms/molecules, in particular Al, Si, P, S, Cl, in addition to As. Results are compared with LDA, GGA and experimental values. In the case of dissociation energy, QMC results show excellent agreement with the experimental values. For ionization potentials in atoms are in reasonable agreement with experiment, but show noticeable systematic errors (up to 0.5 eV). The possible sources for these errors were discussed, and several directions for future study were outlined.

APPENDIX A

Coulomb potential

Using the Ewald method [19, 20, 21, 22, 23], the Coulomb potential is obtained in terms of a direct lattice sum and a 2-D reciprocal lattice sum. As shown below using our Ewald construction, the reciprocal lattice sum [see Eq. (3.6)] will contain only $\mathbf{G} \neq 0$ contributions, and these are conveniently expressed in terms of the Green's function \mathcal{G} for Eq. (3.7):

$$V_{\mathbf{G}}(z) = -4\pi \int_{-\infty}^{\infty} \mathcal{G}(z - z') \rho_{\mathbf{G}}(z') dz'. \quad (\text{A.1})$$

Physically meaningful results require that the $\mathbf{G} \neq 0$ solutions satisfy $\lim_{|z| \rightarrow \infty} V_{\mathbf{G}}(z) = 0$, which leads to the following unique definition of the $\mathbf{G} \neq 0$ Green's function:

$$\mathcal{G}(z - z') \equiv - \frac{\left[\vartheta(z - z') e^{-G(z - z')} + \vartheta(z' - z) e^{G(z - z')} \right]}{2G}, \quad (\text{A.2})$$

where $G = |\mathbf{G}|$. For any reasonably localized charge distribution $\rho_{\mathbf{G}}(z)$, Eqs. (A.1) and (A.2) result in well-behaved, exponentially decaying solutions of $V_{\mathbf{G}}(z)$ as $|z| \rightarrow \infty$.

We now describe our Ewald construction in more detail. The potential is given as the sum of three terms

$$v(\mathbf{l}' - \mathbf{l}) = v_1(\mathbf{l}' - \mathbf{l}) + v_2(\mathbf{l}' - \mathbf{l}) + v_s(\mathbf{l}'), \quad (\text{A.3})$$

where v_1 and v_2 are due to $\rho_1(\mathbf{r})$ and $\rho_2(\mathbf{r})$, respectively in Eq. (3.13), and v_s is the correction for the interaction of the point charge $q_{l'}$ with its own Gaussian density $q_{l'}g(\mathbf{r} - \tilde{\mathbf{l}}')$ in $\rho_2(\mathbf{r})$.

To calculate $v_1(\mathbf{l}' - \mathbf{l})$ we place, for consistency, the ($\mathbf{R} \neq 0$) $q_{\mathbf{l}'}$ images at their vertical projections onto the plane of the $q_{\mathbf{l}}$ sublattice. $v_1(\mathbf{l}' - \mathbf{l})$ is then given by

$$v_1(\mathbf{l}' - \mathbf{l}) = q_{\mathbf{l}} \sum_{\mathbf{R}} \frac{\operatorname{erfc}(\sqrt{\alpha} |\mathbf{l}' - \mathbf{l} - \mathbf{R}|)}{|\mathbf{l}' - \mathbf{l} - \mathbf{R}|} - q_{\mathbf{l}} \sum_{\mathbf{R} \neq 0} \frac{\operatorname{erfc}(\sqrt{\alpha} |\mathbf{l}' - \tilde{\mathbf{l}}' - \mathbf{R}|)}{|\mathbf{l}' - \tilde{\mathbf{l}}' - \mathbf{R}|}. \quad (\text{A.4})$$

The mathematical form of this contribution is identical to its 3-D counterpart, except that the sum is over 2-D rather than 3-D direct-lattice vectors \mathbf{R} .

The 2-D planewave expansion of $\tilde{\rho}_2^{(\mathbf{l}, \mathbf{l}')}(\mathbf{r})$ in Eq. (3.17) is given by

$$\tilde{\rho}_2^{(\mathbf{l}, \mathbf{l}')}(\mathbf{r}) = q_{\mathbf{l}} \left(\frac{\alpha}{\pi A^2} \right)^{1/2} e^{-\alpha(z-l_z)^2} \sum_{\mathbf{G} \neq 0} e^{-G^2/4\alpha} \left[e^{-i\mathbf{G} \cdot \mathbf{l}_{\alpha p}} - e^{-i\mathbf{G} \cdot \mathbf{l}'_{\alpha p}} \right] e^{i\mathbf{G} \cdot \mathbf{r}_p}, \quad (\text{A.5})$$

where we have used the fact that $\tilde{\mathbf{l}}'_z = l_z$. Note that the $\mathbf{G} = 0$ term vanishes. Substituting into Eq. (A.1) and using Eq. (A.2), yields:

$$v_2(\mathbf{l}' - \mathbf{l}) = \sum_{\mathbf{G} \neq 0} \frac{\pi}{AG} [f(G) - f(-G)] [e^{i\mathbf{G} \cdot (\mathbf{l}'_p - \mathbf{l}_p)} - 1], \quad (\text{A.6})$$

where

$$f(x) \equiv e^{x(l'_z - l_z)} \operatorname{erfc} \left(\frac{2\alpha |l'_z - l_z| + x}{2\sqrt{\alpha}} \right). \quad (\text{A.7})$$

Finally, the correction for the interaction of the point charge $q_{\mathbf{l}'}$ with its own Gaussian density is given by:

$$v_s(\mathbf{l}') = \frac{\operatorname{erf}(\sqrt{\alpha} |\mathbf{l}' - \tilde{\mathbf{l}}'|)}{|\mathbf{l}' - \tilde{\mathbf{l}}'|}. \quad (\text{A.8})$$

As verified by direct calculation, the sum of these three terms is independent of the parameter α . For efficiency, $v(\mathbf{l}' - \mathbf{l})$ is stored as a look-up table.

APPENDIX B

Pseudopotentials

Even though the number of plane waves is reduced substantially in the wavefunction by truncating those with large kinetic energy, the plane wave basis required to expand each electronic wavefunction will still be very large no matter how small the cutoff energy is. Fortunately, the property of a solid is chemically dependent on valence electrons to a much greater degree than those of the core electrons. Therefore, the pseudopotential has offered a way to further reduce the number of plane waves for electronic wavefunctions. The method removes the core electrons and replaces the strong potential with the weaker ones. The all-electron (AE) wavefunctions are also replaced with pseudo-wavefunctions which are smooth and mimic the behaviors of the AE wavefunctions beyond the core region whose boundary is specified with the cutoff radius r_c . Because pseudopotential constructions are not unique, there exist several methods for generating them. However, most constructions should follow the same guidelines [76, 77, 78] which are

1. Pseudo wavefunctions should be nodeless.
2. Beyond r_c , the normalized pseudo wavefunction must be equal to the all-electron wavefunction.

$$\phi_l^{PP}(r) = \phi_l^{AE}(r)$$

3. The charge of pseudo wavefunctions must be the same as those of the all-electron wavefunctions within r_c .

$$\int_0^{r_{cl}} |\phi_l^{AE}(r)|^2 r^2 dr = \int_0^{r_{cl}} |\phi_l^{AE}(r)|^2 r^2 dr$$

4. The eigenvalues of the valence all-electron and pseudopotential must be identical.

$$\epsilon_l^{PP} = \epsilon_l^{AE}$$

5. Pseudo wavefunctions must be continuous at the core radius r_c as so must their first and second derivative.

Pseudopotentials which meet all these requirements are said to be norm-conserving. The construction is based on the density function theory [42, 79] whose central idea aims to obtain a screening potential by solving the Kohn-Sham equation self-consistently. Pseudo-orbitals $\phi(r)$ are prescribed based on the optimized pseudopotential method [80] which writes wavefunctions as the sum of Bessel functions,

$$\tilde{\phi}(r) = \begin{cases} \sum_{i=1}^N \beta_i j_l(q_i r) & r \leq r_c \\ \phi(r) & r > r_c \end{cases} \quad (\text{B.1})$$

The prefactors of the four Bessel functions appearing in the first sum are chosen such that wave functions are normalized and continuous (and up to second derivative continuous) at r_c . The latter is combined for the purpose of optimizing the convergence of pseudo-wavefunctions. With this choice of $\tilde{\phi}(r)$, the constructed pseudo-wavefunctions are smooth and nodeless in the core region. With all the requirement met, the screening potential is obtained by inverting the Kohn-Sham equation, and is expressed as:

$$V_{scr,l}(r) = \epsilon_l + \frac{l(l+1)}{2r^2} + \frac{1}{2\tilde{\phi}(r)} \frac{d^2}{dr^2} [\tilde{\phi}(r)], \quad (\text{B.2})$$

where ϵ_l is the all-electron eigenvalue at the angular momentum l . The descreening potential $\tilde{V}_l(r)$ is then calculated by directly subtracting the Hartree and exchange-correlation potentials from the screening potential. By doing this, the pseudopotential maintains the consistence and unbiased approach in which pseudo-orbitals constructed from the reference state are able to use in all other configurational states. Since electrons with different angular momentum scatter differently in the core region, it is essential to have a non-local pseudopotential which defines different pseudopotentials for different angular momentum components. We generate the non-local pseudopotential based on the Kleinman-Bylander scheme [54]. The ionic pseudopotential is divided into two components. One represents the local pseudopotential which is chosen arbitrarily at the initialization process, often those of the lower angular momentum i.e. s or p. The other is the semi-local part which by definition is the difference between the ionic and local pseudopotential:

$$\Delta V_l(r) = \tilde{V}_l(r) - V_L(r). \quad (\text{B.3})$$

Following the Kleinman-Bylander scheme, the non-local pseudopotential is approximate as the reference wavefunction ϕ_l is projected out from the non-local potential for each angular l . The pseudopotential is

$$\begin{aligned} \hat{V}_{\text{ion}}|\Psi_{nl}\rangle &= \hat{V}^{\text{loc}}|\Psi_{nl}\rangle + \sum_l \frac{\langle \Psi_{nl}^{\text{ref}}|\Delta\hat{V}_l|\Psi_{nl}\rangle}{\langle \Psi_{nl}^{\text{ref}}|\Delta\hat{V}_l|\Psi_{nl}^{\text{ref}}\rangle} \Delta\hat{V}_l|\Psi_{nl}^{\text{ref}}\rangle \\ \langle \vec{r}|\hat{V}_{\text{ion}}|\Psi_{nl}\rangle &= V^{\text{loc}}(\vec{r})\Psi_{nl}(\vec{r}) + \sum_l \frac{\int \Psi_{nl}^{\text{ref}}(\vec{r}')\Delta\hat{V}_l(\vec{r}')\Psi_{nl}(\vec{r}')d^3r'}{\int \Psi_{nl}^{\text{ref}}(\vec{r}')\Delta\hat{V}_l(\vec{r}')\Psi_{nl}^{\text{ref}}(\vec{r}')d^3r'} \Delta\hat{V}_l(\vec{r})\Psi_{nl}^{\text{ref}}(\vec{r}), \end{aligned} \quad (\text{B.4})$$

where $\Delta V_l(\vec{r})$ is the l -dependent correction term. The quality of the pseudopotential is determined through two properties; transferability and convergence, which can be controlled through the cutoff radius r_c . Good convergence potential relates to the construction with large r_c which gives the smooth and nodeless pseudo-wavefunction. However, this configuration yields very low transferability in which it is less likely to reproduce pseudopotential in other atomic states than those of the reference state. Smaller r_c increases

transferability due to the fact that the pseudo-wavefunction is constructed closely to the true all-electron wavefunction. However, very small r_c is not suitable to the construction because the smaller r_c gets, the less smooth the wavefunctions become. The least possible value of r_c must be at the outer node of the all-electron wavefunction so that the wavefunctions remain nodeless.

APPENDIX C

Charged Simulation Cell Correction

In the systems whose atomic species are charged, the total energy diverge with system size when imposing the periodic boundary condition. Therefore, a special consideration must be given in order to bring back size convergence to the calculations. In this appendix, we discuss the charged simulation cell formalism which is described by Makov and Payne[66, 67] to treat a non-periodic system in a periodic calculation.

In this formalism, a large supercell containing a charged system can be mapped into a new supercell which have the same charged system immersed in a positive jellium background which neutralize the overall system charge. The energy of the new system converges as a power law of the supercell size, L . A correction up to $\mathcal{O}(L^{-5})$ can be used to correct the total energy in order to obtain a more rapid convergence of the result. Expression for the charge density of the system described above is

$$\rho(\mathbf{r}) = \rho_c(\mathbf{r}) + n_0, \quad (\text{C.1})$$

where $\rho_c(\mathbf{r})$ is the charge density of the atom of interest. The jellium density, n_0 , can be expressed as $n_0 = -q/V_c$ in which q is the total charge and V is the supercell volume. The density can be separated into two parts, namely

$$\rho(\mathbf{r}) = \underbrace{[n_0 + q\delta(\mathbf{r} - \mathbf{r}_0)]}_{\rho_1} + \underbrace{[\rho_c(\mathbf{r}) - q\delta(\mathbf{r} - \mathbf{r}_0)]}_{\rho_2} \quad (\text{C.2})$$

where r_0 is chosen such that ρ_2 contains no dipole i.e. the energy due to ρ_2 - ρ_2 interaction converges as $\mathcal{O}(L^{-5})$ [66, 67].

Therefore the energy of interaction can be separated into three components: E_{11} , E_{22} and E_{12} . The three energies are defined as the interaction on a lattice between ρ_1 - ρ_1 , ρ_2 - ρ_2 and ρ_1 - ρ_2 respectively. E_{11} is referred to as the Madelung energy of a system of point charges on a cubic lattice in a neutralized background,

$$E_{11} = -\frac{q^2\alpha}{2L}. \quad (\text{C.3})$$

The interaction of the neutral charge density, ρ_2 simply converges to $\mathcal{O}(L^{-5})$ (as mentioned above).

The third contribution, E_{12} can be divided into two components, the interaction between ρ_2 and the point charge in ρ_1 and the interaction of ρ_2 with the jellium background. The first term, however, vanishes due to the symmetry for a simple cubic lattice. The second component leads to a total contribution of

$$E_{12} = \frac{2\pi q}{3V_c} \int_{cell} d^3r \rho_2(\mathbf{r}) r^2 + \mathcal{O}(L^{-5}) \quad (\text{C.4})$$

Therefore, the total energy for a simple cubic lattice for charged supercell is

$$E = E_0 - \frac{q^2\alpha}{2L} - \frac{2\pi qQ}{3L^3} + \mathcal{O}(L^{-5}), \quad (\text{C.5})$$

BIBLIOGRAPHY

- [1] C. Tahan, M. Suewattana, P. Larsen, Shiwei Zhang, and H. Krakauer, in *Fundamental Physics of Ferroelectrics 2001*, edited by H. Krakauer (AIP conf. Proceedings, 2001), vol. 582, p. 118.
- [2] M. Suewattana, H. Krakauer, and S. Zhang, *Phys. Rev. B* **71**, 224101 (2005).
- [3] M. Suewattana and H. Krakauer and S. Zhang and E. J. Walter (to be submitted to *Phys. Rev. B*).
- [4] K. Uchino, in *Piezoelectric Actuators and ultrasonic Motors* (Kluwer Academic Publishers, Boston, 1996).
- [5] S.-E. Park and T. E. Shrout, *J. Appl. Phys.* **82**, 1804 (1997).
- [6] M. A. Akbas and P. K. Davies, in *Solid State Chemistry of Inorganic Materials*, edited by P. Davies, A. J. Jacobson, C. Torardi, and T. A. Vanderah (Materials Research Society, 1997), vol. 453, p. 483.
- [7] L. Chai, M. A. Akbas, P. K. Davies, and J. B. Parise, *Materials Research Bulletin* **32**, 11 (1997).
- [8] M. A. Akbas and P. K. Davies, *J. Am. Ceram. Soc.* **80**, 2933 (1997).
- [9] M. A. Akbas and P. K. Davies, *Journal of Materials Research* **12**, 2617 (1997).
- [10] E. Husson, *Mat. Res. Bull.* **23**, 357 (1988), *ibid.*, **25**, 539 (1990).

- [11] J. Chen, *J. Am. Cer. Soc.* **72**, 593 (1989).
- [12] A. B. Bortz, M. H. Kalos, and J. L. Lebowitz, *J. Comput. Phys.* **17**, 10 (1975).
- [13] L. Bellaïche and D. Vanderbilt, *Phys. Rev. Lett.* **81**, 1318 (1998).
- [14] K. A. Jackson, G. H. Gilmer, and D. E. Temkin, *Phys. Rev. Lett.* **75**, 2530 (1995).
- [15] V. A. Shneidman, K. A. Jackson, and K. M. Beatty, *J. Chem. Phys.* **111**, 6932 (1999).
- [16] See, for example, K. Binder and M. H. Kalos, in *Monte Carlo Methods in Statistical Physics*, edited by K. Binder (Springer-Verlag, Berlin, Berlin, 1986), 2nd ed.
- [17] R. A. Laudise, in *The Growth of Single Crystals* (Prentice-Hall, Inc, Englewood Cliffs, 1970).
- [18] J. C. Brice, in *The Growth of Crystal from the Melt* (Interscience Publishers, New York, 1965).
- [19] S. W. de Leeuw, J. W. Perram, and E. R. Smith, *Proc. R. Soc. Lond.* **A373**, 27 (1980).
- [20] S. W. de Leeuw and J. W. Perram, *Molec. Phys.* **37**, 1313 (1979).
- [21] B. Nijober and F. de Wette, *Physica* **23**, 309 (1957).
- [22] D. M. Ceperley, *Phys. Rev. B* **18**, 3126 (1978).
- [23] E. R. Smith, *Physica* **120A**, 327 (1983).
- [24] A. Levi and M. Kotrla, *J. Phys.: Cond. Matt.* **9**, 299 (1997).
- [25] See, for example, M. H. Kalos and P. A. Whitlack, *Monte Carlo Methods* (John Wiley and Sons, New York, 1986).
- [26] Z. Wu and H. Krakauer, *Phys. Rev. B* **63**, 137113 (2001).

- [27] P. K. Davies, J. Tong, and T. Negas, *J. Am. Ceram. Soc.* **80**, 1727 (1997).
- [28] M. A. Akbas and P. K. Davies, *J. Am. Ceram. Soc.* **81**, 670 (1998).
- [29] See, for example, R. E. Cohen, ed., *Fundamental Physics of Ferroelectrics 2002*, vol. 535 (AIP conf. Proceedings, 2002).
- [30] A. J. Williamson, R. Q. Hood, and J. C. Grossman, *Phys. Rev. Lett.* **87**, 246406 (2001).
- [31] J. C. Grossman and et al., *Phys. Rev. Lett.* **36**, 472 (2001).
- [32] R. Maezono, M. D. Towler, Y. Lee, and R. J. Needs, *Phys. Rev. B* **68**, 165103 (2003).
- [33] P. R. C. Kent, R. Q. Hood, M. D. Towler, R. J. Needs, and G. Rajagoapl, *Phys. Rev. B* **57**, 15293 (1998).
- [34] Y. Lee and R. J. Needs, *Phys. Rev. B.* **63**, 035121 (2003).
- [35] J. C. Grossman and L. Mitas, *Phys. Rev. Lett.* **74**, 1323 (1995).
- [36] M. Born and J. R. Oppenheimer, *Ann. Physik* **84**, 457 (1927).
- [37] V. Fock, *Z. Phys.* **61**, 126 (1930).
- [38] D. R. Hartree, *Proc. Cambridge Phil. Soc.* **24:89**, 111,426 (1928).
- [39] R. G. Parr and Y. Weitao, *in Density functional theory of atoms and molecules* (Oxford University Press, New York, 1994).
- [40] J. P. Perdew and W. Yue, *Phys. Rev. B* **33**, 8800 (1986).
- [41] J. P. Perdew and et.al., *Phys. Rev. B* **46**, 6671 (1992).
- [42] W. Kohn and L. Sham, *Phys. Rev. A* **140**, 1133 (1965).

- [43] R. M. Martin, in *Electronic Structure: Basic Theory and Practical Methods* (Cambridge University Press, New York, 2004).
- [44] B. L. Hammond, J. W. a. Lester, and P. J. Reynolds, in *Monte Carlo Methods in Ab Initio Quantum Chemistry, World Scientific Lecture and Course Notes in Chemistry Vol. I* (World Scientific, Singapore, 1994).
- [45] S. Zhang and H. Krakauer, Phys. Rev. Lett. **90**, 136401 (2003).
- [46] J. Hirsch, Phys. Rev. B **28**, 4059 (1983).
- [47] G. Sugiyama and S. Koonin, Ann. Phys. **168**, 1 (1986).
- [48] D. Hamann and S. Fahy, Phys. Rev. B **41**, 11352 (1990).
- [49] W. Purwanto and S. Zhang, Phys. Rev. E **70**, 056702 (2004).
- [50] C. W. Johnson, S. C. Koonin, G. G. Lang, and W. E. Ormand, Phys. Rev. Lett. **69**, 3157 (1992).
- [51] S. Koonin, D. Dean, and K. Langanke, Phys. Rep. **278**, 1 (1997).
- [52] J. Hubbard, Phys. Rev. Lett. **3**, 77 (1959).
- [53] R. D. Stratonovich, Dokl. Akad. Nauk. SSSR **115**, 1907 (1957).
- [54] L. Kleinman and D. Bylander, Phys. Rev. Lett **48**, 1425 (1982).
- [55] J. J. Sakurai, in *Modern Quantum Mechanics* (Addison-Wesley Publishing, New York, 1994).
- [56] S. Zhang, in *Theoretical Methods for strongly Correlated Electrons*, edited by D. Senechal, A. M. Tremblay, and C. Bourbonnais (Springer, New York, 2003), pp. 39–74.

- [57] S. Zhang, in *Quantum Monte Carlo in Physics and Chemistry*, edited by M. P. Nightingale and C. J. Umrigar (Kluwer Academic Publishing, New York, 1999).
- [58] H. F. Trotter, Proc. Am. Math. Soc. **10**, 545 (1959).
- [59] M. Suzuki, Commun. Math. Phys. **51**, 183 (1976).
- [60] S. Zhang, J. Carlson, and J. E. Gubernatis, Phys. Rev. B **55**, 7464 (1997).
- [61] S. Zhang, H. Krakauer, W. A. Al-Saidi, and M. Suewattana, Comp. Phys. Comm. **169**, 394 (2005).
- [62] D. M. Ceperley and B. J. Alder, J. Chem. Phys. **81**, 5833 (1984).
- [63] N. Rom, D. M. Charutz, and D. Neuhauser, Chem. Phys. Lett. **270**, 382 (1997).
- [64] X. Gonze and et. al., Comput. Mat. Sci. **25**, 478 (2002).
- [65] <http://opium.sorcelforge.net>.
- [66] G. Makov and M. C. Payne, Phys. Rev. B **51**, 4014 (1995).
- [67] G. Makov, R. Shah, and M. C. Payne, Phys. Rev. B **53**, 15513 (1996).
- [68] C. Kittel, *Introduction to Solid State Physics* (John Wiley & son Inc., New York, 1996).
- [69] D. Patton, D. V. Porezag, and M. R. Pederson, Phys. Rev. B **55**, 7454 (1997).
- [70] Y. Sakai and E. Miyoshi, J. Chem. Phys **106**, 8084 (1997).
- [71] Y. Moshizuki and *et al.*, prb **49**, 4658 (1994).
- [72] J. C. Grossman, J. Chem. Phys **117**, 1434 (2002).
- [73] D. Feller and K. A. Peterson, J. Chem. Phys. **108**, 154 (1998).

- [74] D. R. Lide, ed., *Handbook of Chemistry and Physics 83rd Edition* (CRC press, New York, 2002).
- [75] D. Porezag, M. R. Pederson, and A. Y. Liu, *Phys. Rev. B* **60**, 14132 (1999).
- [76] N. Troullier and J. L. Martins, *Phys. Rev. B* **43**, 1993 (1991).
- [77] D. R. Hamann, M. Schluter, and C. Chiang, *Phys. Rev. Lett.* **43**, 1979 (1979).
- [78] G. B. Bachelet, D. R. Hamann, and M. Schluter, *Phys. Rev. B* **26**, 4199 (1982).
- [79] P. Hohenberg and W. Kohn, *Phys. Rev.* **136**, B864 (1964).
- [80] A. M. Rappe and et.al., *Phys. Rev. B* **41**, 1227 (1990).

VITA

Malliga Suewattana

Malliga Suewattana was born in Thoen, Lampang Province, Thailand on April 15, 1976. In 1982, she began her education at Lomrad Elementary School in Thailand. She graduated from Bunyawat Wittayalai High School in 1994. She became a DPST (the Development of Science and Technology Talented Project) scholar and entered the faculty of science of Chiangmai University. In 1995, she won the DPST full-scholarship to study abroad, and transferred to Lehigh University, Bethlehem, Pennsylvania where she completed her undergraduate studies and received a Bachelor of Science in Physics in 1999.

She continued her studies at the College of William and Mary in Virginia. She joined the research group of Prof. Shiwei Zhang and Prof. Henry Krakauer in 2000. In May 2001, she received her Master of Science in Physics. This dissertation is part of the completion of the Ph.D and was defended on September 8, 2005 at the College of William and Mary in Virginia.